Master's Thesis

Research on Advanced Three-port Dual-Active-Bridge (DAB) Converters for DC Microgrid

Juyoung Sim

Department of Electrical Engineering

Graduate School of UNIST

2020

Research on Advanced Three-port Dual-Active-Bridge (DAB) Converters for DC Microgrid

Juyoung Sim

Department of Electrical Engineering

Graduate School of UNIST

Research on Advanced Three-port Dual-Active-Bridge (DAB) Converters for DC Microgrid

A thesis/dissertation
submitted to the Graduate School of UNIST
in partial fulfillment of the
requirements for the degree of
Master of Science

Juyoung Sim

12 Dec. 2019

Approved by

Advisor

Jee-Hoon Jung

Research on Advanced Three-port Dual-Active-Bridge (DAB) Converters for DC Microgrid

Juyoung Sim

This certifies that the thesis/dissertation of Juyoung Sim is approved.

12 Dec. 2019

signature

Advisor: Jee-Hoon Jung

signature

Jingook Kim

signature

Jeong hwan Jeon

Abstract

Three-port dual-active-bridge converter (DAB) has been studied to integrate three DC units into one converter. it can increase power density as well as cost-effectiveness with small number of components. However, it has power correlation among the three ports, which brings complexity to control.

This thesis investigates advanced thee-port DAB converters to overcome the power correlation issue the conventional converter suffers from and even achieve higher power density and higher efficiency. Two-inductor three-port DAB converter is proposed to eliminate the power correlation issue without additional control. It uses only two series power inductors, whereas the conventional has three of them. The proposed converter is theoretically analyzed and compared with the conventional converter. The effectiveness of the proposed converter is verified by a simulation software, PSIM and a 5-kW prototype converter. Dual-transformer three-port DAB converter using two transformers is also introduced. It removes the above-mentioned problem that the conventional converter has. It can fully use its transformer magnetizing inductances to extend the zero voltage switching (ZVS) capability at low power. The magnetizing design methodology is proposed to effectively extend the ZVS capability. The validity of the proposed magnetizing design method is verified by PSIM and a 3-kW prototype converter.

A voltage balancer for bipolar low-voltage DC (LVDC) distribution is proposed using Two-inductor three-port DAB converter. A bipolar LVDC distribution system used in residential and building applications requires AC-DC converters and voltage balancers that balance the two DC pole polarities. The proposed balancer can balance the bipolar voltage levels in case of grid-tied voltage balancer failures. It can balance the bipolar DC voltage level without complex control. Furthermore, it has less current stress in power switches than that of the conventional three-port DAB converter. The effectiveness of the proposed converter is verified with a 3-kW prototype converter.

Contents

Abstract

List of Figures

List of Tables

List of Abbreviations

Ⅰ. Introduction ---- 1
Ⅱ. Conventional Three-port Dual-active-bridge (DAB) Converter ---- 4
2.1 Theoretical Analysis ---- 4
2.2 Control Strategy ---- 8
2.3 Simulation Results ---- 12
Ⅲ. Advanced Three-port DAB Converter ---- 17
3.1 Two-inductor Three-port DAB Converter ---- 17
3.1.1 Proposed Converter Structure ---- 17
3.1.2 Theoretical Analysis ---- 18
3.1.3 Simulation and Experimental Results ---- 24
3.2 Dual-transformer Three-port DAB Converter ---- 31
3.2.1 Proposed Converter Structure ---- 31
3.2.2 Theoretical Analysis ---- 32
3.2.3 Zero Voltage Switching (ZVS) Capability Extentsion ---- 33
3.2.4 Magnetizing Inductance Design ---- 38
3.2.3 Simulation and Experimental Results ---- 41
IV. Isolated Voltage Balancer for Bipolar LVDC Distribution ---- 51
4.1 Proposed Voltage Balancer Structure ---- 51
4.2 Theoretical Analysis ---- 53
4.2.1 Voltage Balancing Operation ---- 53
4.2.2 Current Stress Reduction ---- 55
4.3 Experimental Results ---- 57
V. Conclusion ---- 63
REFERENCES ---- 64
APPENDIX ---- 68

List of Figures

Fig. 1.1 DC microgrid concept diagram with different loads and distributed sources

Fig. 1.2 Dual-active-bridge (DAB) converter structure

Fig. 1.3 DC microgrid concept diagram with three-port DC-DC converters

Fig. 2.1 Conventional three-port DAB converter

Fig. 2.2 Simplified port operated with 50 % duty ratio at a fixed switching frequency

Fig. 2.3 Wye-connected equivalent circuit for conventional three-port DAB converter

Fig. 2.4 Operating waveforms of the conventional three-port DAB converter ($\phi_{13} > \phi_{12}$)

Fig. 2.5 Delta-connected equivalent circuit for conventional three-port DAB converter

Fig. 2.6 Power curve over phase shift between port-to-port

Fig. 2.7 Each port power curve over phase shift ϕ_{12} and ϕ_{13}

Fig. 2.8 Independent power control algorithm block diagram

Fig. 2.9 Variations of decoupling matrix elements over Port 2 power under Port 3 power fixed to 1.0 p.u

Fig. 2.10 Conventional three-port DAB converter realized in PSIM

Fig. 2.11 Variations of decoupling matrix elements over power: (a) under changing Port 2 and fixing Port 3 to 1 kW, (b) under changing Port 3 and fixing Port 2 to 1 kW

Fig. 2.12 Steady-state operational simulation results at operating points: (a): ϕ_{12} = 0.372, ϕ_{13} = 0.329 (b): ϕ_{12} = 0.262, ϕ_{13} = 0.130

Fig. 2.13 Simulation results of Port 2 and Port 3 power control: (a) without decoupling strategy (b) with decoupling strategy

Fig. 2.14 Effect on Port 3 control when the load of Port 2 changes: (a) 380 W to 1000 W at t = 0.1 sec, (b) 1 kW to 100 W at t = 0.15 sec

Fig. 3.1 Two-inductor three-port DAB converter

Fig. 3.2 Delta-connected equivalent circuit for Two-inductor three-port DAB converter

Fig. 3.3 Operating waveforms of Two-inductor three-port DAB converter ($\phi_{13} > \phi_{12}$)

Fig. 3.4 Operating waveforms of Two-inductor three-port DAB converter when Port 1 remains at zero power ($\phi_{12} = -\phi_{13}$)

Fig. 3.5 Operating waveforms with Port 3 idling in (a): the conventional three-port DAB converter (b): Two-inductor three-port DAB converter

Fig. 3.6 Control diagram of Two-inductor three-port DAB converter

Fig. 3.7 Different voltage phase reference in Two-inductor three-port DAB converter (a): Port 2 voltage phase reference (b): Port 3 voltage phase reference

Fig. 3.8 5-kW prototype of Two-inductor three-port DAB converter

Fig. 3.9 Steady-state operational simulation results at operating points: (a): ϕ_{12} = 0.890, ϕ_{13} = 0.227 (b): ϕ_{12} = 0.558, ϕ_{13} = 0.244

Fig. 3.10 Simulation result of port power change at step-load change

Fig. 3.11 Simulation result of circulating current in Port 3 left at zero power in (a): the conventional three-port DAB converter (b) Two-inductor three-port DAB converter

Fig. 3.12 Steady-state operational experimental results (a): Port 2 consuming 4.5-kW and Port 3 storing

500 W (b) Port 2 consuming 3-kW from Port 1 transferring 2-kW and Port 3 providing 1-kW

Fig. 3.13 Experimental results of circulating current in Port 3 idling in (a): the conventional three-port DAB converter (b): Two-inductor three-port DAB converter

Fig. 3.14 Step load response in Port 2 changing from 1-kW to 4kW while Port 3 remains at 1-kW

Fig. 3.15 Efficiency curves over change of Port 2 power with Port 3 fixed at 1-kW

Fig. 3.16 Dual-transformer three-port DAB converter

Fig. 3.17 Simplified equivalent circuit of Dual-transformer three-port DAB converter

Fig. 3.18 Steady-state waveforms between Port 1 and Port 2 with Port 3 open

Fig. 3.19 Operating process of Dual-transformer three-port DAB converter with Port 3 open

Fig. 3.20 ZVS range according to voltage gain M: (a): M=1 (b): M=1.2 (c) M=0.8

Fig. 3.21 Magnetizing inductance for different inductor placements (a): in Port 2 (b): in Port 1

Fig. 3.22 Extended ZVS range (a): in Port 1 (b): in Port 2 with the coefficient α=3

Fig. 3.23 Magnetizing inductance utilization for different cases (a): Case 1 (M_{12}<1 and M_{13}<1) (b): Case 2 (M_{12}>1 and M_{13}<1) (c): Case 3 (M_1 <1 and M_{13}>1) (d): Case 4 (M_{12}>1 and M_{13} >1)

Fig. 3.24 3-kW Dual-transformer three-port DAB converter prototype

Fig. 3.25 Steady-state operational simulation results at operating points: (a): ϕ_{12} = 0.244, ϕ_{13} = 0.506 (b): ϕ_{12} = 0.515, ϕ_{13} = 0.235

Fig. 3.26 Simulation result of step-load response

Fig. 3.27 Steady-state experimental results (a): Port 2 taking 1.5-kW, Port 3 consuming 750-W (b) Port 2 taking 750-W, Port 3 consuming 1.5-kW, (c): Port 2 and Port 3 taking 1.5-kW

Fig. 3.28 Step-load response in Port 2 changing from 500 W to 1.5-kW with Port 3 at 1.5-kW

Fig. 3.29 Case 1: Experimental results at turn-on transition without designed magnetizing inductances (a): Port 1, (b): Port 2, (c): Port 3

Fig. 3.30 Case 1: Experimental results at turn-on transition with designed magnetizing inductances (a): Port 1, (b): Port 2, (c): Port 3

Fig. 3.31 Case 2: Experimental results at turn-on transition without designed magnetizing inductances (a): Port 1, (b): Port 2, (c): Port 3

Fig. 3.32 Case 2: Experimental results at turn-on transition without designed magnetizing inductances (a): Port 1, (b): Port 2, (c): Port 3

Fig. 3.33 Case 4: Experimental results at turn-on transition without designed magnetizing inductances (a): Port 1, (b): Port 2, (c): Port 3

Fig. 3.34 Case 4: Experimental results at turn-on transition without designed magnetizing inductances (a): Port 1, (b): Port 2, (c): Port 3

Fig. 3.35 Efficiency curves over change of Port 2 and Port 3 power for Case 1

Fig. 4.1 Schematics of bipolar LVDC distribution system with the proposed back-up converter employing voltage balancing capability with ESS

Fig. 4.2 Converter schematics: (a) Two-inductor three-port DAB converter, (b) The conventional three-port DAB converter

Fig. 4.3 Theoretical operating waveforms of the proposed converter

Fig. 4.4 Control block diagram of the proposed converter with balancing capability for bipolar DC pole voltage levels

Fig. 4.5 Current stress comparison between the conventional converter and the proposed converter in

each port at P_3 = 1.0 p,u fixed: (a) Port 1, (b) Port 2, (c) Port 3

Fig. 4.6 3-kW prototype proposed voltage balancer photograph

Fig. 4.7 Steady state experimental operational waveforms under (a): 3 kW (P_2 = 1.5 kW, P_3 = 1.5 kW) (b): 1.5 kW (P_2 = 1.5 kW, P_3 = 0 W)

Fig. 4.8 Dynamic response experimental waveforms (P_2 = 750 W and P_3 = 500 W to 1.5 kW)

Fig. 4.9 Steady state operational waveforms under the power conditions of P_2 = 750 W and P_3 = 1.5 kW (a) in the proposed converter (b) in the conventional converter

Fig. 4.10 Efficiency curves over output power change at Port 2 (P_3 = 1.5 kW fixed)

Fig. 4.11 Estimated loss comparison at $P_2 = P_3$ = 1.5 kW

List of Tables

TABLE I SYSTEM SPECIFICATIONS AND PARAMETERS FOR CONVENTIONAL THREE-PORT DAB CONVERTER

TABLE II SYSTEM SPECIFICATIONS AND PARAMETERS FOR TWO-INDUCTOR THREE-PORT DAB CONVERTER

TABLE III SYSTEM SPECIFICATIONS AND PARAMETERS FOR DUAL-TRANSFORMER THREE-PORT DAB CONVERTER

TABLE IV CONVERTER PARAMETERS FOR DIFFERENT VOLTAGE GAIN CASES AND DESIGNED MAGNETIZING INDUCTANCES

TABLE V SYSTEM SPECIFICATIONS AND PARAMETERS FOR THE PROPOSED VOLTAGE BALANCER

List of Abbreviations

DAB	Dual-Active-Bridge
DPS	Dual Phase Shift
DSP	Digital Signal Processor
EPS	Extended Phase Shift
ESS	Energy Storage System
EV	Electric Vehicle
LVDC	Low Voltage DC
PI	Proportional-Integral
SPS	Single Phase Shift
TPS	Triple Phase Shift
TZM	Trapezoidal-phase-shift Modulation
ZVS	Zero Voltage Switching

Ⅰ. Introduction

Digital loads requiring DC power have become majority over the last few decades. Electric vehicles (EV), which also need DC power have been developed due to the increase of environmental regulations. Also, as the modern society has been challenged by the depletion of non-renewable energy sources such as fossil fuel, the importance of energy efficiency has been emphasized. Because of the reasons above, which are the increase of DC power consumption and the rise of concern about energy efficiency, DC distribution has been of particular interest and highlighted as one of the future distribution systems [1]. It has more advantages than the conventional AC distribution has, such as lower power loss in the distribution lines without AC resistance, less energy conversion stages and great connectivity of renewable energy sources [1]-[3]. Therefore, DC distribution can achieve higher efficiency and provide better flexibility with the earlier-stated advantages.

The conceptual DC microgrid diagram, one of the DC distribution systems is shown in Fig. 1.1 It has different types of DC loads, renewable energy sources and energy storage systems (ESS). It shows that a DC distribution system needs different scales of DC-DC converters for various loads, distributed

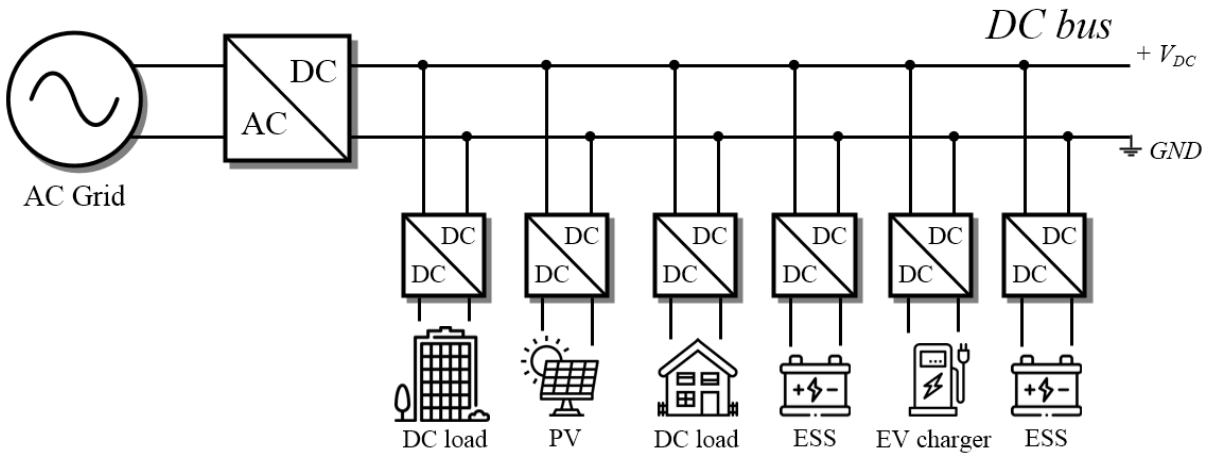

Fig. 1.1 DC microgrid concept diagram with different loads and distributed sources

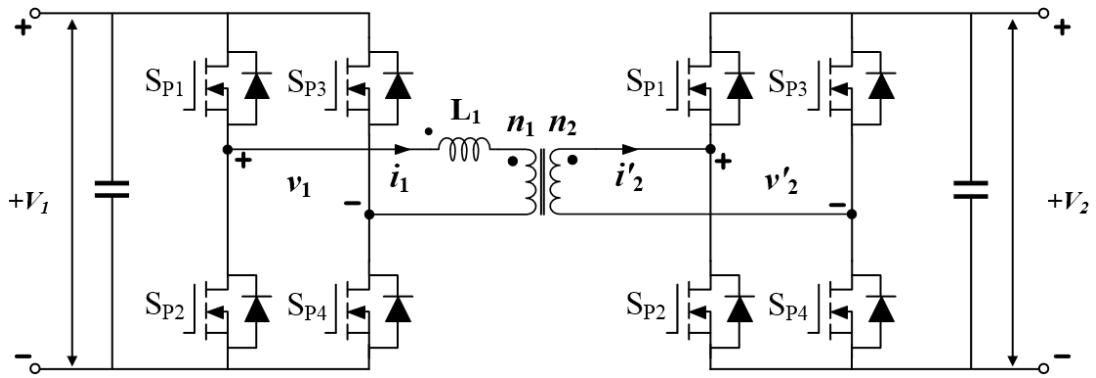

Fig. 1.2 Dual-active-bridge (DAB) converter structure

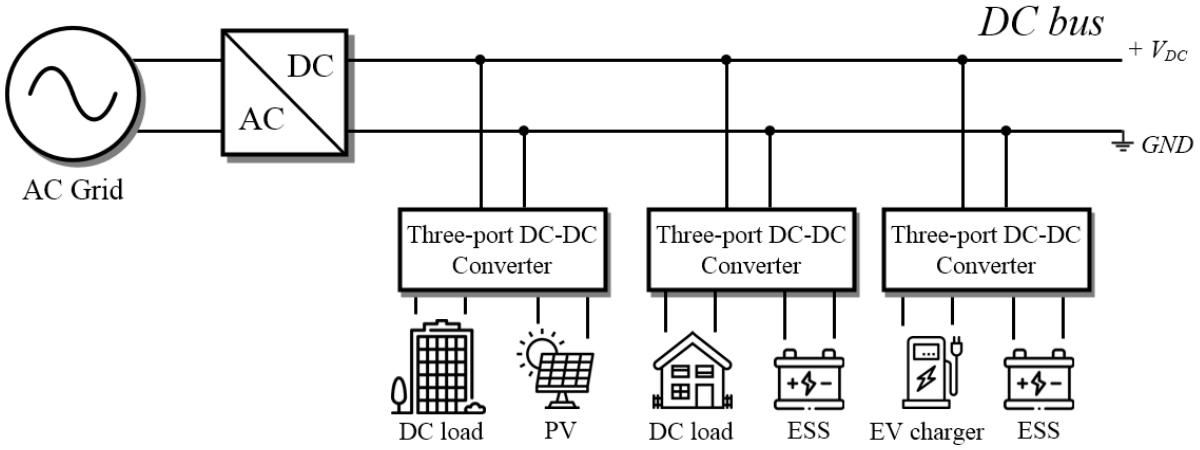

Fig. 1.3 DC microgrid concept diagram with three-port DC-DC converters

energy sources and ESS. Consequently, an important key technology in order to realize a DC microgrid system is high power bidirectional DC-DC conversion [1]-[3]. The dual-active-bridge (DAB) converter as a great candidate topology shown in Fig. 1.2 has been getting attention for high power DC-DC power conversion with a minimal component count. The concept of the DAB converter was firstly introduced in [4]. The DAB converter can transfer high power in both directions with its symmetric structure. It also has a high-frequency transformer, which can match different voltage levels with its turns ratio and meet some safety requirements.

The operational principles of the DAB converter are presented in [4]-[7]. The DAB converter basically transfers power through the series inductance used as a power transfer element with the voltage phase displacement between the two bridges. The bridge voltages are generated by complimentarily turning the diagonal switch pairs, commonly known as the single phase shift (SPS) modulation [4], [5]. Different modulation strategies have been proposed to improve the performance of the DAB converter. the extended phase shift (EPS) modulation, the dual phase shift (DPS) modulation, the triple phase shift (TPS) modulation and the trapezoidal-phase-shift modulation (TZM) have been proposed to increase power conversion efficiency [8]-[11].

The DAB converters can be applied to connect DC units with the DC microgrid with the attractive features above. However, these two-port converters are controlled individually and may require an additional communication bus for certain converters that frequently interface power to each other. This structure causes complexity in the entire system even if the converters are simple to implement with minimal component counts.

Fig. 1.3 illustrates a DC microgrid system with three-port converters. A three-port converter is able to connect two DC units with the grid into one converter. This structure makes the whole system more compact than the structure shown in Fig. 1.1 In other words, the power density of the total system becomes higher. In addition, power switching devices and the corresponding gate drivers are less

required as well as the associated passive components. Also, an auxiliary communication circuit may be removed between certain DC units that regularly interface each other due to the centralized control. Therefore, using three-port converters in a DC microgrid can increase the power density and reduce cost to build up and maintain the system.

This thesis aims to investigate three-port DC-DC converters derived from the DAB converter, which still keep the same important features the DAB converter has, such as bidirectional high power transfer capability and galvanic isolation. The rest of this thesis is organized as follows: Section II introduces the conventional three-port DAB converter and its operational principles and control strategy. Also, a simpler control strategy avoiding use of a look-up table is proposed. In Section III, two advanced three-port DAB converters, Two-inductor three-port DAB converter and Dual-transformer three-port DAB converter are proposed and introduced, respectively. Two-inductor three-port DAB converter can eliminate the power coupling that the conventional converter has without additional control. The topology description and the operational principles are explained and analyzed. The validity of the proposed converter is verified with PSIM, the power circuit simulation software and experimental results. Dual-transformer DAB converter is also able to eliminate the power coupling without extra control. its topology description and operational principles are explained. A magnetizing inductance design method is proposed to extend the zero voltage switching (ZVS) capability. The effectiveness of the magnetizing inductance design is verified with PSIM and experimental results. Lastly, an isolated voltage balancer employing ESS in bipolar low voltage DC (LVDC) distribution is proposed using Two-inductor three-port DAB converter in Section IV. Its structure and theoretical analysis are presented. The validity of the proposed voltage balancer is verified with PSIM and experimental results.

Ⅱ. Conventional Three-port Dual-active-bridge (DAB) Converter

In this chapter, the description, the operational principles and control strategies of the conventional three-port DAB converter are presented.

2.1 Theoretical Analysis

Fig. 2.1 illustrates the conventional three-port DAB converter, which is an extended structure of the DAB converter [12]-[14]. This topology consists of three full-bridges, three inductances and a high-frequency transformer. The full-bridges are replaceable with half-bridges depending on the application. The inductances can be realized with the leakage inductances of the high-frequency transformer and also, they can be designed with external inductors. The three ports are magnetically combined with the transformer. The high-frequency does not only integrate three ports but also provide galvanic isolation for safety and match voltage differences among the ports.

The diagonal opposite switch pairs S_{x1}, S_{x4} and S_{x2}, S_{x3} ($x = P$, S and T) complementarily operate to generate two-level square-wave voltages with 50 % duty ratio at a fixed switching frequency. The switching operation stated above can be simply described as an AC square-wave voltage source with the amplitude of V_1. Therefore, one port (i.e., Port 1) can be simplified as depicted in Fig. 2.2. In the same manner, the other ports can be represented as AC square-wave voltage sources.

As depicted in Fig. 2.1, all the ports are connected to the high-frequency transformer in series. The

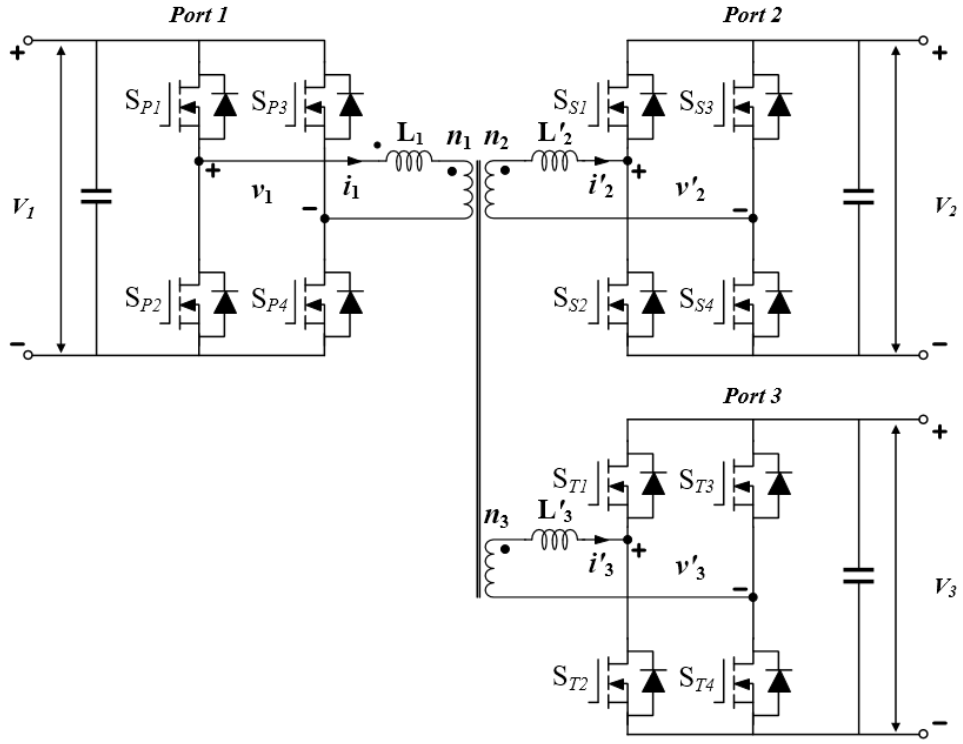

Fig. 2.1 Conventional three-port DAB converter

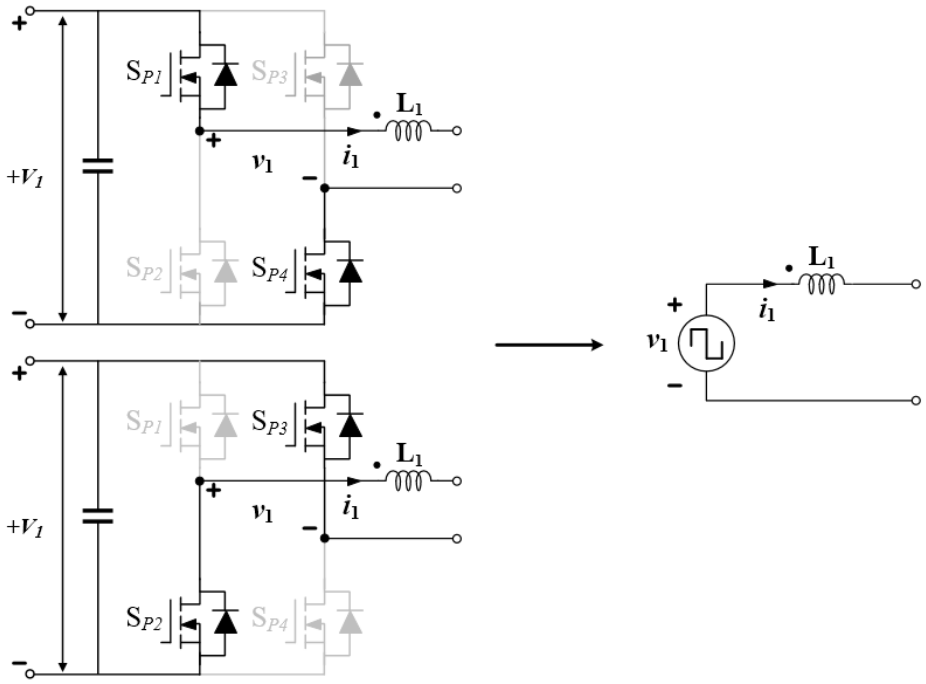

Fig. 2.2 Simplified port operated with 50 % duty ratio at a fixed switching frequency

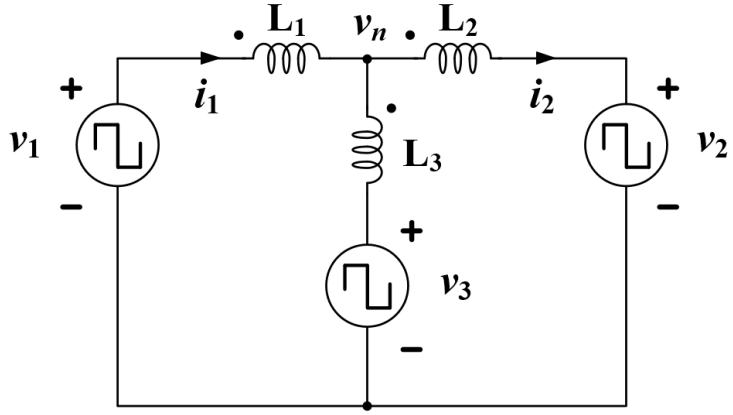

Fig. 2.3 Wye-connected equivalent circuit for conventional three-port DAB converter

three-winding transformer can be described as a wye connected circuit since the ports are connected in series [15]. Fig. 2.3 illustrates the wye-connected equivalent circuit referred to the Port 1 side with the transformer turns ratios n_{12} (n_1/n_2) and n_{13} (n_1/n_3), where $v_2 = n_{12}v'_2$, $v_3 = n_{13}v'_3$, $i_2 = i'_2/n_{12}$, $i_3 = i'_3/n_{13}$, $L_2 = n_{12}^2 L'_2$ and $L_3 = n_{13}^3 L'_3$. The neutral voltage v_n can be derived by the principle of superposition as below: (Details of the derivation follow in APPENDIX.A)

$$v_n(\omega t) = \frac{L_1L_2v_3(\omega t) + L_1L_3v_2(\omega t) + L_2L_3v_1(\omega t)}{L_1L_2 + L_1L_3 + L_2L_3} \tag{1}$$

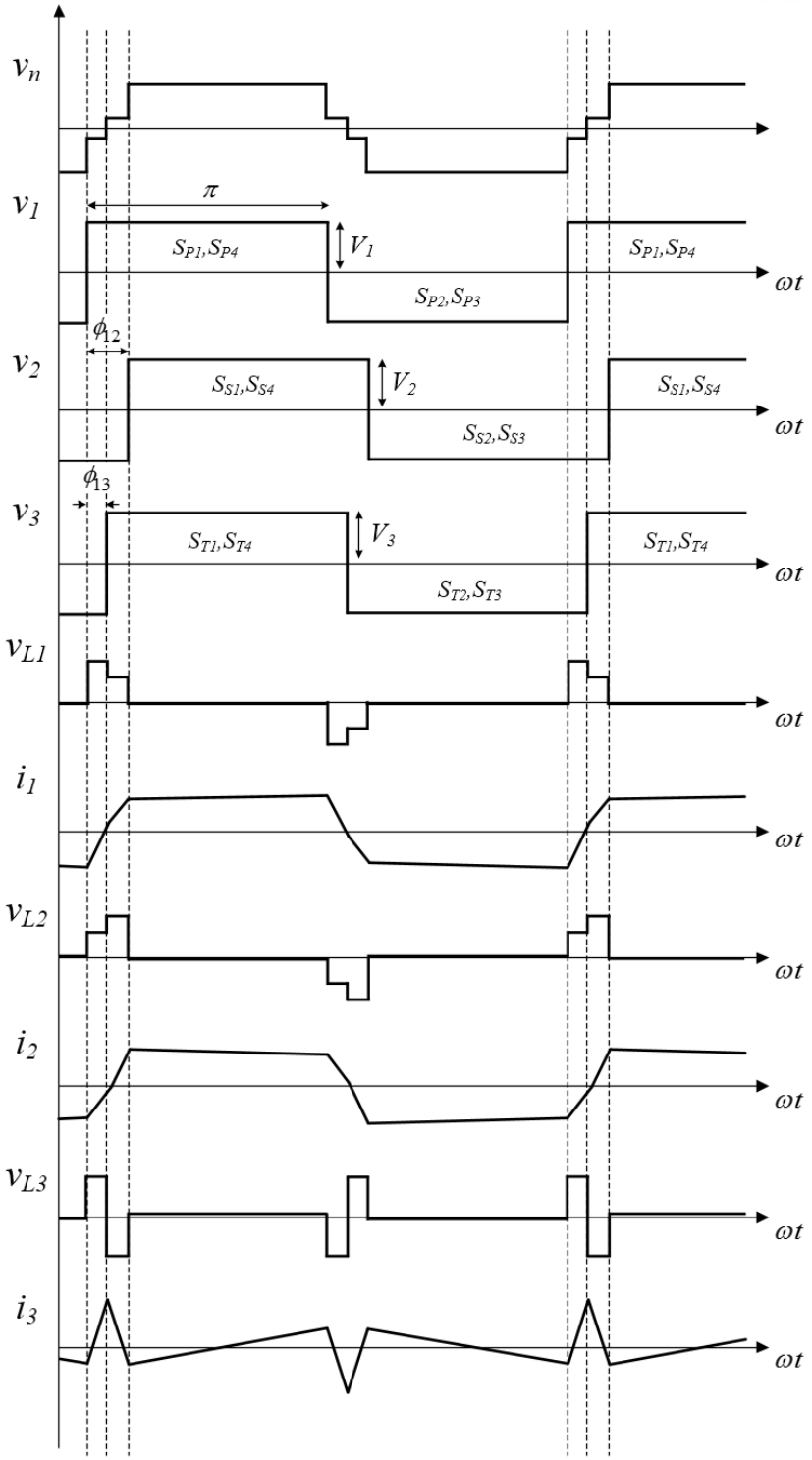

Fig. 2.4 Operating waveforms of the conventional three-port DAB converter ($\phi_{13} > \phi_{12}$)

Since the neutral voltage v_n can be derived, voltages applied across the inductances and the port currents can be calculated. Therefore, the operating waveforms of the conventional three-port DAB converter can be illustrated as depicted in Fig. 2.4 However, it is difficult to analyze power flow among the three

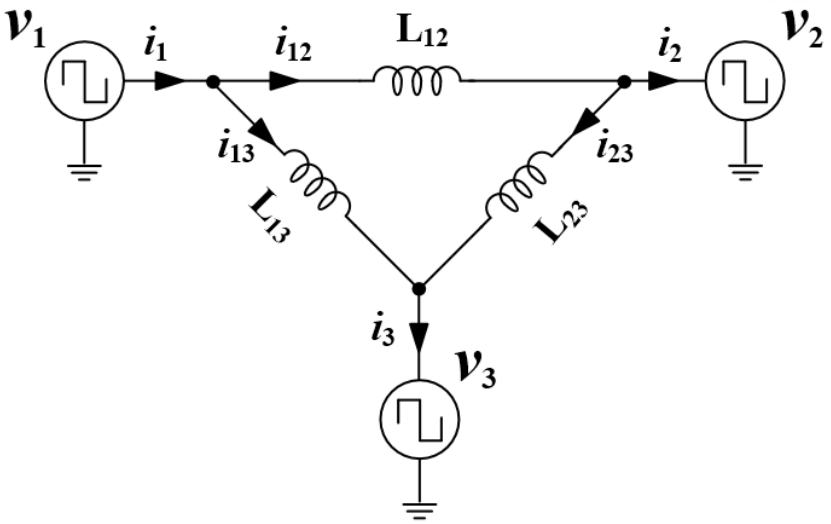

Fig. 2.5 Delta-connected equivalent circuit for conventional three-port DAB converter

ports since the neutral voltage v_n is a function of the port voltages v_1, v_2 and v_3. The wye-delta transformation can be applied for simple analysis [12], [13]. It is advantageous to analyze the relation between the ports. The delta-connected equivalent circuit with the primary port (Port 1) referred parameters can be as depicted in Fig. 2.5 The square-wave voltages sources are remained as the same in the wye form. The effective inductances of L_{12} [$=(L_1L_2 + L_1L_3 + L_2L_3)/L_3$], L_{13} [$=(L_1L_2 + L_1L_3 + L_2L_3)$ / L_2] and L_{23} [$=(L_1L_2 + L_1L_3 + L_2L_3)/L_1$] can be derived as power transfer elements between the ports.

As the equivalent circuit shown in Fig. 2.3 is transformed into the delta connection, it can be considered as three two-port DAB converters. Therefore, the total power transfer can be determined by the principle of superposition. Each port-to-port power transfer can be derived as follows [4], [5].

$$P_{12} = \frac{V_1 V_2}{2\pi^2 f_{sw} L_{12}} \phi_{12}(\pi - |\phi_{12}|) \tag{2}$$

$$P_{13} = \frac{V_1 V_3}{2\pi^2 f_{sw} L_{13}} \phi_{13}(\pi - |\phi_{13}|) \tag{3}$$

$$P_{23} = \frac{V_2 V_3}{2\pi^2 f_{sw} L_{23}} (\phi_{13} - \phi_{12})(\pi - |\phi_{13} - \phi_{12}|) \tag{4}$$

where, P_{xy} denotes power from x port to y port (x, y = 1, 2 and 3). V_1, V_2 and V_3 are the magnitude of each port, f_{sw} is the operating switching frequency, and ϕ_{12} and ϕ_{13} are the phase shift variables of Port 2 and Port 3 with respect to the reference phase of Port 1. The phase shift range can be changed from -π to π, but it has to be limited as from -π/2 to π/2. Because the limited range can curve the whole power capability of the converter, and if the phase is shifted more than π/2, reactive power increases more than active power, which causes poor conversion efficiency as shown in Fig. 2.6 [6], [7]. Also, it shows that

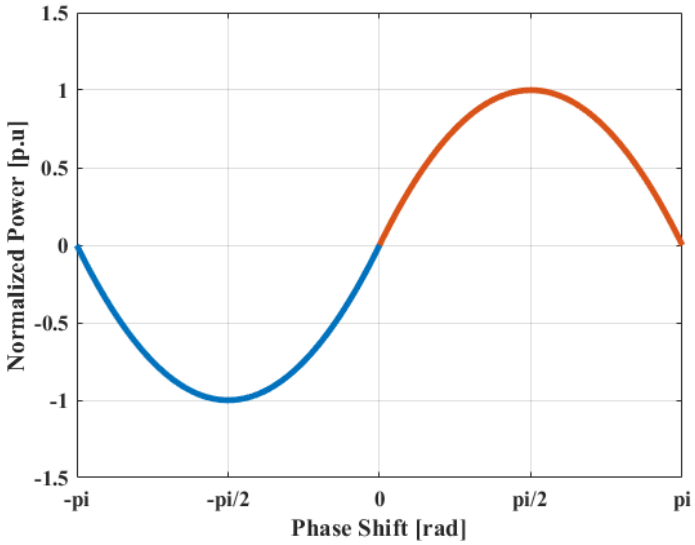

Fig. 2.6 Power curve over phase shift for port-to-port

it can bidirectionally transfer power with the phase shift value. Since each port-to-port power is determined as in the equations (2), (3) and (4). The total power flow in each port can be determined as below:

$$\begin{aligned} P_1 &= P_{12} + P_{13} \\ P_2 &= -P_{12} + P_{23} \\ P_3 &= -P_{13} - P_{23} \end{aligned} \tag{5}$$

where, P_x is a total port power in Port x (x = 1, 2 and 3). Fig. 2.7 shows that the three port powers over the phase shift values ϕ_{12} and ϕ_{13} limited from -π/2 to π/2 for the same reason stated above. It denotes that the three ports are able to transfer power in every way since it has a symmetric structure.

2.2 Control Strategy

The conventional three-port DAB converter suffers from the power correlation [12], [13]. To eliminate the power correlation in the converter, a decoupling control algorithm is proposed in [12]. However, it uses a look-up table of decoupling matrices at every operating point of the converter, which brings difficulty to control. In this subchapter, one decoupling matrix that can cover the whole load rage is proposed [16].

The input-output power relation has to be analyzed to control the converter. Each port power equation is derived by the equations (2)-(5) as below:

$$P_1 = \frac{V_1 V_2 L_3 \phi_{12}(\pi - |\phi_{12}|) + V_1 V_3 L_2 \phi_{13}(\pi - |\phi_{13}|)}{2\pi^2 f_{sw}(L_1 L_2 + L_1 L_3 + L_2 L_3)} \tag{6}$$

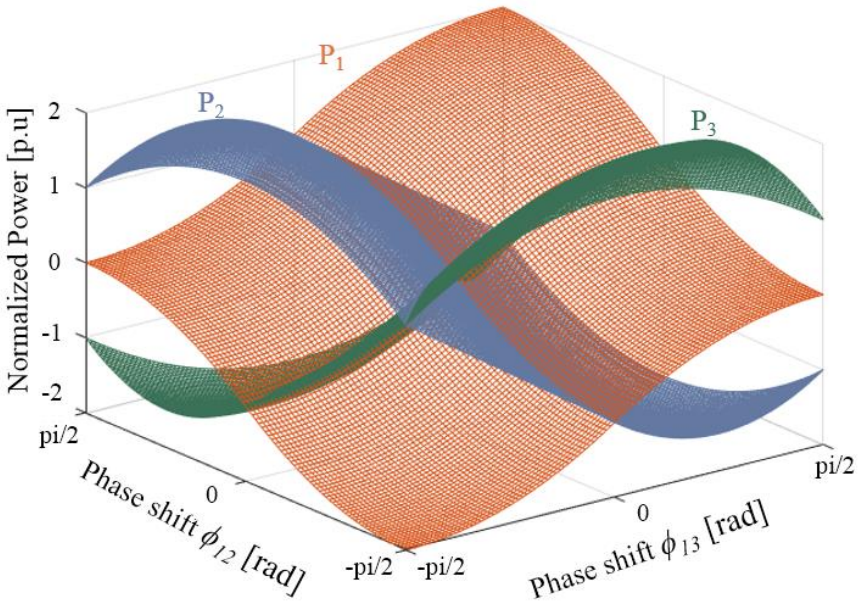

Fig. 2.7 Each port power curve over phase shift ϕ_{12} *and* ϕ_{13}

$$P_2 = \frac{V_1 V_2 L_3 \phi_{12}(\pi - |\phi_{12}|) + V_2 V_3 L_1 (\phi_{12} - \phi_{13})(\pi - |\phi_{12} - \phi_{13}|)}{2\pi^2 f_{sw}(L_1 L_2 + L_1 L_3 + L_2 L_3)} \tag{7}$$

$$P_3 = \frac{V_1 V_3 L_2 \phi_{13}(\pi - |\phi_{13}|) + V_2 V_3 L_1 (\phi_{13} - \phi_{12})(\pi - |\phi_{13} - \phi_{12}|)}{2\pi^2 f_{sw}(L_1 L_2 + L_1 L_3 + L_2 L_3)} \tag{8}$$

The delta-connected equivalent circuit transformed from the wye form is only used for power flow analysis since it can be seen as three two-ports DAB converters, but the three ports are combined with the transformer in series, which denotes that physically, the converter itself has the wye-connected form. Therefore, the internal circulating power in the delta connection does not exist. If loss is ignored, the equation below can be satisfied:

$$P_1 + P_2 + P_3 = 0 \tag{9}$$

As the equation (9) notes, the total sum of power in the converter is zero.

The three port powers are controlled by the two control variables ϕ_{12} and ϕ_{13}. When two port powers are determined, the other port power is automatically determined according to the equation (9). The port powers can be derived by their corresponding currents if the port voltages regulated are assumed to be constant. A system matrix that represent the input-output relation can be defined by setting the control variable ϕ_{12} and ϕ_{13} as the inputs and the port currents I_2 and I_3 as the outputs. The port currents I_2 and I_3 can be derived by dividing the equations (7) and (8) by their corresponding voltages.

$$I_2 = \frac{V_1 L_3 \phi_{12}(\pi - |\phi_{12}|) + V_3 L_1 (\phi_{12} - \phi_{13})(\pi - |\phi_{12} - \phi_{13}|)}{2\pi^2 f_{sw}(L_1 L_2 + L_1 L_3 + L_2 L_3)} \tag{10}$$

$$I_3 = \frac{V_1 L_2 \phi_{13}(\pi - |\phi_{13}|) + V_2 L_1 (\phi_{13} - \phi_{12})(\pi - |\phi_{13} - \phi_{12}|)}{2\pi^2 f_{sw}(L_1 L_2 + L_1 L_3 + L_2 L_3)} \tag{11}$$

In order to express the equations (10) and (11) as linear functions of the phase shift values ϕ_{12} and ϕ_{13}, which are the input variables, linearization is needed. The quadratic terms in the equations can be simplified with the Fourier series:

$$\phi(\pi - \phi) \approx \frac{8}{\pi} \sin\phi \tag{12}$$

By substituting the simplified quadratic terms transformed from the equation (12) into the equations (10) and (11), and applying the Taylor series on them at an operating point ϕ_{12op} and ϕ_{13op}. The linearized equations are as follows:

$$I_2 \cong G_{11}\phi_{12} + G_{12}\phi_{13} \tag{13}$$

$$G_{11} = \frac{V_1 L_3 \cos(\phi_{12op}) + V_3 L_1 \cos(\phi_{12op} - \phi_{13op})}{(1/4)\pi^3 f_{sw} K} \tag{14}$$

$$G_{12} = -\frac{V_3 L_1 \cos(\phi_{12op} - \phi_{13op})}{(1/4)\pi^3 f_{sw} K} \tag{15}$$

$$I_3 \cong G_{21}\phi_{12} + G_{22}\phi_{13} \tag{16}$$

$$G_{21} = -\frac{V_2 L_1 \cos(\phi_{13op} - \phi_{12op})}{(1/4)\pi^3 f_{sw} K} \tag{17}$$

$$G_{22} = \frac{V_1 L_2 \cos(\phi_{13op}) + V_2 L_1 \cos(\phi_{13op} - \phi_{12op})}{(1/4)\pi^3 f_{sw} K} \tag{18}$$

$$K \triangleq L_1 L_2 + L_1 L_3 + L_2 L_3 \tag{19}$$

Therefore, the system matrix G can be defined as in the equation (20) below:

$$\begin{bmatrix} I_2 \\ I_3 \end{bmatrix} = \begin{bmatrix} G_{11} & G_{12} \\ G_{21} & G_{22} \end{bmatrix} \begin{bmatrix} \phi_{12} \\ \phi_{13} \end{bmatrix} = G\vec{\phi} \tag{20}$$

The system off-diagonal elements G_{12} and G_{21} are the causes making the port power coupling. In other words, change of one control variable affects the two output ports. Overshoot, undershoot and unwanted

power flow can occur in a port that does not have load change since power cannot be independently controlled due to the coupling elements G_{12} and G_{21}. A decoupling matrix has to be defined in order to remove the off-diagonal elements of the system matrix G. The decoupling matrix can be defined as the inverse matrix of the system matrix G [17].

$$D \triangleq \begin{bmatrix} D_{11} & D_{12} \\ D_{21} & D_{22} \end{bmatrix} = G^{-1} = \frac{1}{G_{11}G_{22} - G_{12}G_{21}} \begin{bmatrix} G_{22} & -G_{12} \\ -G_{21} & G_{11} \end{bmatrix} \tag{21}$$

In order to use the decoupling matrix approach, the system matrix has to be a non-singular matrix to define the inverse matrix in the equation (21) on every occasion. That is to say the determinant of the system matrix G must not be zero. The determinant of the system matrix G can be derived as follows:

$$|G| = G_{11}G_{22} - G_{12}G_{21} \tag{22}$$

All the parameters of the converter have positive values such as voltages, inductances and switching frequency etc. Also, according to (14), (15), (17) and (18), G_{12} and G_{21} values are included in G_{11} and G_{22}. It means that the term, $G_{12}G_{21}$ are smaller than $G_{11}G_{22}$ on any occasion. Therefore, the determinant $|G|$ is always greater than zero, which means a decoupling matrix exist at any operating point. New control variables ϕ^*_{12} and ϕ^*_{13} can be defined by applying the decoupling matrix in the control loop. The equation (23) above depicts that the system gain matrix becomes a unit matrix due to the decoupling matrix. As a result, the system can independently transfer power to each load with decoupling matrices

$$\begin{aligned} \begin{bmatrix} I_2 \\ I_3 \end{bmatrix} &= \begin{bmatrix} D_{11} & D_{12} \\ D_{21} & D_{22} \end{bmatrix} \begin{bmatrix} G_{11} & G_{12} \\ G_{21} & G_{22} \end{bmatrix} \begin{bmatrix} \phi^*_{12} \\ \phi^*_{13} \end{bmatrix} \\ &= \begin{bmatrix} 1 & 0 \\ 0 & 1 \end{bmatrix} \begin{bmatrix} \phi^*_{12} \\ \phi^*_{13} \end{bmatrix} \end{aligned} \tag{23}$$

stored in a look-up table at every operating point, which can be simply illustrated in Fig. 2.8 as a control block diagram. However, calculating and storing all the inverse matrices of the system matrix G may be a burden to the controller which is likely to increase the controller cost as well as complexity in control.

Operating range of the DAB converter should not be used from - π/2 up to π/2 but from -π/4 up to π/4 for better performance [5], [18]. Decoupling matrix element values can be plotted as illustrated in Fig. 2.9 with the design methodology presented in [5], [18]. The maximum change rate of decoupling element values is 8.2 %, which does not change significantly. Therefore, one decoupling matrix that is calculated at a nominal operating point can effectively decouple the conventional converter system for

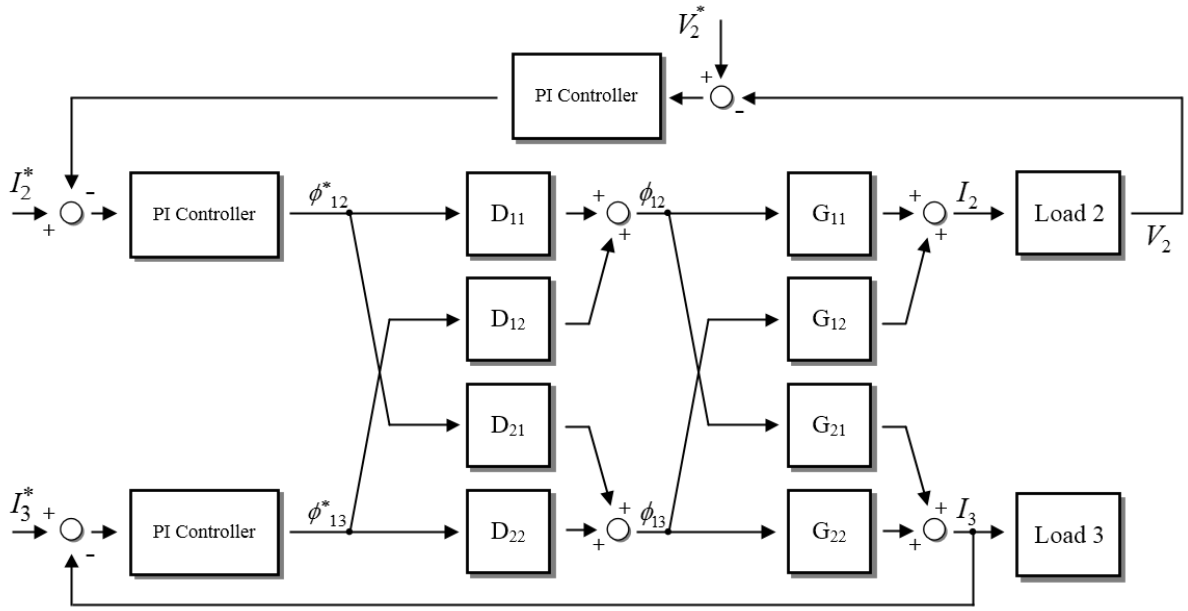

Fig. 2.8 Independent power control algorithm block diagram

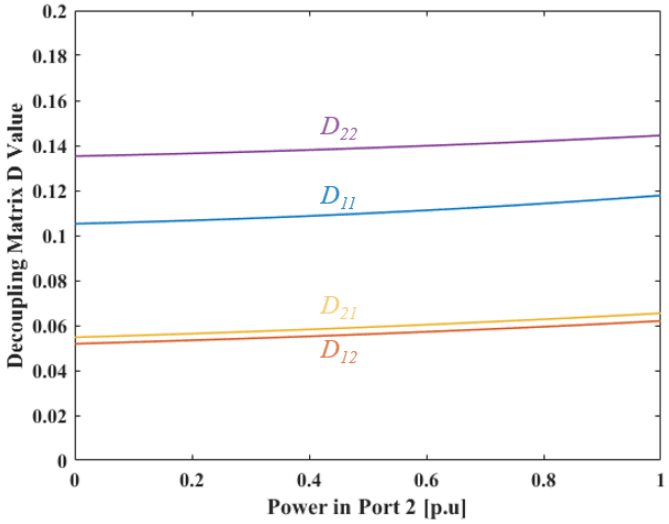

Fig. 2.9 Variations of decoupling matrix elements over Port 2 power under Port 3 power fixed to 1.0 p.u

the whole operating range.

2.3 Simulation Results

A DC microgrid has a variety of DC units such as DC loads, distributed energy sources and ESS. To verify the effectiveness of the three-port DAB converter and its decoupling control strategy, a 1-kW converter interconnecting a load and ESS with the DC bus is used and implemented in the PSIM circuit simulator. The converter is designed with the parameters listed in TABLE 1 and composed of three

TABLE I SYSTEM SPECIFICATIONS AND PARAMETERS FOR CONVENTIONAL THREE-PORT DAB CONVERTER

Parameter	Symbol	Value
Rated power	-	1 kW
Port 1 voltage (DC bus)	V_1	380 V
Port 2 voltage (DC load)	V'_2	380 V
Port 3 voltage (ESS)	V'_3	60 V
Power inductor	L_1	25.5 μH
	L'_2	25.5 μH
	L'_3	1 μH
Turns ratio	n_{12} (n_1/n_2)	1
	n_{13} (n_1/n_3)	6
Switching frequency	f_{sw}	50 kHz

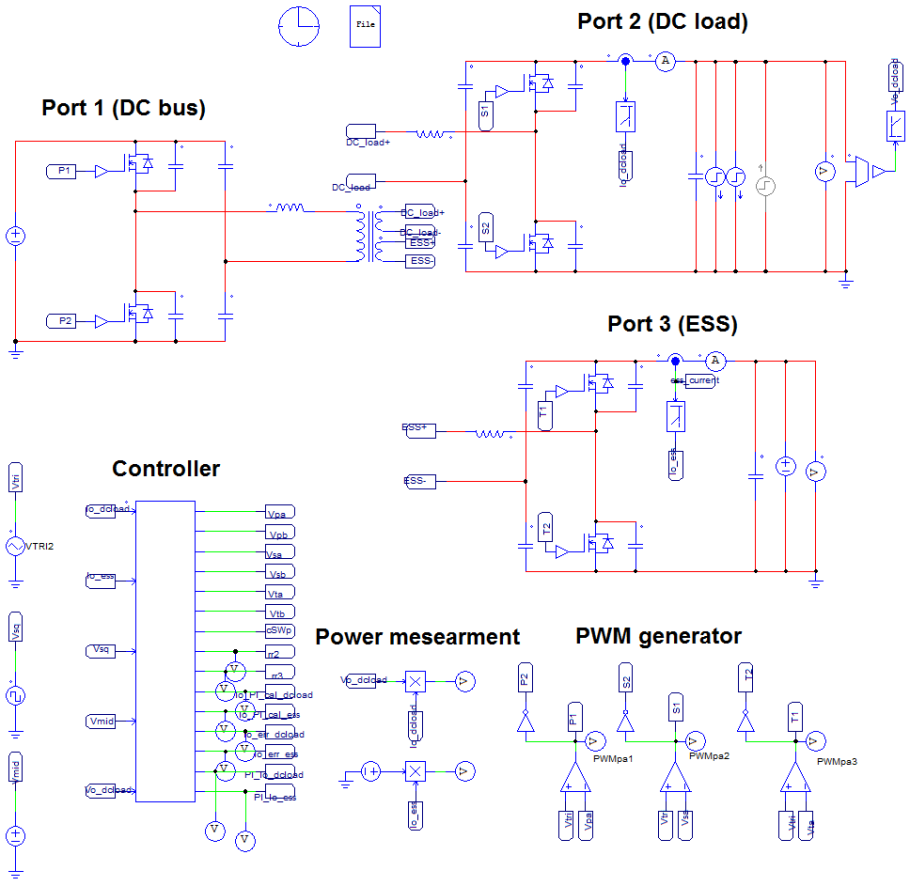

Fig. 2.10 Conventional three-port DAB converter realized in PSIM

half-bridge cells for simple control and the least component number.

Fig. 2.10 shows the three-port DAB converter using a half-bridge cell for each port in PSIM. The control strategy is the same as the control strategy shown in Fig. 2.8. The voltage controller speed for

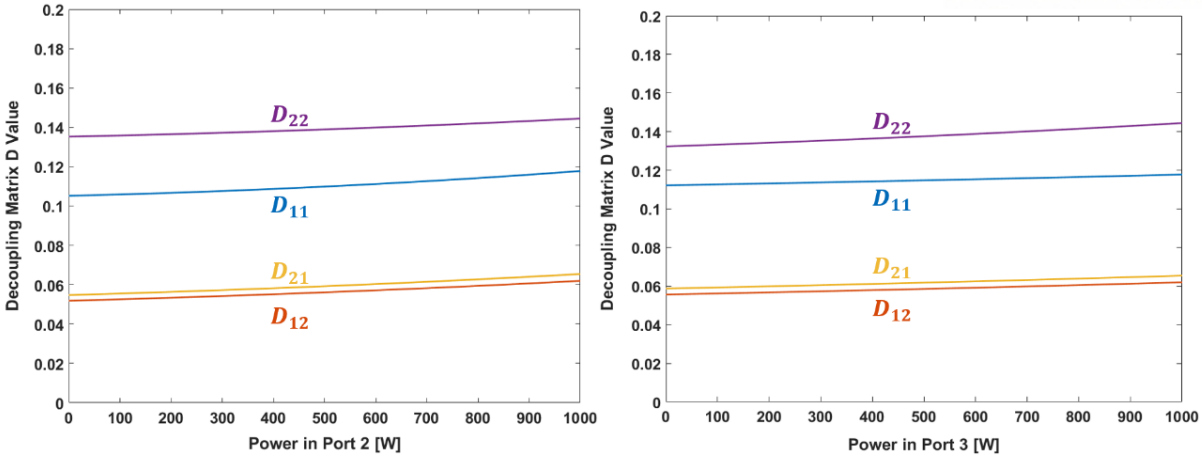

(a) (b)

Fig. 2.11 Variations of decoupling matrix elements over power: (a) under changing Port 2 and fixing Port 3 to 1 kW, (b) under changing Port 3 and fixing Port 2 to 1 kW

Port 2 is set 10 times slower than that of the current controller for Port 2 in order to avoid interference between the two controllers. Fig. 2.11 illustrates the variations of decoupling matrix elements over power change of each port. The maximum change rate of decoupling matrix elements is 8.3 % with the design parameters stated above. Therefore, one decoupling matrix calculated at a nominal operating point can be used, where P_2 = 1 kW and P_3 = 0 W in this case as ESS often idles.

Fig. 2.12 depicts that the steady-state operational simulation results at different operating points. It shows that the converter can transfer power by the voltage phase difference with respect to the reference voltage phase. Fig. 2.12 (a) illustrates that Port 2 absorbs 1-kW power while Port 3 stores 500 W. The Port 2 voltage v'_2 and the Port 3 voltage v'_3 lag behind the reference voltage, the Port 1 voltage v_1 by the phase displacement values ϕ_{12} = 0.372 and ϕ_{13} = 0.329, respectively. Fig. 2.12 (b) shows that Port 2 absorbs 1-kW power while Port 3 remains at zero power with the phase shift values ϕ_{12} = 0.262 and ϕ_{13} = 0.130. It shows one port is able to idle with circulating current while the other port takes power from the source.

Fig. 2.13 (a) and (b) shows the simulation results without decoupling control and with the decoupling control strategy respectively. In the simulation, the Port 3 power is fixed at zero power and Port 2 changes power from 380 to 1 kW at 0.1 sec and changes power from 1 kW to 100 W at 0.15 sec. As depicted in Fig. 2.13 (a), when Port 2 changes its power at 0.1 sec and 0.15 sec, control in Port 3 is interfered. As a result, unwanted power occurs in Port 3. Fig. 2.13 (b) shows that the same simulation Fig. 2.14 shows the waveforms to verify the effectiveness of the proposed method at the transient times of the experiments depicted in Fig. 2.13. Fig. 2.14 (a) illustrates effect on Port 3 remaining at zero power when the Port 2 power step-ups from 380 W to 1 kW. Port 3 has -107-W of unwanted power without the proposed method, whereas Port 3 has only 4.75-W of unwanted power with the proposed

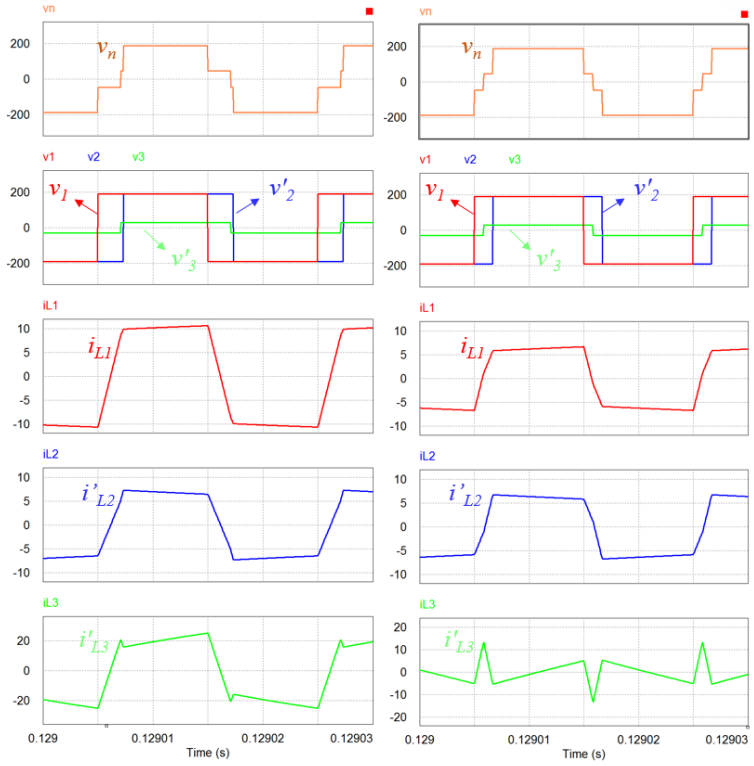

(a) (b)

Fig. 2.12 Steady-state operational simulation results at operating points: (a): $\phi_{12} = 0.372$, $\phi_{13} = 0.329$ (b): $\phi_{12} = 0.262$, $\phi_{13} = 0.130$

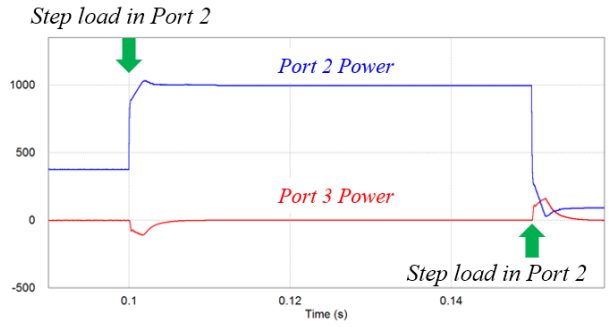

(a)

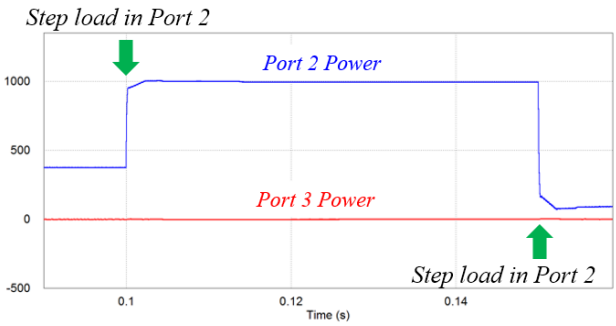

(b)

Fig. 2.13 Simulation results of Port 2 and Port 3 power control: (a) without decoupling strategy (b) with decoupling strategy

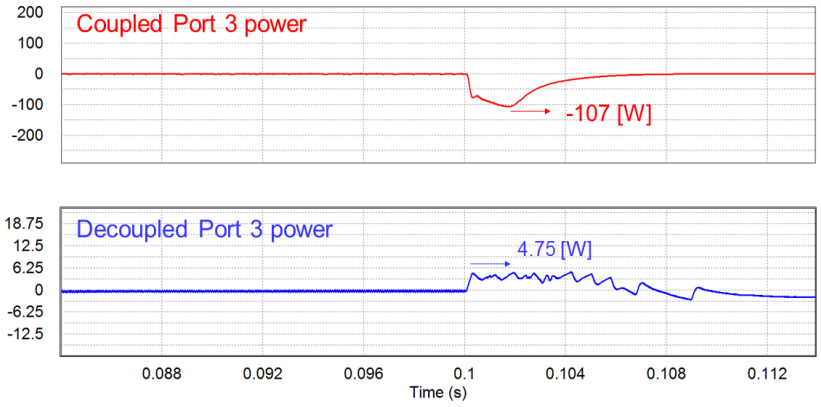

(a)

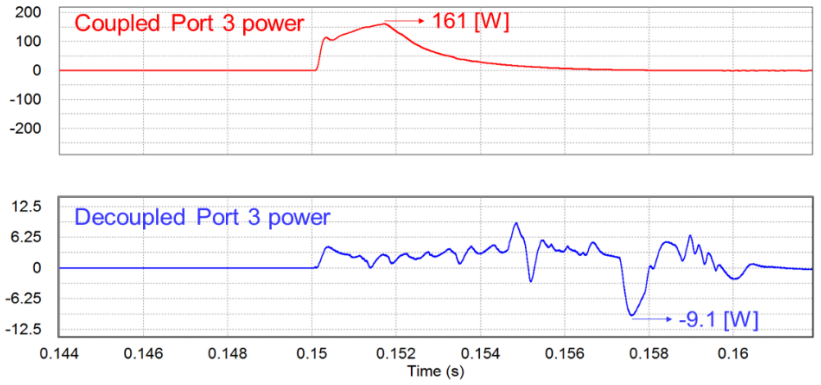

(b)

Fig. 2.14 Effect on Port 3 control when the load of Port 2 changes: (a) 380 W to 1000 W at t = 0.1 sec, (b) 1 kW to 100 W at t = 0.15 sec

method. Fig. 2.14 (b) depicts effect on Port 3 idling when the Port 2 power step-downs from 1 kW to 100 W. Port 3 has 161-W of unwanted power without the proposed method, whereas Port 3 has only -9.1-W with the proposed method. The simulation results show that the interference has been reduced by 95.5 % and 93.3 % respectively.

The conventional three-port DAB converter and its control strategy are presented in this chapter. The topology consists of one high-frequency transformer, which combines all the three ports, three power coupling inductors and three bridge cells. The converter can be simply analyzed with the delta-connected equivalent circuit showing relation between each port. Power can be transferred by corresponding phase displacement value with respect to the reference voltage. A simple decoupling power control strategy is proposed, which only uses one decoupling matrix. It can effectively decouple the system over a wide load range with one decoupling matrix, which can reduce complexity to control.

Ⅲ. Advanced Three-port DAB Converter

In this chapter, two advanced three-port DAB converters are proposed. Proposed structures, operational principles and their advantages over the conventional three-port DAB converter are explained and analyzed in the following chapters.

3.1 Two-inductor three-port DAB converter

Two-inductor three-port DAB converter that can be independently controlled without complex decoupled control is proposed in the chapter. In addition, it can increase power density by removing one power inductor and decrease circulating current in a battery connected port when it remains at zero power. The effectiveness of the proposed converter is verified with a 5-kW prototype converter.

3.1.1 Proposed Converter Structure

Fig. 3.1 illustrates Two-inductor three-port DAB converter, the proposed converter [19]. It consists of three full bridges, which can be replaced with half bridges. A high-frequency transformer that interconnects the three bridge cells provides galvanic isolation. Two ports have series inductance. The series inductance can be utilized with the leakage inductance of the transformer as well as with external

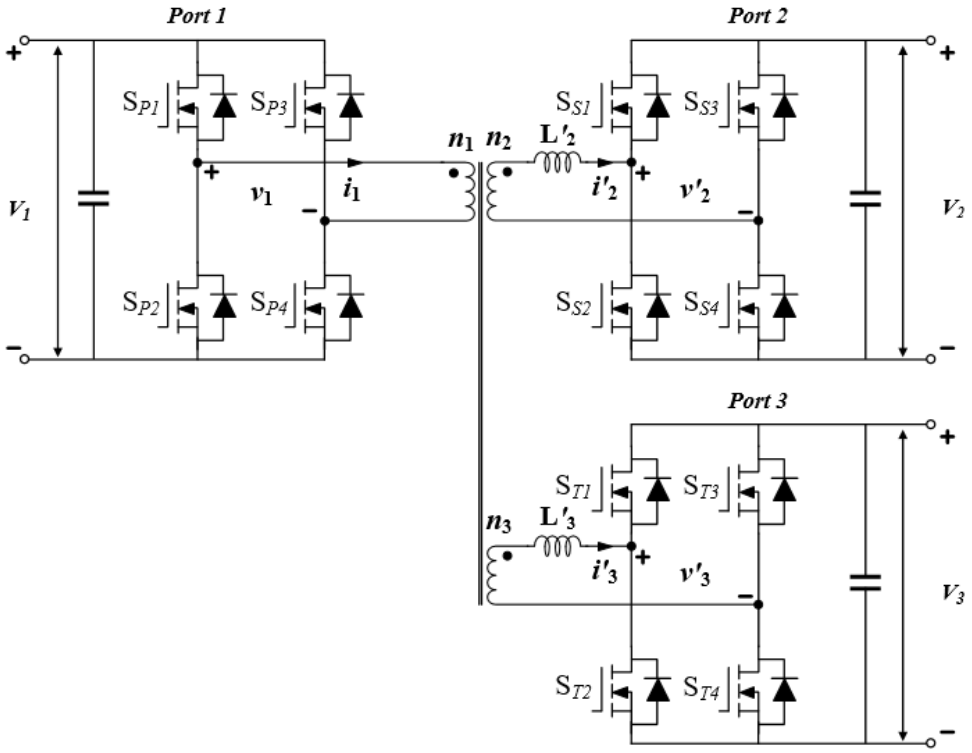

Fig. 3.1 Two-inductor three-port DAB converter

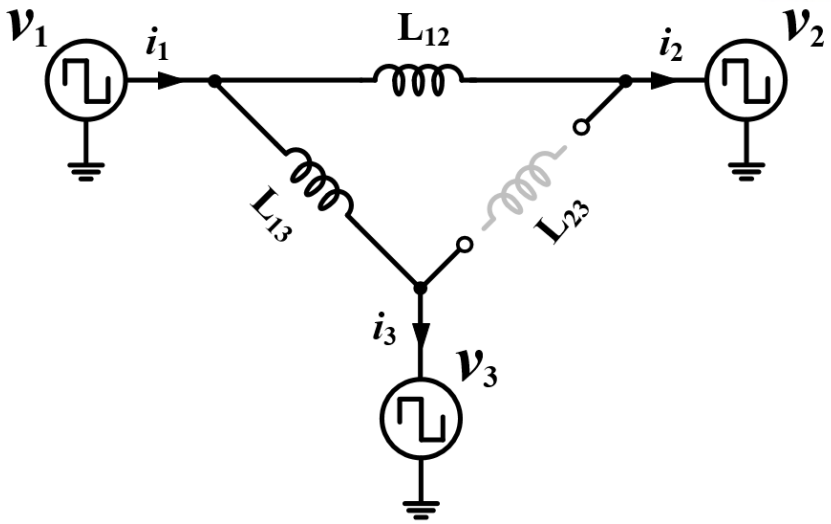

Fig. 3.2 Delta-connected equivalent circuit for Two-inductor three-port DAB converter

inductors. However, the other port does not have power transfer inductance, which is the structure difference compared with the conventional three-port DAB converter. For example, in Fig. 3.1, two ports Port 2 and Port 3 have series inductance, whereas Port 1 does not have one. This different configuration brings significant advantages over the conventional three-port DAB converter. Also, it does not lose any of the key features such as bidirectional power flow capability, high power density and electric isolation among the ports, which the conventional three-port DAB converter has.

3.1.2 Theoretical Analysis

The same manner applied to the conventional three-port DAB converter can be also used to analyze the proposed converter. The diagonal opposite switch pairs S_{x1}, S_{x4} and S_{x2}, S_{x3} (x = P, S and T) complementarily switch to create two-level square-wave voltages with 50 % duty ratio at a fixed switching frequency. It can describe the three bridge cells as AC square-wave voltage sources with the amplitude of the corresponding capacitor voltage. The three-winding transformer can be expressed as wye connection. For simpler analysis, the wye-delta transformation can be applied. Fig. 3.2 depicts the delta transformed equivalent circuit of the proposed converter referred to the Port 1 side with the transformer turns ratios n_{12} (n_1/n_2) and n_{13} (n_1/n_3), where $v_2 = n_{12}v'_2$, $v_3 = n_{13}v'_3$. The effective inductances of L_{12} [=($L_1L_2 + L_1L_3 + L_2L_3$)/L_3], L_{13} [=($L_1L_2 + L_1L_3 + L_2L_3$) / L_2] and L_{23} [=($L_1L_2 + L_1L_3 + L_2L_3$)/L_1] can be derived as power transfer elements between the ports, where $L_2 = n_{12}^2L'_2$ and $L_3 = n_{13}^3L'_3$. However, In the proposed converter, the inductance L_1 is assumed to be zero. As a result, the effective inductance between Port 2 and Port 3 becomes infinite:

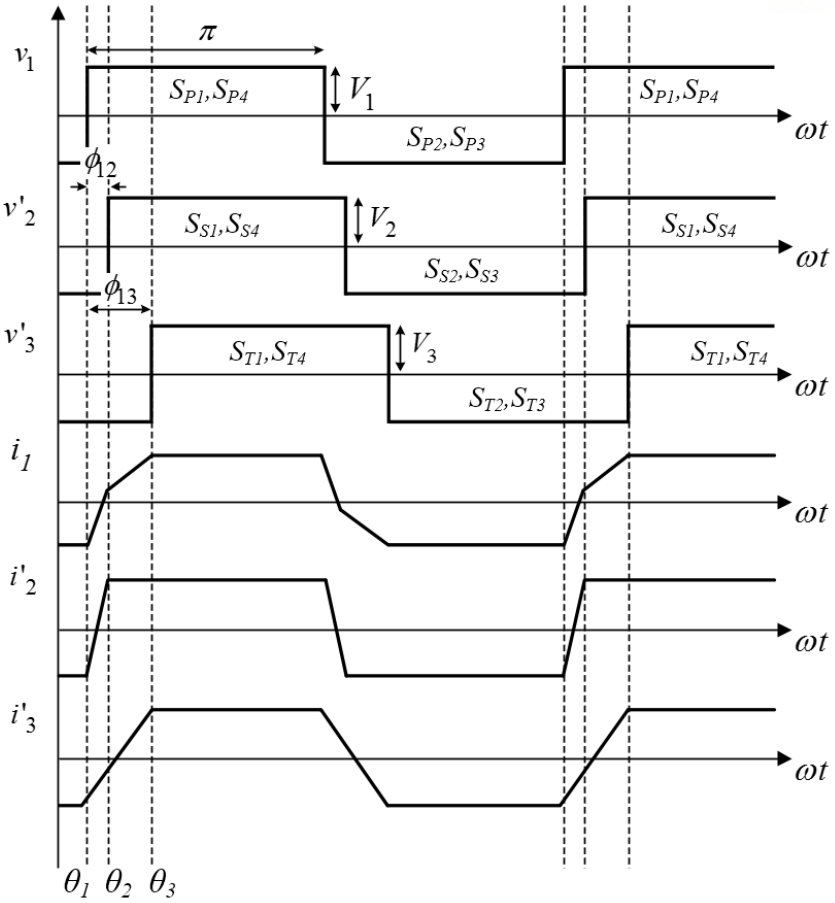

Fig. 3.3 Operating waveforms of Two-inductor three-port DAB converter ($\phi_{13} > \phi_{12}$)

$$L_{23} = \frac{L_1L_2 + L_1L_3 + L_2L_3}{L_1} \cong \infty \tag{24}$$

The impedance between the two ports, Port 2 and Port 3 becomes infinite due to the equation (24). In other words, the power transfer path between them is removed. Considering the fact that it has the infinite impedance between Port 2 and Port 3, theoretical operational waveforms can be as illustrated in Fig. 3.3. As the proposed converter is based on the DAB converter, power is transferred with the voltage phase shift values ϕ_{12} and ϕ_{13} through the series inductance. The voltage phase shift value ϕ_{12} only determines power between Port 1 and Port 2. Likewise, the voltage phase shift value ϕ_{13} determines power between Port 1 and Port 3. Since L_{23} is assumed to be infinite, the phase displacement value $|\phi_{13} - \phi_{12}|$ does not influence power transfer in the proposed converter. Consequently, the power transfer equations of the proposed converter can be derived as below:

$$P_{12} = \frac{V_1V_2}{2\pi^2 f_{sw}L_{12}}\phi_{12}(\pi - |\phi_{12}|) \tag{25}$$

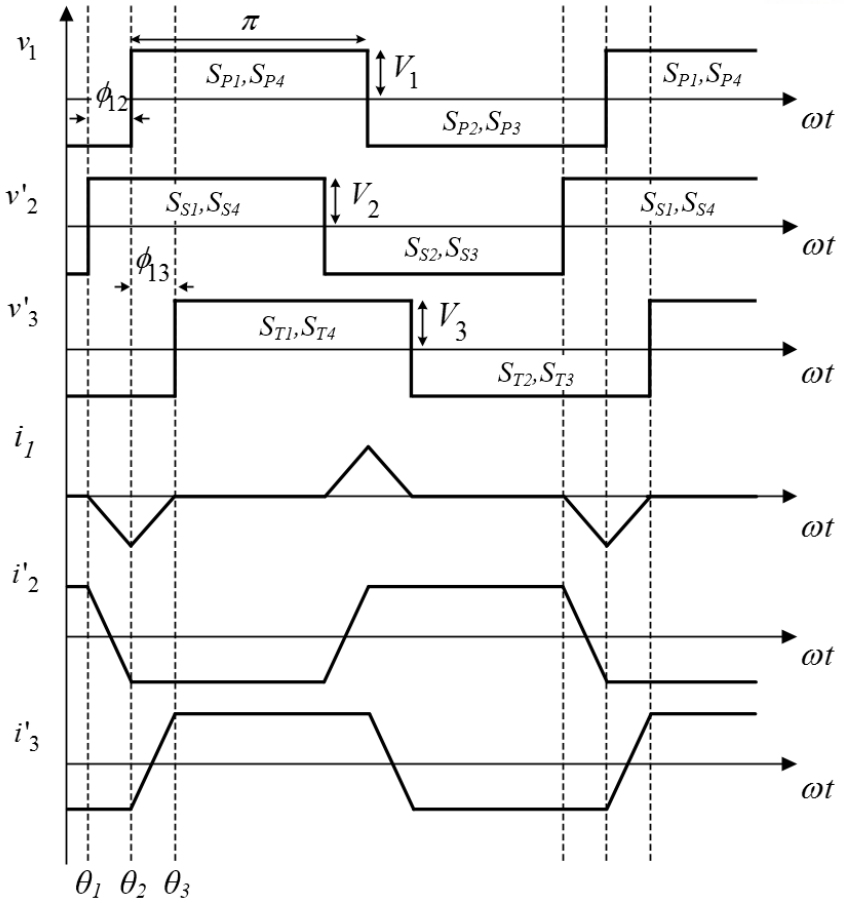

Fig. 3.4 Operating waveforms of Two-inductor three-port DAB converter with Port 1 remains at zero power ($\phi_{12} = -\phi_{13}$)

$$P_{13} = \frac{V_1 V_3}{2\pi^2 f_{sw} L_{13}} \phi_{13}(\pi - |\phi_{13}|) \tag{26}$$

$$P_{23} = \frac{V_2 V_3}{2\pi^2 f_{sw} L_{23}} (\phi_{13} - \phi_{12})(\pi - |\phi_{13} - \phi_{12}|) \cong 0 \tag{27}$$

where, ϕ_{12} and ϕ_{13} ranges are limited from -π/2 to π/2. The power equations (25)-(27) can be simplified as each port power equation as follows:

$$P_1 = P_{12} + P_{13}, \quad P_2 = -P_{12}, \quad P_3 = -P_{13} \tag{28}$$

The equation (28) shows that the two ports, Port 2 and Port 3 are equivalently seen as connected to Port 1 in parallel.

The proposed converter can transfer power from Port 2 to Port 3 and vice versa even without the direct power transfer path between them. Fig. 3.4 shows the operating waveforms of the proposed converter with Port 1 remaining at zero power. Although the direct power transfer path is eliminated,

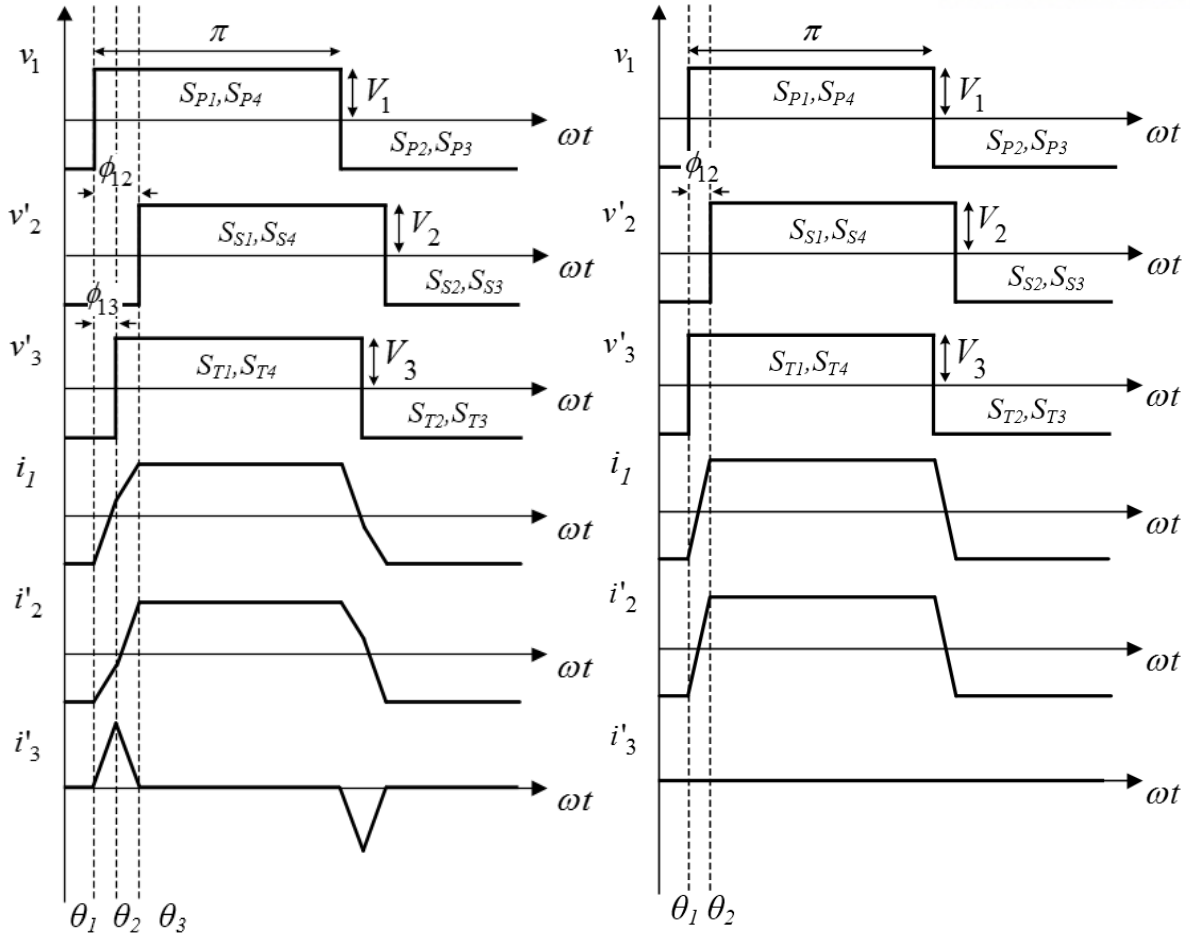

Fig. 3.5 Operating waveforms with Port 3 idling in (a): the conventional three-port DAB converter (b): Two-inductor three-port DAB converter

power can be still transferred between the two ports by detouring around Port 1. Circulating current occurs in Port 1 in this case. As illustrated in Fig. 3.4, the current, i_1 in Port 1 is sum of the currents i_2 and i_3 from Port 2 and Port 3. It means that a large portion of the current in Port 1 is cancelled out. This circulating current has only peak-value current, which may cause large core loss, but Port 1 does not have a power inductor or leakage inductance of the transformer. Therefore, bidirectional power flow capability among the three ports is sustained in the proposed converter without a considerable influence on the converter performance.

An energy storage element such as a battery, a supercapacitor and ESS can be integrated in three-port DC-DC converters [12], [19]-[21]. An energy storage element is used to capture energy at one time for use at a later time. Considering the operation of the energy storage element, the idling operation for the energy storage element often occurs. However, even if all the power switch devices in one port are turned off, power could flow through their body diodes. Therefore, zero power has to be achieved by

adjusting the phase shift values ϕ_{12} and ϕ_{13}.

Fig. 3.5 shows that theoretical idling operating waveforms for Port 3 of the conventional three-port DAB converter and Two-inductor three-port DAB converter when the converter parameters are ideal (i.e., zero loss and unit voltage gain). Due to the structure of the conventional three-port DAB converter, the Port 3 power is determined with both of the phase displacement values ϕ_{12} and ϕ_{13}.

$$P_{13} = -P_{23} \tag{29}$$

The equation (29) above has to be satisfied in order to make the net active power zero in Port 3 with proper values of ϕ_{12} and ϕ_{13}. Although, the total net active power can be zero in Port 3, it has circulating current, i'_3 as illustrated in Fig. 3.5 (a) even in the ideal case. As a result, it lowers the total power conversion efficiency.

Fig. 3.5 (b) shows that the idling operating waveforms for Port 3 of the proposed converter. Port 3 power is only determined by ϕ_{13}. According to the equations (26) and (28), zero active power can be achieved with the Port 3 voltage phase in phase with respect to the reference voltage. it has reduced circulating current. The circulating current occurs by the voltage difference between Port 1 and Port 3, which can be zero in the ideal case as shown in Fig. 3.5 (b). Therefore, Two-inductor three-port DAB converter has less circulating current than that of the conventional three-port DAB converter, which may increase the total power conversion efficiency.

Two-inductor three-port DAB converter can have simpler control strategies since it is a decoupled system itself with its structure. It can effectively eliminate the port coupling issue that the conventional three-port DAB converter has. The equations (14), (15), (17) and (18) are the linearized system matrix elements of the conventional three-port DAB converter. These can be also applied on Two-inductor three-port DAB converter in the same manner. In the proposed converter, the inductance in Port 1 is assumed to be zero since it has neglectable leakage inductance of the transformer. The equations (14), (15), (17) and (18) considering zero L_1 can become as follows:

$$G_{11} = \frac{V_1 L_3 \cos(\phi_{12op})}{(1/4)\pi^3 f_{sw} L_2} \tag{30}$$

$$G_{12} \cong 0 \tag{31}$$

$$G_{21} \cong 0 \tag{32}$$

$$G_{22} = \frac{V_1 L_2 \cos(\phi_{13op})}{(1/4)\pi^3 f_{sw} L_3} \tag{33}$$

The off-diagonal elements causing the power correlation, G_{12} and G_{21} become zero in Two-inductor

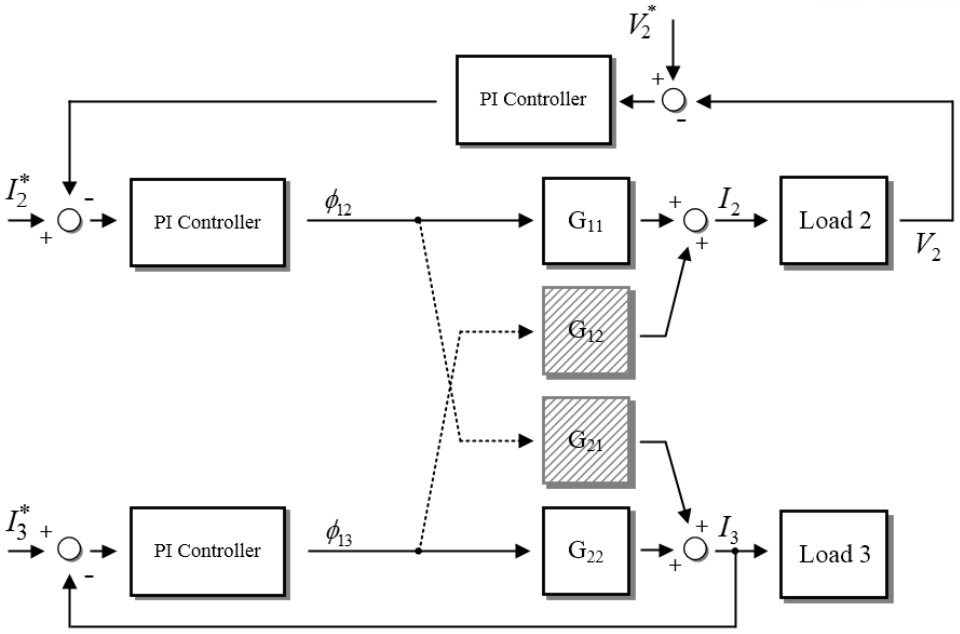

Fig. 3.6 Control diagram of Two-inductor three-port DAB converter

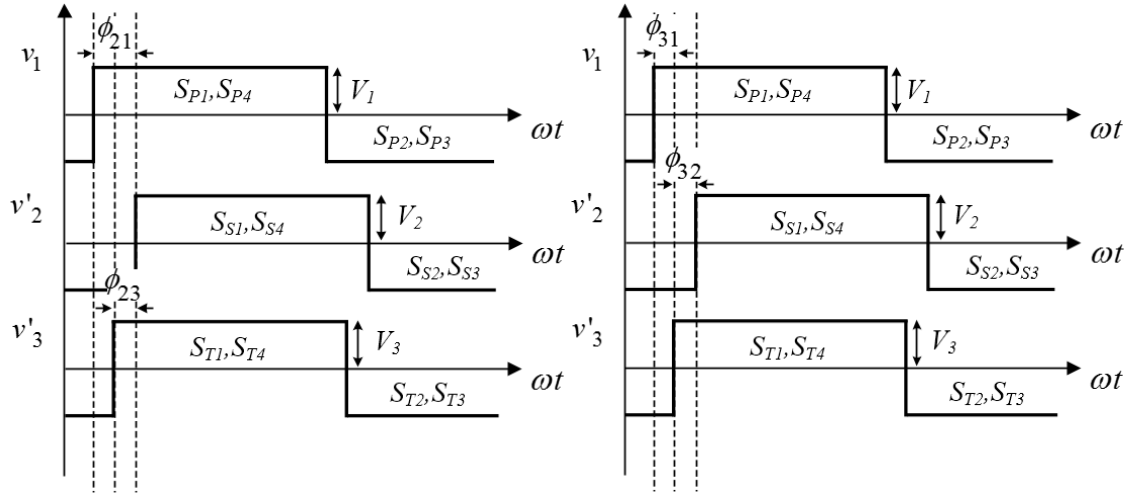

(a) (b)

Fig. 3.7 Different voltage phase reference in Two-inductor three-port DAB converter (a): Port 2 voltage phase reference (b): Port 3 voltage phase reference

three-port DAB converter. Therefore, the system matrix can be expressed as below:

$$\begin{bmatrix} I_2 \\ I_3 \end{bmatrix} = \begin{bmatrix} G_{11} & 0 \\ 0 & G_{22} \end{bmatrix} \begin{bmatrix} \phi_{12} \\ \phi_{13} \end{bmatrix} = G\vec{\phi} \tag{34}$$

The equations (34) denotes the system matrix of the proposed converter. the system matrix shows that

each load port can be controlled by its corresponding control variables ϕ_{12} and ϕ_{13}. Therefore, control strategies for the proposed converter can be simple.

Fig. 3.6 illustrates the control diagram of the proposed converter. As it shows, the system itself is a decoupled system without the coupling elements G_{12} and G_{21}, which does not require the decoupling control using a look-up table. One control stage can be reduced in the proposed converter compared with the conventional three-port DAB converter. Consequently, Two-inductor three-port DAB converter can independently control each port without additional decoupling control strategies.

The decoupled system can be only realized when the phase reference voltage is the square-wave voltage in the port that does not have series inductance. If the phase reference voltage is either of the voltages of the ports that have series inductance as shown in Fig 3.7, one of the off-diagonal elements appears as below:

$$\begin{bmatrix} I_2 \\ I_3 \end{bmatrix} = \begin{bmatrix} G_{11} & 0 \\ G_{21} & G_{22} \end{bmatrix} \begin{bmatrix} \phi_{21} \\ \phi_{31} \end{bmatrix} = G\vec{\phi} \tag{35}$$

$$\begin{bmatrix} I_2 \\ I_3 \end{bmatrix} = \begin{bmatrix} G_{11} & G_{12} \\ 0 & G_{22} \end{bmatrix} \begin{bmatrix} \phi_{32} \\ \phi_{31} \end{bmatrix} = G\vec{\phi} \tag{36}$$

The equation (35) corresponds to Fig. 3.7 (a), where the voltage phase reference is v'_2 and the equation (36) corresponds to Fig. 3.7 (b), where the voltage phase reference is v'_3. This denotes that setting a reference voltage phase as the voltage of the port that includes series inductance makes a coupling element in the system matrix. Therefore, the voltage phase reference must be the voltage phase of the port does not have series inductance.

3.1.3 Simulation and Experimental Results

In order to demonstrate that the proposed converter can interconnect various loads, Port 1, Port 2 and Port 3 are set as a DC grid, a DC load and ESS, respectively. The effectiveness of the proposed converter is verified with PSIM and a 5-kW prototype converter. A 5-kW prototype converter shown in Fig. 3.8 is used to obtain experimental results. The converter parameters and specifications are listed in Table II. In the experimental results, a three-winding transformer is designed using TC-704025, the nanocrystalline core by Avertec. Ch571125, the high flux cores by Changsung corporation are used as power transfer inductors. IPW65R041, the power MOSFETs manufactured by Infineon are installed for Port 1 and Port 2 which have relatively high voltages. IRF250P224, the high current power MOSFETs manufactured by Infineon are used for Port 3. The control strategy is implemented by a TMS320F28335 digital signal processor (DSP) by Texas Instruments.

TABLE II SYSTEM SPECIFICATIONS AND PARAMETERS FOR TWO-INDUCTOR THREE-PORT DAB CONVERTER

Parameter	Symbol	Value
Rated power	-	5 kW
Port 1 voltage (DC bus)	V_1	380 V
Port 2 voltage (DC load)	V'_2	380 V
Port 3 voltage (ESS)	V'_3	60 V
Power inductor	L'_2	140 μH
	L'_3	5.1 μH
Turns ratio	n_{12} (n_1/n_2)	1
	n_{13} (n_1/n_3)	6
Switching frequency	f_{sw}	25 kHz

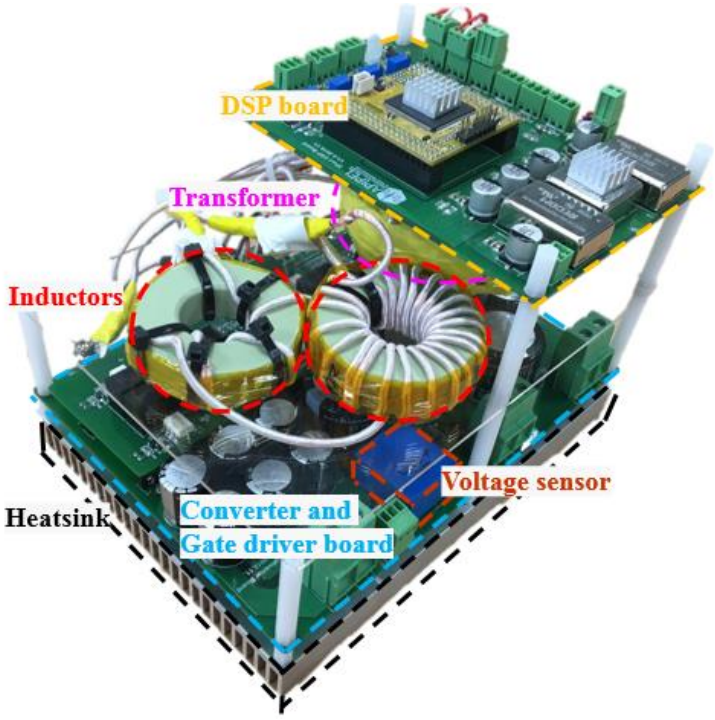

Fig. 3.8 5-kW prototype of Two-inductor three-port DAB converter

Fig. 3.9 shows the steady-state operational simulation results in PSIM. In Fig. 3.9 (a), Port 2 and Port 3 consume 3-kW and 1-kW from Port 1, respectively with the phase delay values $\phi_{12} = 0.890$ and $\phi_{13} = 0.227$, which denotes power transfer occurs by their port voltage phase difference. Fig. 3.9 (b) depicts that Port 3 transfers 1-kW to Port 2 via Port 1 and Port 1 provides 2-kW to Port 2. It shows that power can be transferred between Port 2 and Port 3 in spite of absence of the power path between them.

Fig. 3.10 shows circulating current comparison in Port 3 idling for the conventional three-port DAB converter and Two-inductor three-port DAB converter. Fig. 3.10 (a) is the result of the conventional

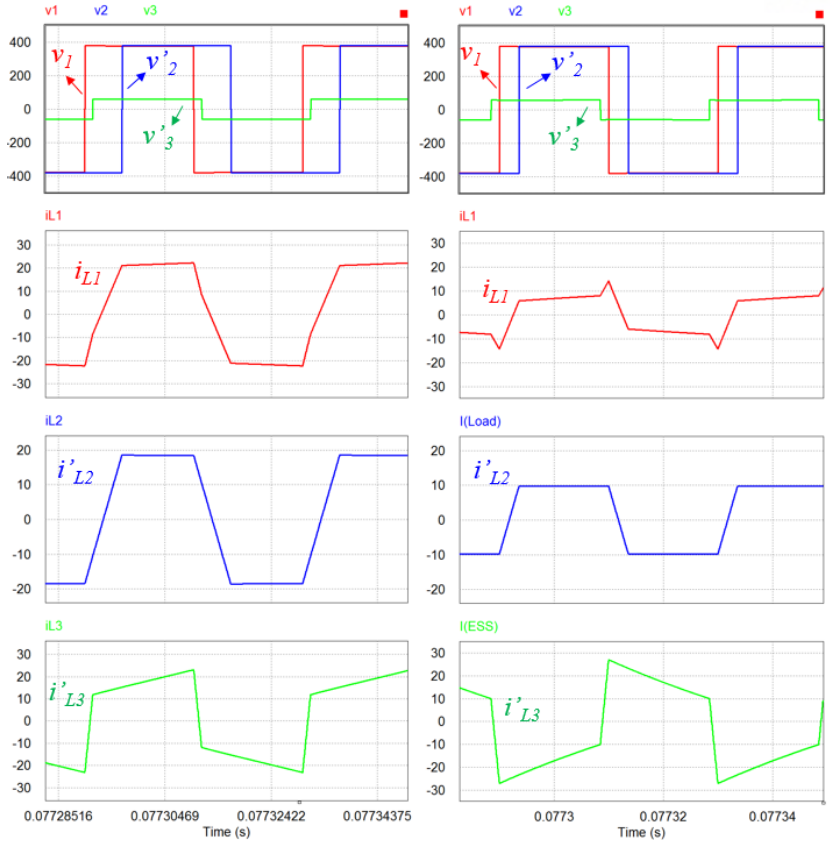

(a) (b)

Fig. 3.9 Steady-state operational simulation results at operating points: (a): $\phi_{12} = 0.890$, $\phi_{13} = 0.227$ (b): $\phi_{12} = 0.558$, $\phi_{13} = 0.244$

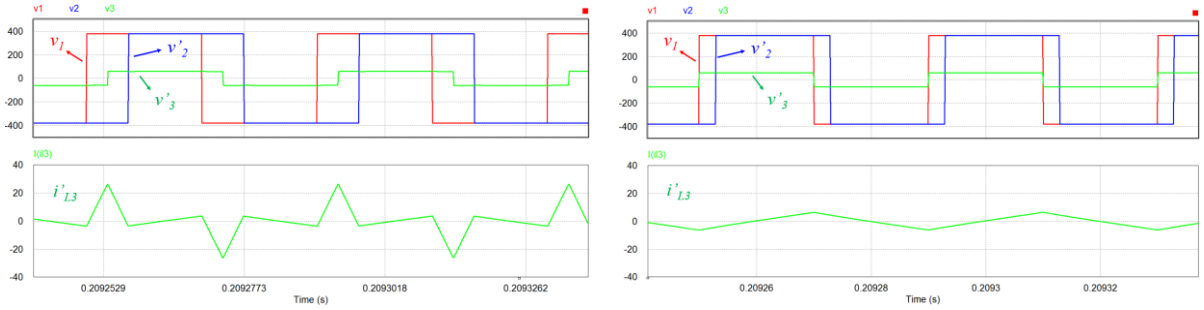

(a) (b)

Fig. 3.10 Simulation result of circulating current in Port 3 left at zero power in (a): the conventional three-port DAB converter (b) Two-inductor three-port DAB converter

converter. Since the three-ports are all coupled, Port 3 can be left at zero power when the equation (29) is satisfied, which generates relatively high circulating current having 6 A of RMS value and 25 A of peak value. Fig. 3.10 (b) shows that circulating current in Port 3 remaining at zero power. Port 3 can remain at zero power, which its port voltage is in phase with the reference phase. It generates reduced circulating current having 2.5 A of RMS value and 6 A of Peak value by their port voltage difference

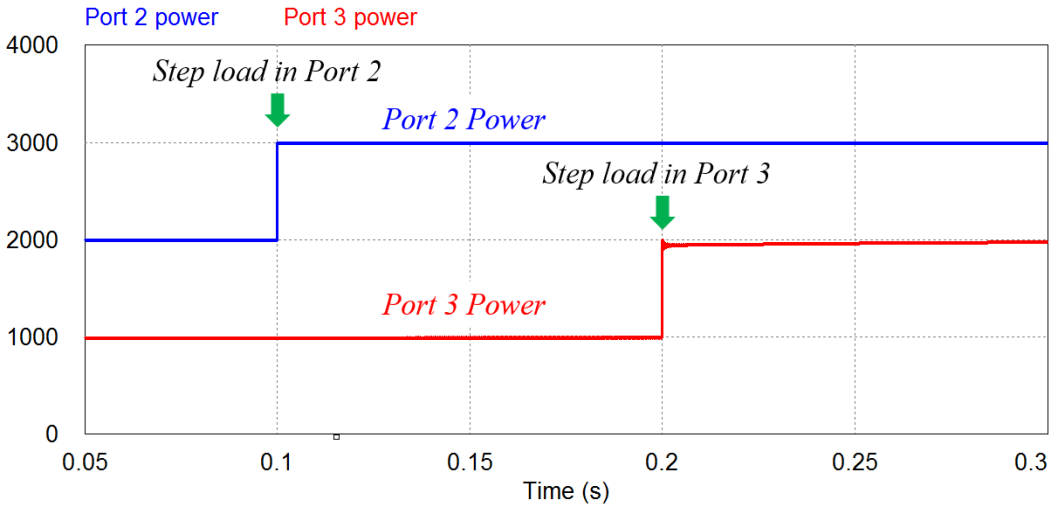

Fig. 3.11 Simulation result of port power change at step-load change

between Port 1 and Port 3.

Fig. 3.11 illustrates changes of each power at step-load conditions. Port 2 power changes from 2-kW to 3-kW at 0.1 sec and Port 3 power varies from 1-kW to 2-kW at 0.2 sec. It shows that power change in one port does not influence the other port control. Therefore, the result shows that Two-inductor three-port DAB converter is a power decoupled system.

Fig. 3.12 depicts the steady-state experimental results using the 5-kW prototype converter shown in Fig. 3.8. Fig. 3.12 (a) shows the steady-state result at the full load condition, where Port 2 takes 4.5-kW with 1.390 rad of the phase shift value, ϕ_{12} and 0.279 rad of the phase displacement value, ϕ_{13}. Fig. 3.12 (b) illustrates the experimental steady-state waveforms where Port 2 consumes 3-kW from Port 1 transferring 2-kW and Port 3 providing 1-kW, respectively. The negative value, -0.314 rad of the phase shift, ϕ_{13} of Port 3 can transfer power to Port 2 without a straight power path between them.

Fig. 3.13 depicts the experimental results of one port idling operation (e.g. Port 3). Fig. 3.13 (a) shows the operating waveforms of Port 3 left at zero power in the conventional three-port DAB converter. In the conventional converter, in order to idle Port 3, it has to satisfy the equation (29), which occurs relatively high circulating current (RMS value: 4.5 A, Peak value: 14.5 A) whereas, in the proposed converter, Port 3 has reduced circulating current (RMS value: 1.8 A, Peak value: 3 A). The circulating current can be nearly zero when the voltage difference between Port 1 and Port 3 is zero, which typically is designed as zero voltage difference between ports [18].

Fig. 3.14 shows the experimental result of step-load response in Port 2. Port 2 has 3-kW of step-load where it changes from 3-kW to 4-kW while Port 3 remains at 1-kW. Port 2 voltage is adjusted to its reference voltage, 380 V with 300 ms settling time. Port 3 voltage and current are not influenced by a step-load of Port 2, which means the two ports are independently controlled by its structure.

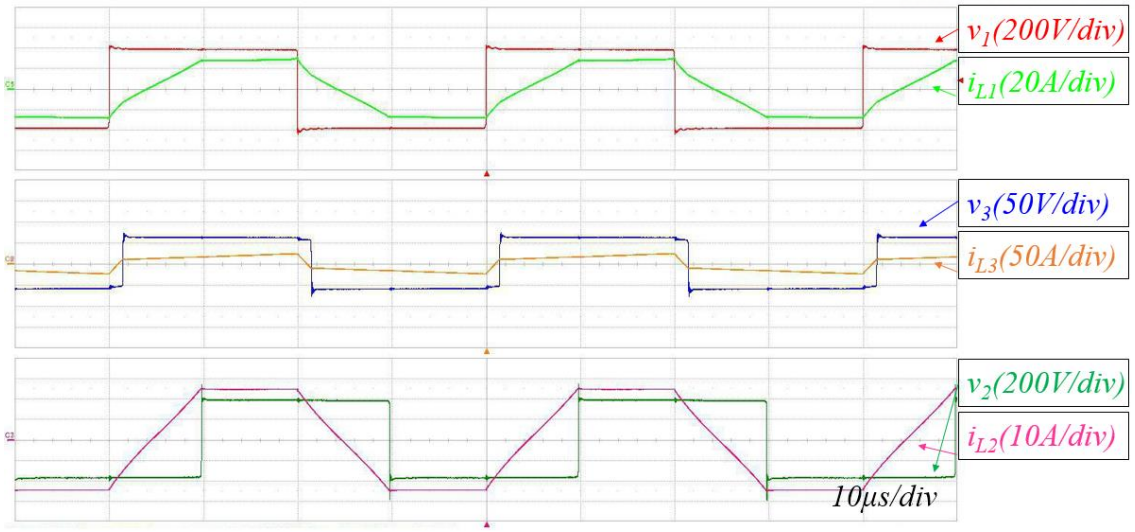

(a)

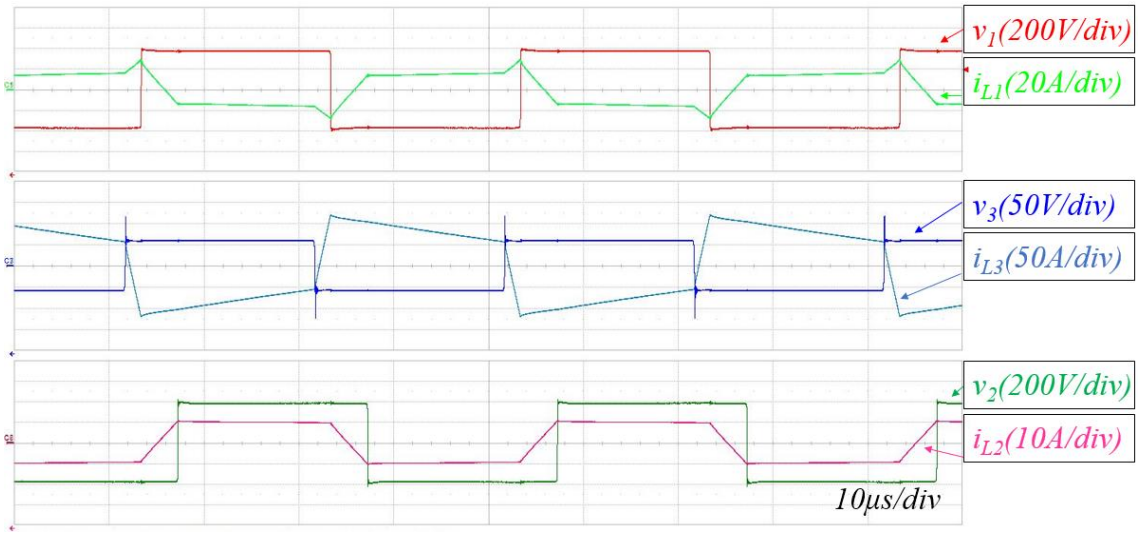

(b)

Fig. 3.12 Steady-state operational experimental results (a): Port 2 consuming 4.5-kW and Port 3 storing 500 W (b) Port 2 consuming 3-kW from Port 1 transferring 2-kW and Port 3 providing 1-kW

Fig 3.15 illustrates the efficiency curves of the proposed converter and the conventional converter. The highest efficiency of the proposed converter is 94.5 %, which is 1.9 % higher than that of the conventional converter. The proposed converter has approximately 1.5 % higher power conversion efficiency over the whole load range. It is because the proposed converter has one less power inductor, which means it has less core and conduction loss.

Two inductor three-port DAB converter using only two power inductors is proposed. The converter structure and operational principles are explained. The advantages of the proposed converter, which are simple control and reduced circulating current in one port idling are theoretically analyzed. In the simulation and experimental results, the proposed converter can transfer power by their phase shift

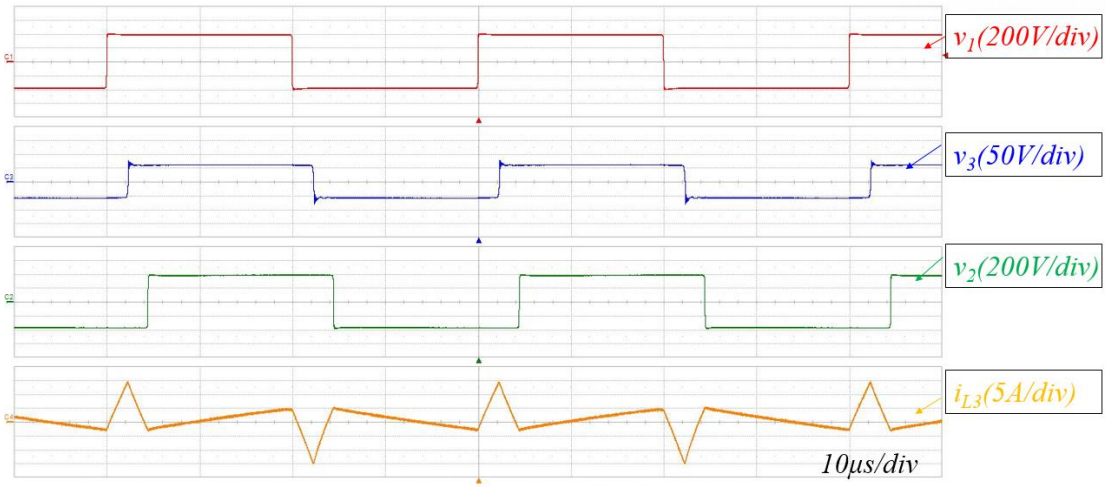

(a)

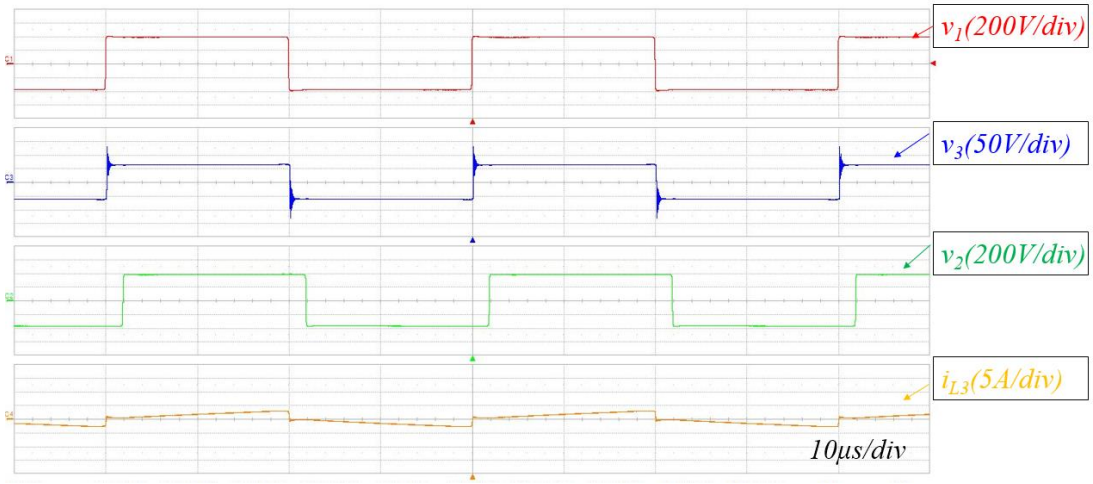

(b)

Fig. 3.13 Experimental results of circulating current in Port 3 idling in (a): the conventional three-port DAB converter (b): Two-inductor three-port DAB converter

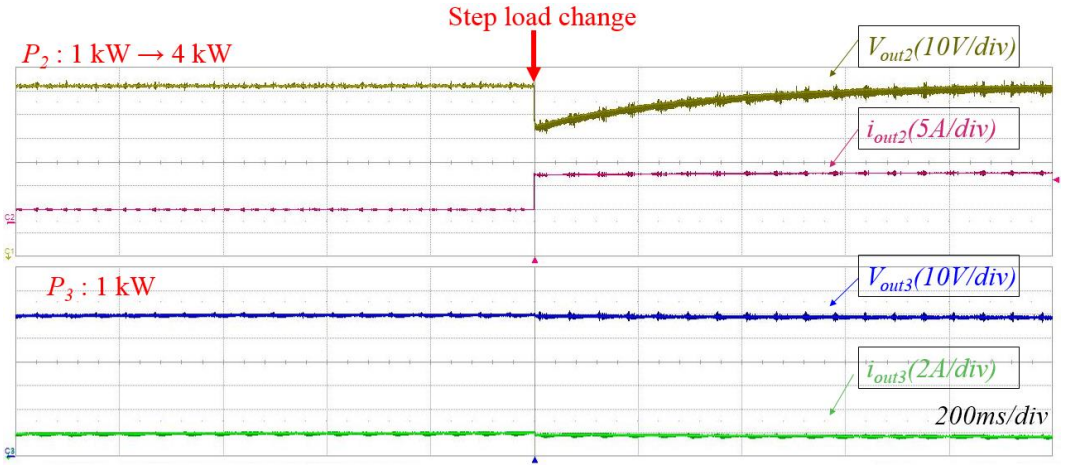

Fig. 3.14 Step-load response in Port 2 changing from 1-kW to 4-kW while Port 3 remains at 1-kW

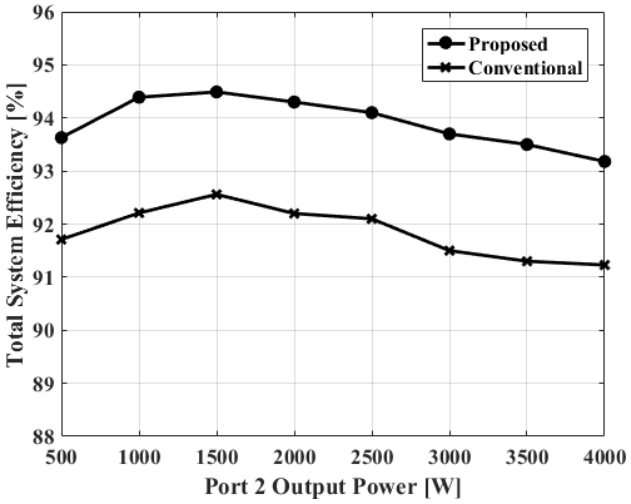

Fig. 3.15 Efficiency curves over change of Port 2 power with Port 3 fixed at 1-kW

values ϕ_{12} and ϕ_{13} in every direction regardless of the absence of a power transfer path between the ports having an inductor. The circulating current in Port 3 idling of the proposed converter compared with that of the conventional converter is reduced by 60 % and 79.4 % in terms of RMS value and peak value, respectively. The step-load response shows that Port 3 voltage and current do not get affected by Port 2 power step-change, from 1-kW to 4-kW, which means it is decoupled without additional control. The highest power conversion efficiency in the proposed converter is 94.5 %. The proposed converter has averagely 1.5 % higher efficiency than that of the conventional converter, which comes from less core and conduction loss due to one less power inductor. As a result, Two-inductor three-port DAB converter can be used to replace the conventional three-port DAB converter with higher power density, simple control and higher power efficiency.

3.2 Dual-transformer Three-port DAB Converter

Dual-transformer three-port DAB converter that has simple control without complex decoupling control is proposed in this chapter. It uses multiple transformers, not a single transformer. It has an advantage in terms of extendibility to connect more input and output ports than three. In addition, the transformer magnetizing inductance design methodology to achieve full zero voltage switching (ZVS) range is proposed and analyzed. The validity of the proposed converter is experimentally demonstrated with a 3-kW prototype.

3.2.1 Proposed Structure

Fig. 3.16 illustrates the Dual-transformer three-port DAB converter structure. It consists of three full bridges, which can be replaced with half bridges, two series inductances, which can be utilized with either external inductors or the transformer leakage inductances, and two high-frequency transformers. Each transformer corresponds to a load port (e.g. Port 2, Port 3) with the source port (e.g. Port 1). The structure is fundamentally the same equivalent circuit as Two-inductor three-port DAB converter, which means it has all the advantages that Two-inductor three-port DAB converter has, such as a decoupled system without using decoupling control strategies presented in [13], [16].

This configuration using two high-frequency transformers may bring lower power density than the Two-inductor three-port DAB structure. However, it has distinct advantages. It is a perfectly decoupled

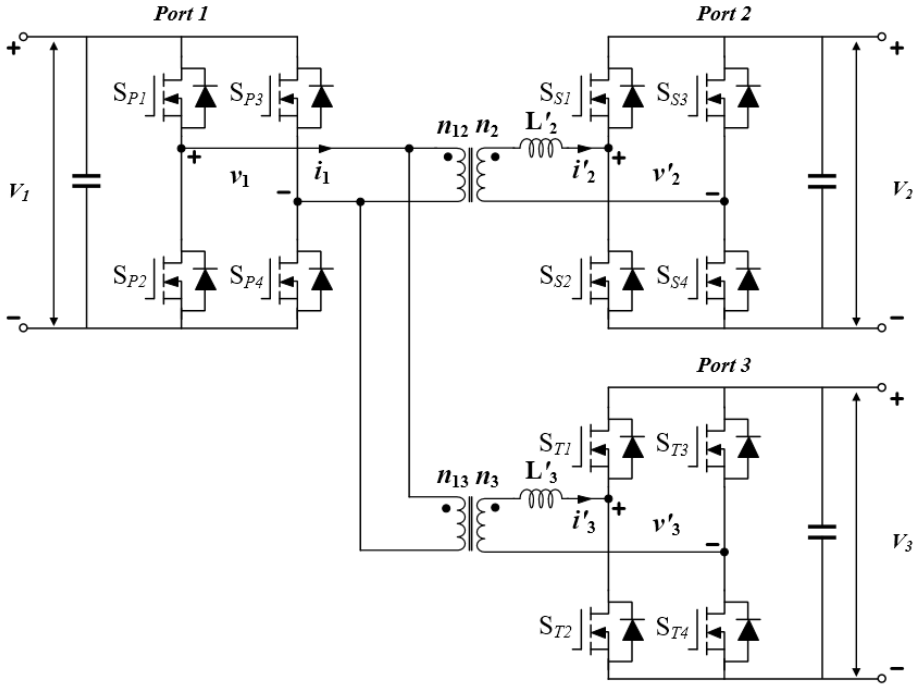

Fig. 3.16 Dual-transformer three-port DAB converter

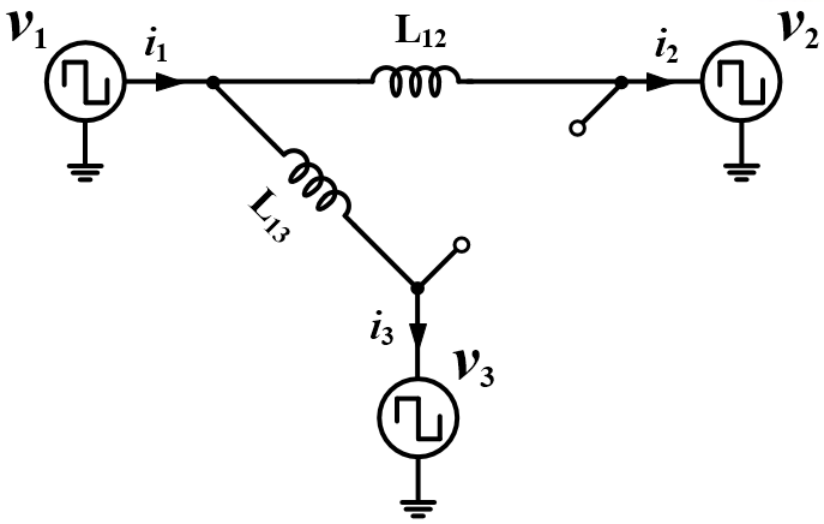

Fig. 3.17 Simplified equivalent circuit of Dual-transformer three-port DAB converter

system regardless of leakage inductance in Port 1 while Two-inductor three-port DAB converter requires small leakage inductance that is ignorable enough in Port 1. Also, it can fully use the transformer magnetizing inductances utilized to compensate current for the ZVS operation. The magnetizing inductance design methodology to expand the ZVS range is proposed and analyzed in the following sections.

3.2.1 Theoretical analysis

As previously stated, the operation of the diagonal opposite switch pairs S_{x1}, S_{x4} and S_{x2}, S_{x3} (x = P, S and T) complementarily switching with 50 % duty ratio at a fixed switching frequency can be described as two-level AC square-wave voltage sources with the magnitude of the corresponding DC source voltage. Port 2 and Port 3 are connected using two different transformers to Port 1, which all the ports can be referred to Port 1.

Fig. 3.17 depicts the simplified equivalent circuit of the proposed converter referred to the primary side with their turns ratio n_{22} (n_{12}/n_2) and n_{33} (n_{13}/n_3). The voltage sources v_1, v_2 ($=n_{22}v'_2$) and v_3 ($=n_{33}v'_3$) represent the primary side referred two-level AC square-wave voltage sources. The inductance L_{12} ($=n^2_{22}L'_2$) and L_{13} ($=n^2_{33}L'_3$) represent the primary referred effective inductances, which are the power transfer elements. Effective inductance does not exist between Port 2 and Port 3 since the two ports are not magnetically coupled with one transformer. In contrast, in Two-inductor three-port DAB converter, it can only be assumed to have infinite effective inductance when L_1 is much greater than L_2 and L_3.

Due to infinite impedance between Port 2 and Port 3, the power transfer equations of the proposed converter can be derived as follows:

$$P_{12} = \frac{V_1 V_2}{2\pi^2 f_{sw} L_{12}} \phi_{12}(\pi - |\phi_{12}|) \tag{37}$$

$$P_{13} = \frac{V_1 V_3}{2\pi^2 f_{sw} L_{13}} \phi_{13}(\pi - |\phi_{13}|) \tag{38}$$

$$P_1 = P_{12} + P_{13}, \quad P_2 = -P_{12}, \quad P_3 = -P_{13} \tag{39}$$

These derived equations mean that Dual-transformer three-port DAB converter operates exactly the same as Two-inductor three-port DAB converter that has neglectable leakage inductance in Port 1. Therefore, the operating waveforms can be illustrated as same as shown in Fig. 3.3. Also, the equations (37), (38) can be linearized as system matrix elements presented same as the equations (30)-(33). However, the off-diagonal terms are absolutely zero as below because Dual-transformer three-port DAB converter uses two different transformers.

$$G_{12} = 0 \tag{40}$$

$$G_{21} = 0 \tag{41}$$

Therefore, Dual-transformer three-port DAB converter is an absolute decoupled system regardless of the inductance L_1 value. In addition, it has less circulating current in one of the load ports (e.g. Port 2 or Port 3) idling as it has the same operational principles.

3.2.2 Zero Voltage Switching (ZVS) Capability Extension

Dual-transformer three-port DAB converter is simplified to the two load ports connected to Port 1 illustrated in Fig. 3.16. If one of the load ports (e.g. Port 3) is open, the system can be seen as the two-port DAB converter. For sake of simplicity to analyze the ZVS capability of DAB-based converters, the ZVS operation principles have to be explained before all.

Fig 3.18 shows that the operating waveforms of the proposed converter with Port 3 open, which operates as the two-port DAB converter. To simplify the process of the operation, only steady states are considered. According to the operating waveforms, the switching cycles can be divided as depicted in Fig. 3.19.

The interval 1 ($\omega t \leq \theta_1$) shown in Fig. 3.19 (a) depicts that the inductor current (i_1 and i'_2) flows in the negative direction before the switch S_{P1} and S_{P4} turn on. At the angle of θ_1, the switch pair S_{P2} and S_{P3} turn off.

The interval 2 ($\theta_1 < \omega t \leq \theta'_1$) illustrated in Fig. 3.19 (b) shows the dead time section before the switches S_{P1} and S_{P4} turn on. The inductor current starts conducting through the anti-parallel diodes of

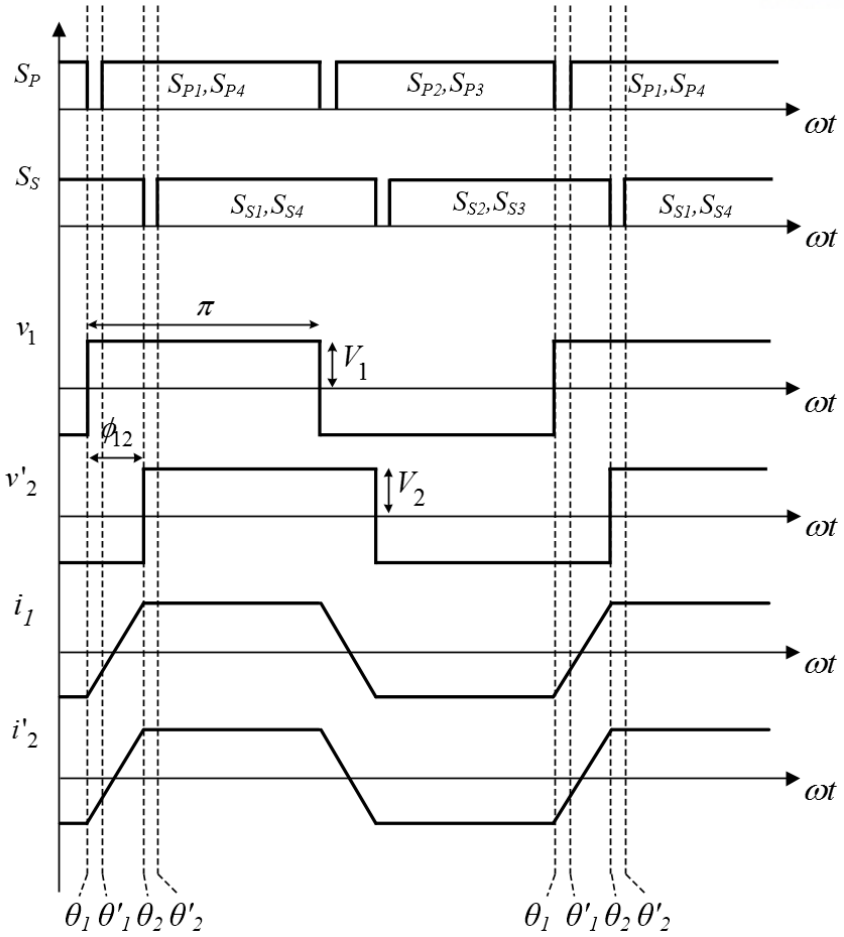

Fig. 3.18 Steady-state waveforms between Port 1 and Port 2 with Port 3 open

the switches. Also, a small amount of current discharges the output capacitances of S_{P1} and S_{P4} and charges

The interval 2 ($\theta_1 < \omega t \leq \theta'_1$) illustrated in Fig. 3.19 (b) shows the dead time section before the switches S_{P1} and S_{P4} turn on. The inductor current starts conducting through the anti-parallel diodes of the switches. Also, a small amount of current discharges the output capacitances of S_{P1} and S_{P4} and charges the diagonal opposite output capacitances of S_{P2} and S_{P3} to V_1. In this interval, the conduction through the switches S_{P1} and S_{P4} in the negative direction makes zero voltage across the switches before they turn on. Therefore, the ZVS is achieved on the switches S_{P1} and S_{P4}.

The interval 3 ($\theta'_1 < \omega t \leq \theta_2$) depicted in Fig. 3.19 (c) and Fig. 3.19 (d) shows that the inductor current starts conducting through the switches S_{P1} and S_{P4}. The inductor begins changing the inductor current direction due to the positive voltage applied on the inductor shown in Fig. 3.19 (d). At the angle of θ_2, the switches S_{S2} and S_{S3} in Port 2 turn off while the inductor current flows in the positive direction.

The interval 4 ($\theta_2 < \omega t \leq \theta'_2$) shown in Fig. 3.19 (e) depicts the dead time interval before the switches S_{S1} and S_{S4} turn on. The inductor current conducts through the anti-parallel diodes of S_{S1} and S_{S4}. Besides, it discharges the output capacitances of S_{S1} and S_{S4} and charge the output capacitances of S_{S2} and S_{S3}.

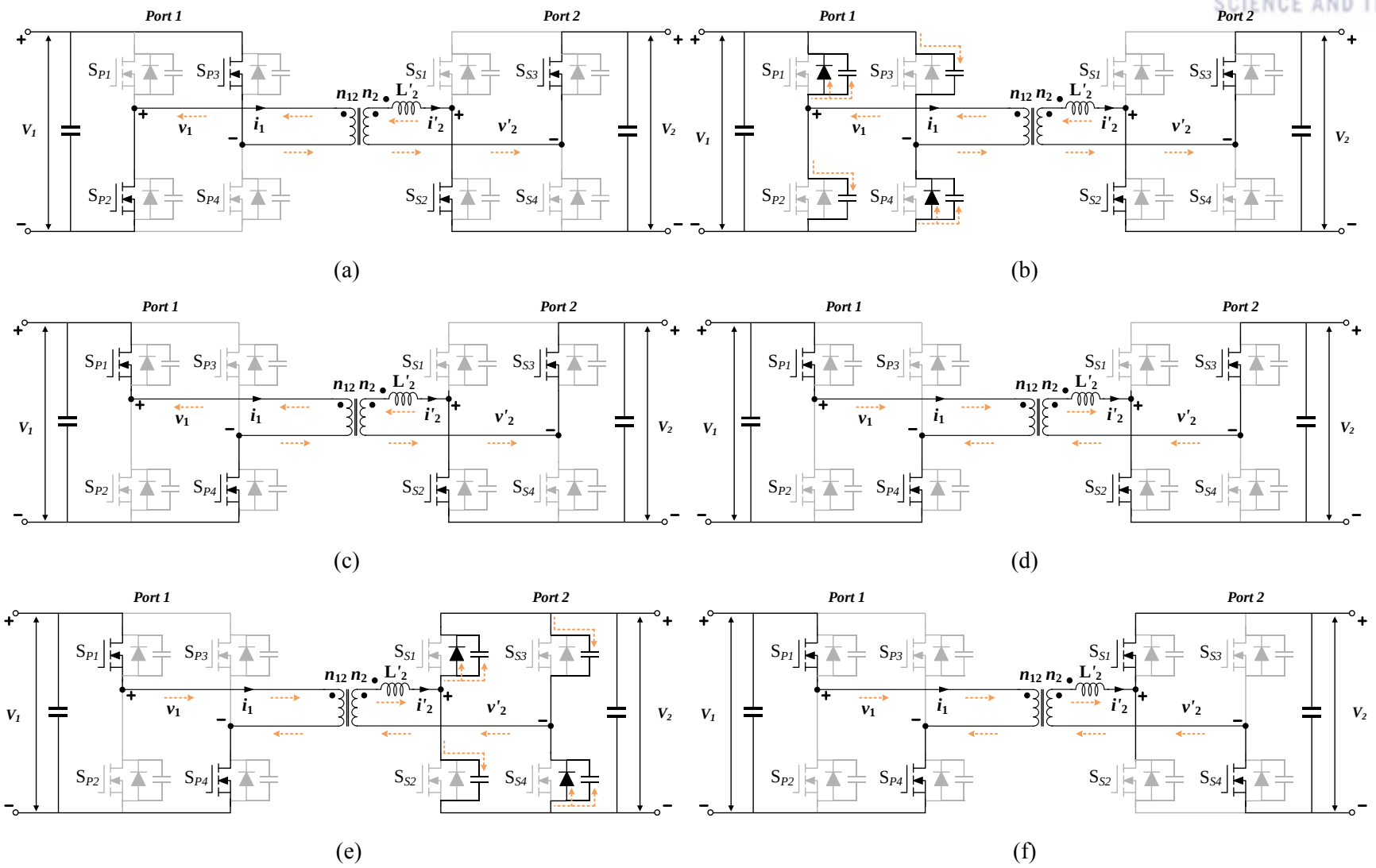

Fig. 3.19 Operating process of Dual-transformer three-port DAB converter with Port 3 open

The positive-flowing inductor current realizes the ZVS on the switches S_{S1} and S_{S4}.

The interval 5 ($\theta'_2 < \omega t$) shown in Fig. 3.19 (f) illustrates the inductor current conducts through the switches S_{S1} and S_{S4}. As the structure of the converter is symmetric, the rest of the process is the same as above.

To achieve the ZVS earlier-explained, the inductor current must be negative at θ_1 for Port 1 and positive at θ_2 for Port 2. The inductor currents for the ZVS conditions can be derived as follows:

$$i_{L12}(\theta_1) = \frac{1}{4 f_{sw} L_{12}}[(1-2d_{12})n_{22}V_2 - V_1] \le 0 \tag{42}$$

$$i_{L12}(\theta_2) = \frac{1}{4 f_{sw} L_{12}}[(2d_{12}-1)V_1 - n_{22}V_2] \ge 0 \tag{43}$$

where, d_{12} ($=\phi_{12}/\pi$) is the phase shift ratio. The ZVS boundary can be obtained with respect to output power over the voltage gain M12 defined as $n_{22}V_2/V_1$.

$$M_{12} \le \frac{1}{(1-2d_{12})} \tag{44}$$

$$M_{12} \ge (1-2d_{12}) \tag{45}$$

The normalized ZVS boundary is obtained with respect to power over the voltage gain M_{12} as the equations above. The variation of output power P_{12} in per unit over the duty ratio d_{12} for different values of M_{12} can be as shown in Fig. 3.20. The output power curve has to be within the constraint bounded by the two ZVS boundaries in order to achieve the ZVS for both of the ports. Fig. 3.20 (a) shows that when the voltage gain M_{12} is unity, the output power curve is within the boundary for the whole load range. Fig. 3. 20 (b) shows that when the voltage gain M_{12} is greater than unity, which means the Port 2 voltage is higher than that of Port 1, the output power curve is out of the Port 1 ZVS boundary in light load conditions. Fig. 3.20 (c) depicts that when the voltage gain M_{12} is smaller than unity, the output power curve is out of the Port 2 ZVS boundary in light load conditions. As a result, the voltage gain should be designed as close as unity to achieve the ZVS. Otherwise the ZVS fails in one of the ports in light load conditions.

The ZVS failure can cause various issues such as high stress on switch devices by voltage spike, low efficiency by hard switching operation and increase of noise [22]-[24]. Due to these issues stated, several methods have been proposed to extend the ZVS capability of DAB converters. Zero vector control strategies to expand the ZVS capability have been presented in [25], [26]. Adding auxiliary circuit methods for the ZVS capability extension have been proposed in [27], [28]. Using magnetizing inductance of the transformer method has been proposed in [29].

A zero vector control strategy for the ZVS capability extension is proposed for the conventional three-

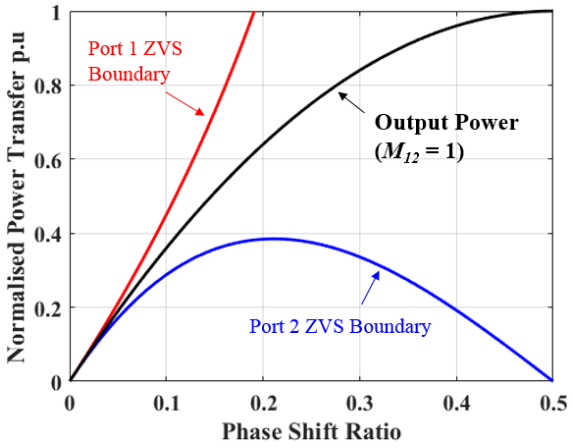

(a)

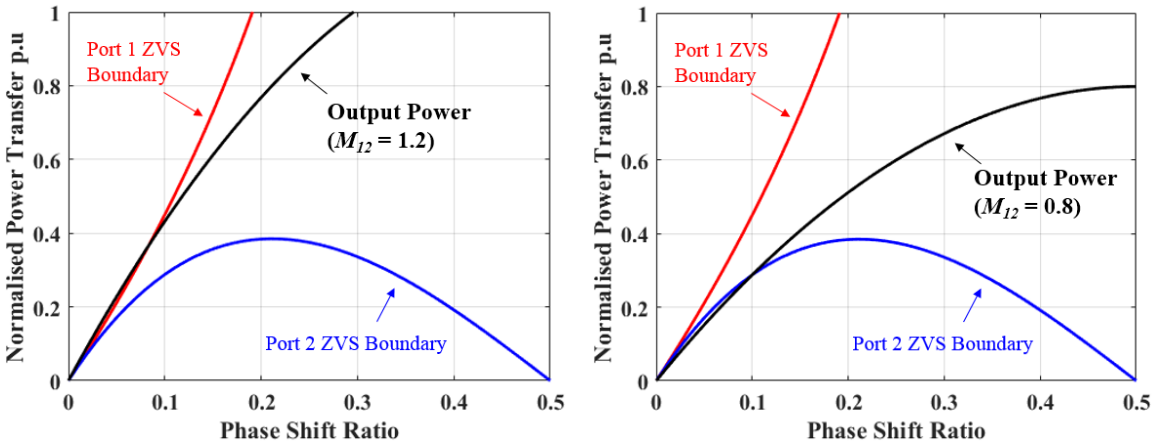

(b) (c)

Fig. 3.20 ZVS range according to voltage gain M: (a): M_{12}=1 (b): M_{12}=1.2 (c) M_{12}=0.8

port DAB converter in [13]. However, a zero vector control cannot be applied to both of Two-inductor three-port DAB converter and Dual-transformer three-port DAB converter. the additional control variable for the zero vector control can make cross-coupled loops to control, which eliminates the strong advantage of the decoupled structure. Adding auxiliary circuits to extend the ZVS capability may weaken the purpose of multi-port converters that have high power density and low production cost.

Magnetizing inductance that can extend the ZVS capability has not been considered in any of the three-port DAB converters due to the complex structure. Also, it cannot fully widen the ZVS range for Two-inductor three-port DAB converter because it may require to re-arrange the inductance placement, which may turn the converter into a different structure. However, in Dual-transformer three-port DAB converter, magnetizing inductance can be fully utilized to achieve the ZVS operation for a whole load range. The magnetizing design methodology for the full ZVS capability is proposed in the following section.

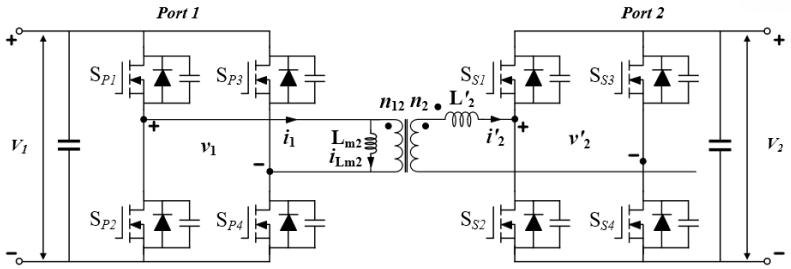

(a)

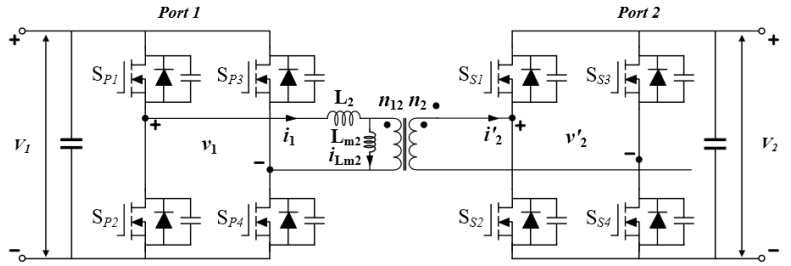

(b)

Fig. 3.21 Magnetizing inductance for different inductor placements (a): in Port 2 (b): in Port 1

3.2.3 Magnetizing Inductance Design

Fig. 3.21 shows Dual-transformer three-port DAB converter with Port 3 open for different inductor placements considering the magnetizing inductance of the transformer. Fig. 3.21 (a) illustrates that the power transfer inductor is placed in Port 2. The inductor current i_1 in Port 1 can become sum of the inductor current i'_2 in Port 2 and the magnetizing current i_{Lm2}. In the structure shown in Fig. 3.21 (b), the inductor current i'_2 is the current that is i_{Lm2} subtracted from the Port 1 inductor current i_1. Considering the addition of the magnetizing current i_{Lm2}, the inductor current can be re-derived at the angles of θ_1 and θ_2 as below for the different inductor placements.

$$i_{L12}(\theta_1) = \frac{1}{4 f_{sw} L_{12}}[(1-2d_{12})n_{22}V_2 - V_1] - \frac{V_1}{4 f_{sw} L_{m2}} \le 0 \tag{46}$$

$$i_{L12}(\theta_2) = \frac{1}{4 f_{sw} L_{12}}[(2d_{12}-1)V_1 + n_{22}V_2] \ge 0 \tag{47}$$

$$i_{L12}(\theta_1) = \frac{1}{4 f_{sw} L_{12}}[(1-2d_{12})n_{22}V_2 - V_1] \le 0 \tag{48}$$

$$i_{L12}(\theta_2) = \frac{1}{4 f_{sw} L_{12}}[(2d_{12}-1)V_1 + n_{22}V_2] + \frac{n_{22}V_2}{4 f_{sw} L_{m2}} \ge 0 \tag{49}$$

The equations (46)-(47) are the inductor current at the angles of θ_1 and θ_2 when the inductor is in Port 2 and the equations (48)-(49) for when the inductor is in Port 1. The effect of the magnetizing current can widen one of the ZVS boundaries shown in the equations (46) and (49) for the two different

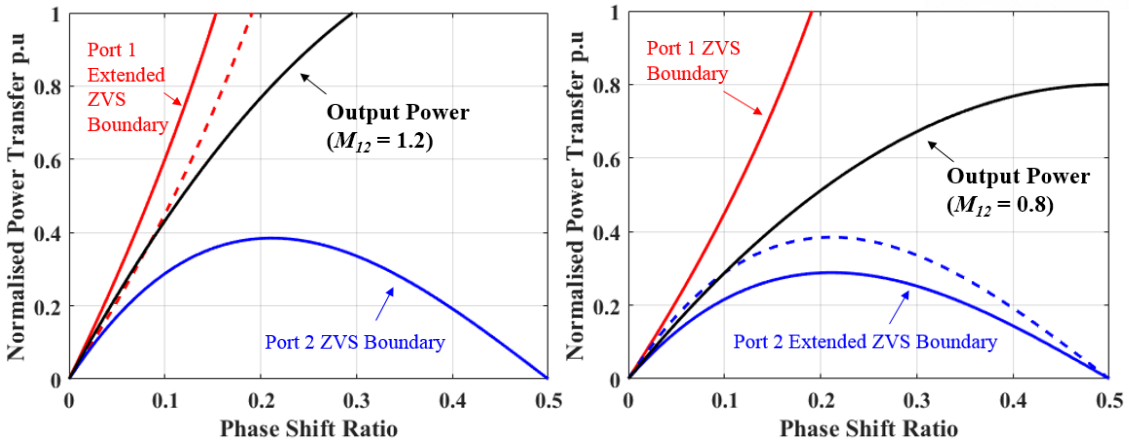

(a) (b)

Fig. 3.22 Extended ZVS range (a): in Port 1 (b): in Port 2 with the coefficient α=3

structures. By defining the coefficient α (= L_{m2}/L_{12}), the extended ZVS boundaries can be illustrated as shown in Fig. 3.22 at α = 3. Fig. 3.22 (a) depicts that the Port 1 ZVS boundary is extended due to the inductor located in Port 2. Fig. 3.22 (b) illustrates that the Port 2 ZVS boundary is widened because of the inductor placed in Port 1. Therefore, the inductor placement should be designed depending on the voltage gain.

The two voltage gains can be pre-determined as loads require constant voltages, but the different amount of power. To cover all the combinations of the two different voltage gains, the design methodology of the magnetizing inductance for the different cases that can be appeared in the converter is proposed.

Fig. 3.23 depicts four different cases depending on the voltage gains [M_{12} (=$n_{22}V_2/V_1$) and M_{13} (=$n_{33}V_3/V_1$)] to extend the ZVS capability in Dual transformer three-port DAB converter. Fig. 3.23 (a) shows Case 1 where the two inductors are placed in Port 1 and the magnetizing inductance current compensate the ZVS operation for Port 2 and Port 3. Fig. 3.23 (b) shows Case 2 where the inductor L_2 is located in Port 2 and L_3 is placed in Port 1. The magnetizing inductance current i_{Lm2} compensates the ZVS operation for Port 1 and the magnetizing inductance current i_{Lm3} compensates the ZVS operation for Port 3. Case 3 shown in Fig. 3.23 (c) is the exactly opposite structure as Case 2. Fig. 3.23 (d) illustrates Case 4 where the inductor L_2 is located in Port 2 and the inductor L_3 is put in Port 3. The magnetizing current can widen the ZVS boundary for Port 1 in this case.

As the same manner applied on the equations (46)-(49) for the relation between Port 1 and Port 2, the inductor current i_{L3} between Port 1 and Port 3 can be derived for the different inductor placements as follows:

$$i_{L13}(\theta_1) = \frac{1}{4 f_{sw} L_{13}}[(1-2d_{13})n_{33}V_3 - V_1] - \frac{V_1}{4 f_{sw} L_{m3}} \le 0 \quad (50)$$

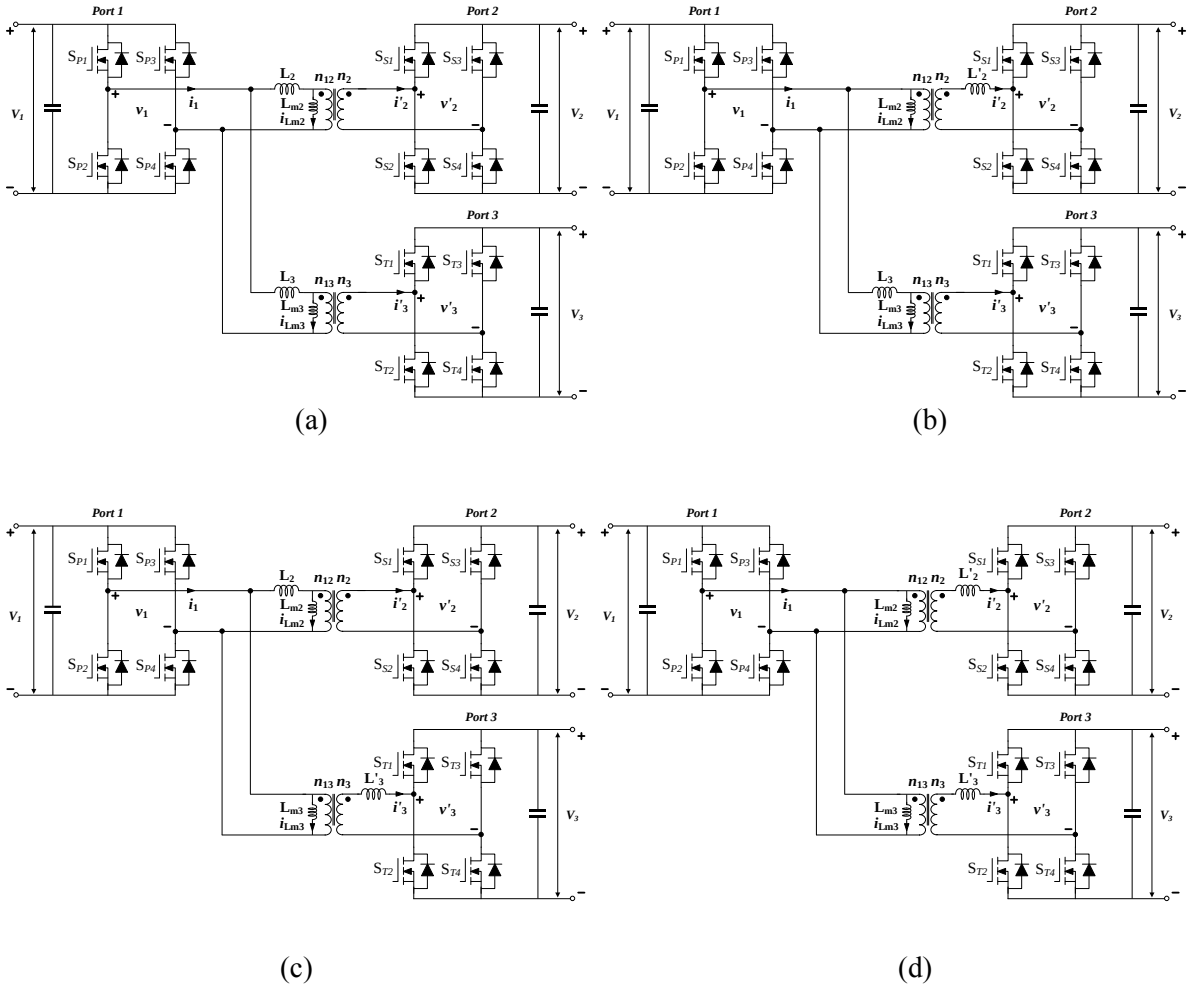

Fig. 3.23 Magnetizing inductance utilization for different cases (a): Case 1 (M_{12}<1 and M_{13}<1) (b): Case 2 (M_{12} >1 and M_{13} <1) (c): Case 3 (M_{12} <1 and M_{13}>1) (d): Case 4 (M_{12}>1 and M_{13} >1)

$$i_{L13}(\theta_3) = \frac{1}{4 f_{sw} L_{13}}[(2d_{13} - 1)V_1 + n_{33}V_3] \geq 0 \tag{51}$$

$$i_{L13}(\theta_1) = \frac{1}{4 f_{sw} L_{13}}[(1 - 2d_{13})n_{33}V_3 - V_1] \leq 0 \tag{52}$$

$$i_{L13}(\theta_3) = \frac{1}{4 f_{sw} L_{13}}[(2d_{13} - 1)V_1 + n_{33}V_3] + \frac{n_{33}V_3}{4 f_{sw} L_{m3}} \geq 0 \tag{53}$$

where, d_{13} is defined as ϕ_{13}/π and the angle θ_3 is the moment when the switches S_{T2} and S_{T3} are turned off. The equations (50)-(51) are for the inductor current i_{L13} at the angles of θ_1 and θ_3 when the inductor is in Port 3 and the equations (52)-(53) are for the inductor current i_{L13} at the angles of θ_1 and θ_3 when the inductor is in Port 1. Also, β can be defined as L_{m3}/L_{13} as the same manner for the coefficient α.

As the equations (46)-(53) are linear functions of the phase shift ratio d_{12} and d_{13}, these functions have minimum values when d_{12} and d_{13} are zero. Since these equations are linear, the ZVS operation

for a whole load range is guaranteed if $i_{L1}(\theta_1)$ $[(=i_{L12}(\theta_1)+i_{L13}(\theta_1)] \leq 0$, $i_{L12}(\theta_2) \geq 0$ and $i_{L13}(\theta_3) \geq 0$ are satisfied at d_{12} and $d_{13} = 0$.

Referring to the equations (46)-(53) and defining a coefficient k of the inductance ratio as L_{13}/L_{12}. the coefficients α and β can be derived as a function of M_{12} and M_{13} For Case 1, the coefficients α and β can be determined as below according to the equations of (48), (49), (52) and (53) at d_{12} and $d_{13} = 0$:

$$\alpha \leq \frac{M_{12}}{1-M_{12}}, \quad \beta \leq \frac{M_{13}}{1-M_{13}} \tag{54}$$

For Case 2, the coefficients α and β can be determined as follows according to the equations (46), (47), (52) and (53) at d_{12} and $d_{13} = 0$:

$$\alpha \leq \frac{1}{(M_{12}-1)+\frac{1}{k}(M_{13}-1)}, \quad \beta \leq \frac{M_{13}}{1-M_{13}} \tag{55}$$

For Case 3, the coefficients α and β can be determined as follows according to the equations (48), (49), (50) and (51) at d_{12} and $d_{13} = 0$:

$$\alpha \leq \frac{M_{12}}{1-M_{12}}, \quad \beta \leq \frac{1}{k(M_{12}-1)+(M_{13}-1)} \tag{56}$$

In Case 4, the two magnetizing inductances, L_{m2} and L_{m3} concurrently compensate the inductor current for the ZVS operation. In order to have the minimum conduction loss, each magnetizing inductance has to compensate half of the current needed for the ZVS operation in Port 1. As a result, the coefficients α and β are determined as below according to the equations (46), (47), (50) and (51) at d_{12} and $d_{13} = 0$:

$$\alpha \leq \frac{2}{k(M_{12}-1)+(M_{13}-1)}, \quad \beta \leq \frac{2}{(M_{12}-1)+\frac{1}{k}(M_{13}-1)} \tag{57}$$

The two magnetizing inductances L_{m2} and L_{m3} can realize the full range ZVS operation in Dual-transformer three-port DAB converter with the derived equations (54)-(57) for the four different cases.

3.2.4 Simulation and Experimental Results

In order to demonstrate that the proposed converter can interconnect two DC loads at the same time, Port 1 is set as a DC bus, Port 2 and Port 3 are set as load ports respectively. The effectiveness of the proposed converter is verified with PSIM and a 3-kW prototype converter shown in Fig. 3.24. The

TABLE III SYSTEM SPECIFICATIONS AND PARAMETERS FOR DUAL-TRANSFORMER THREE-PORT DAB CONVERTER

Parameter	Symbol	Value
Rated power	-	3 kW
Port 1 voltage (DC bus)	V_1	380 V
Port 2 voltage (DC load 2)	V'_2	380 V
Port 3 voltage (DC load 3)	V'_3	380 V
Power inductor	L'_2	97.7 μH
	L'_3	96.0 μH
Turns ratio	n_{22} (n_{12}/n_2)	1
	n_{33} (n_{13}/n_3)	1
Switching frequency	f_{sw}	50 kHz

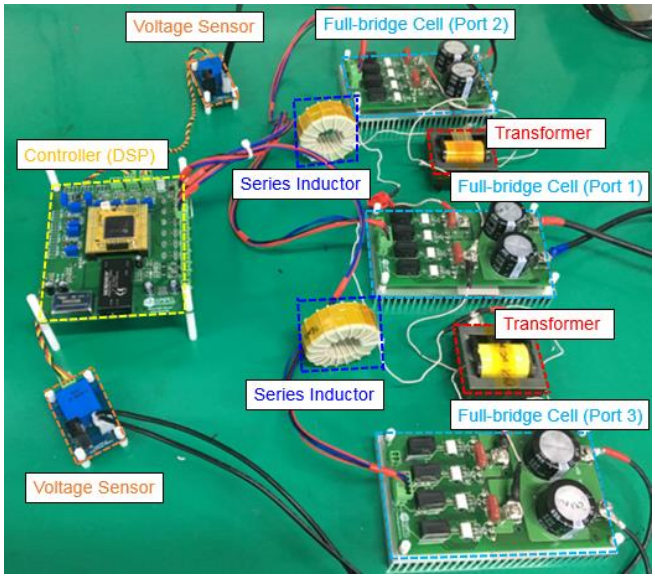

Fig. 3.24 3-kW Dual-transformer three-port DAB converter prototype

converter parameters and specifications for the unity voltage gain case are listed in Table III. The two transformers is designed using EER6062S manufactured by Samhwa Electronics, the two inductances are designed using CH610125 high flux cores by Changsung corporation and SiC MOSFETs, SCT3060AL from Rohm, are used for the switching devices. A TMS320F28335 manufactured by Texas Instruments is used to digitally control the proposed converter.

Fig. 3.25 shows that the steady-state operational simulation results, which denote that each port power is determined with the phase shift value. Fig. 3.25 (a) shows Port 2 and Port 3 take 1-kW and 2-kW, respectively with the phase shift ratio, $\phi_{12} = 0.244$ and $\phi_{13} = 0.506$. Fig. 3.25 (b) depicts that Port 2 and Port 3 absorb 2-kW and 1-kW respectively with the phase shift ratio, $\phi_{12} = 0.515$ and $\phi_{13} = 0.235$. The slight difference of the phase shift values for the swapped load conditions between the load ports

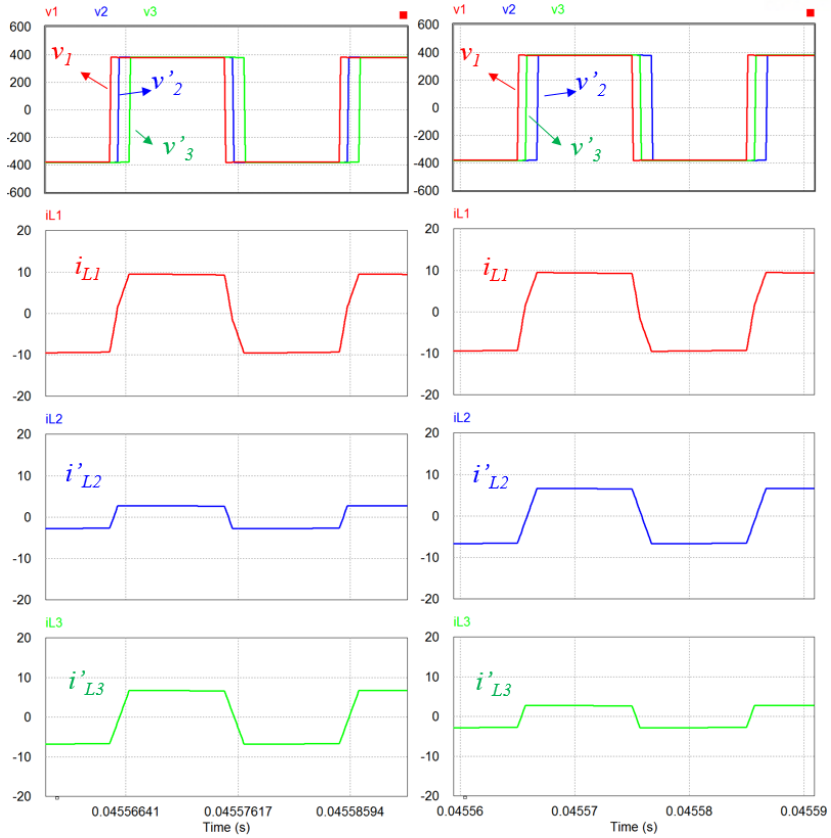

(a) (b)

Fig. 3.25 Steady-state operational simulation results at operating points: (a): $\phi_{12} = 0.244$, $\phi_{13} = 0.506$ (b): $\phi_{12} = 0.515$, $\phi_{13} = 0.235$

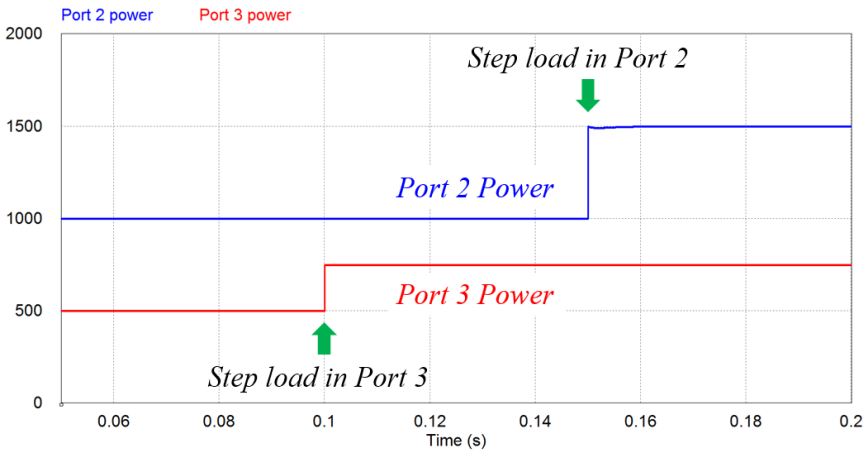

Fig. 3.26 Simulation result of step-load response

is because the two inductance cannot be practically the same. Since it is slightly different, it can be assumed to be symmetric.

Fig. 3.26 illustrates changes of each power at step-load conditions. Port 3 power changes from 500-

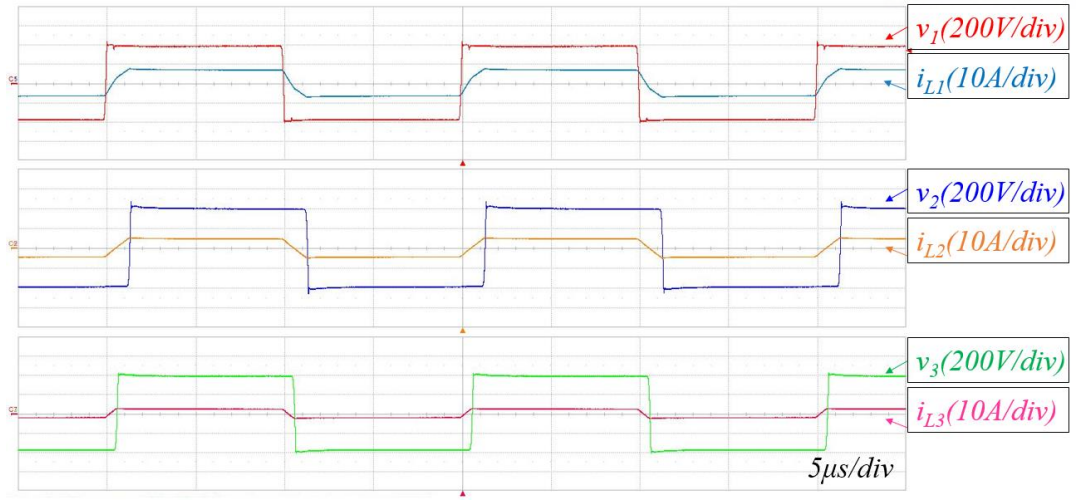

(a)

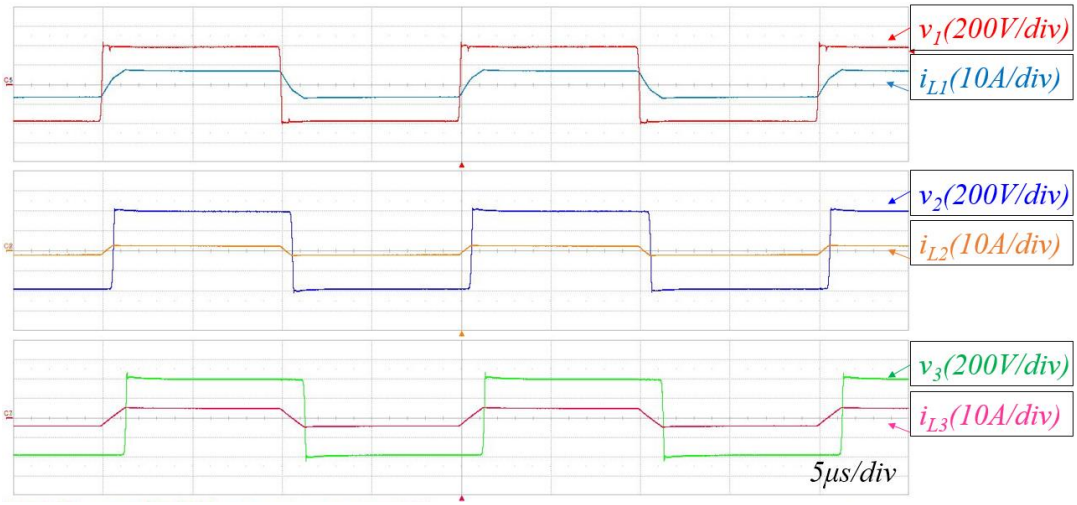

(b)

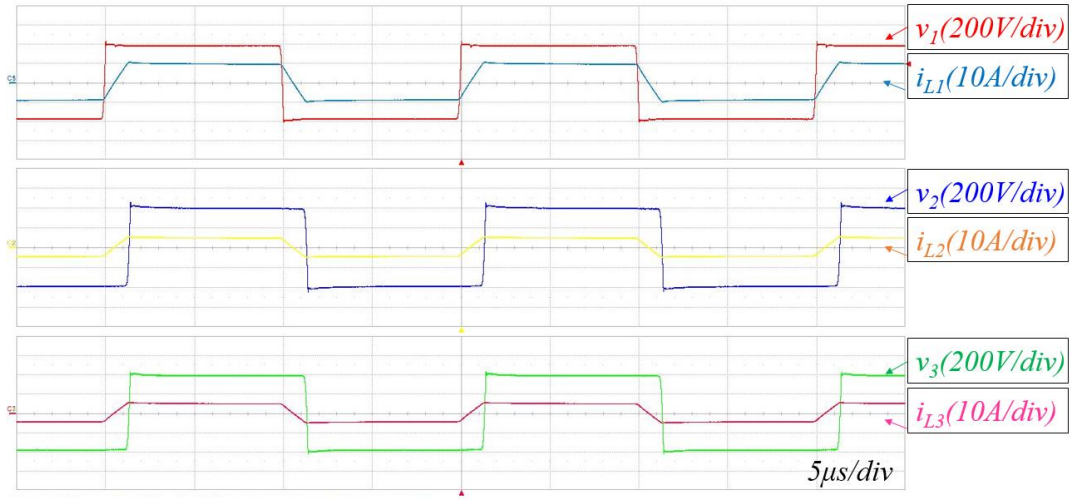

(c)

Fig. 3.27 Steady-state experimental results (a): Port 2 taking 1.5-kW, Port 3 consuming 750-W (b) Port 2 taking 750-W, Port 3 consuming 1.5-kW, (c): Port 2 and Port 3 taking 1.5-kW

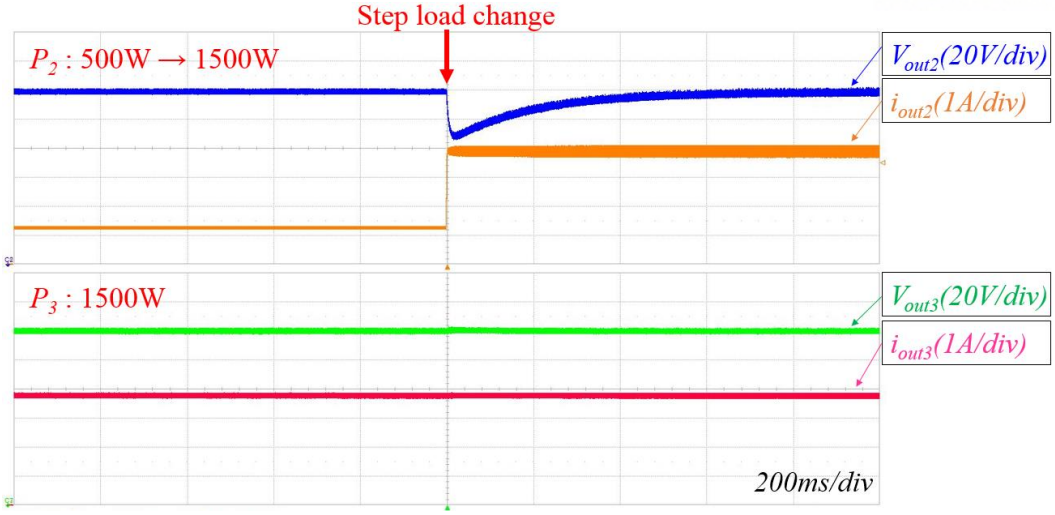

Fig. 3.28 Step-load response in Port 2 changing from 500 W to 1.5-kW with Port 3 at 1.5-kW

TABLE IV CONVERTER PARAMETERS FOR DIFFERENT VOLTAGE GAIN CASES AND DESIGNED MAGNETIZING INDUCTANCES

		Case 1	Case 2	Case 4
Parameter	Symbol	Value	Value	Value
Port 1 voltage	V_1	380 V	380 V	380 V
Port 2 voltage	V'_2	370 V	400 V	400 V
Port 3 voltage	V'_3	360 V	370 V	390 V
Power inductor	L'_2	97.7 μH	97.7 μH	97.7 μH
	L'_3	96.0 μH	96.0 μH	96.0 μH
Turns ratio	n_{22} (n_{12}/n_2)	1	1	1
	n_{33} (n_{13}/n_3)	1	1	1
Switching frequency	f_{sw}	50 kHz	50 kHz	50 kHz
Magnetizing Inductance	L_{m2}	1.16 mH	1.16 mH	1.47 mH
	L_{m3}	0.89 mH	1.21 mH	1.50 mH

W to 750-W at 0.1 sec and Port 2 power varies from 1-kW to 1.5-kW at 0.15 sec. It shows that power change in one port does not influence the other port control. Therefore, the result shows that the proposed converter is a power decoupled system.

Fig. 3.27 depicts the steady-state experimental results using the 3-kW prototype converter under several load conditions. Fig. 3.27 (a) shows the steady-state result where Port 2 takes 1.5-kW with 0.401 rad of the phase shift value ϕ_{12} and Port 3 takes 750-W with 0.191 rad of the phase displacement value, ϕ_{13}. Fig. 3.27 (b) shows the steady-state result where Port 2 takes 750-W with 0.201 rad of the phase shift value ϕ_{12} and Port 3 takes 1.5k-W with 0.392 rad of the phase displacement value, ϕ_{13}. Fig. 3.27 (c) shows the steady-state result under full-load condition where Port 2 and Port 3 take 1.5-kW, respectively with ϕ_{12} = 0.401 rad and ϕ_{13} = 0.392 rad.

Fig. 3.28 illustrates the step-load response experimental result. Port 2 step-changes from 500-W to

1.5-kW while Port 3 remains at 1.5-kW. Port 2 has 200-ms of the settling time during the step-load change. Meanwhile, Port 3 remains at 1.5-kW without any change. It shows that the two load ports are independently controlled.

Table IV lists the converter parameters for different voltage gain cases and their corresponding designed magnetizing inductance for the ZVS operation. In Case 1, the voltage gain M_{12} and M_{13} are smaller than unity. The coefficients α and β can be calculated as 37 and 18 according to the equations (54). To practically guarantee the ZVS operation, margin for the magnetizing inductance is also added (See APPENDIX.B). The magnetizing inductances L_{m2} and L_{m3} are calculated as in the table IV. Since Case 2 and Case 3 are the symmetric case, only Case 2 is considered in the experimental results. For Case 2 and Case 4, the magnetizing inductances can be calculated in the same manner above.

Fig. 3.29 shows that the experimental results at turn-on transition under no load condition using the parameters listed in Case 1 of Table IV without the magnetizing inductances. Due to the voltage gain M_{12} and M_{13} that are smaller than unity, Port 1 has the ZVS operation, but Port 2 and Port 3 have the hard switching operation, which can cause stress on the switching devices and lowers the efficiency.
Fig. 3.30 shows that the experimental results at turn-on transition under no load condition with the designed 1.16 mH and 0.89 mH of magnetizing inductances L_{m2} and L_{m3}, respectively listed in Table IV. The magnetizing inductances L_{m2} and L_{m3} compensate corresponding load port. Therefore, Port 2and Port 3 have the ZVS operation.

Fig. 3.31 shows that the experimental results at turn-on transition under no load condition using the parameters listed in Case 2 of Table IV without the magnetizing inductances. Due to the voltage gain M_{12} that is greater than unity and M_{13} that is smaller than unity, Port 2 has the ZVS operation, but Port 1 and Port 3 have the hard switching operation. Fig. 3.32 shows that each port achieves the ZVS operation under no load condition with the designed 1.16 mH and 1.21 mH of magnetizing inductances L_{m2} and L_{m3}, respectively.

Fig. 3.33 depicts that the experimental results at turn-on transition under no load condition using the parameters listed in Case 3 of Table IV without the magnetizing inductances. Due to the voltage gain M_{12} and M_{13} that are greater than unity, Port 2 and Port 3 have the ZVS operation, but Port 1 has the hard switching operation. Fig. 3.34 shows that each port achieves the ZVS operation under no load condition with the designed 1.47 mH and 1.81 mH of magnetizing inductances L_{m2} and L_{m3}, respectively.

Fig. 3.35 illustrates the efficiency curves of Dual-transformer three-port DAB converter without the designed magnetizing inductance and the same converter with the designed magnetizing inductance. As the proposed method can realize the full ZVS operation, it brings higher efficiency below 500-W load conditions. The largest efficiency difference is 4.0 % at 100-W load condition. The proposed method brings lower efficiency since Dual-transformer three-port DAB converter can have the ZVS operation under heavy load condition and the proposed method has higher core loss.

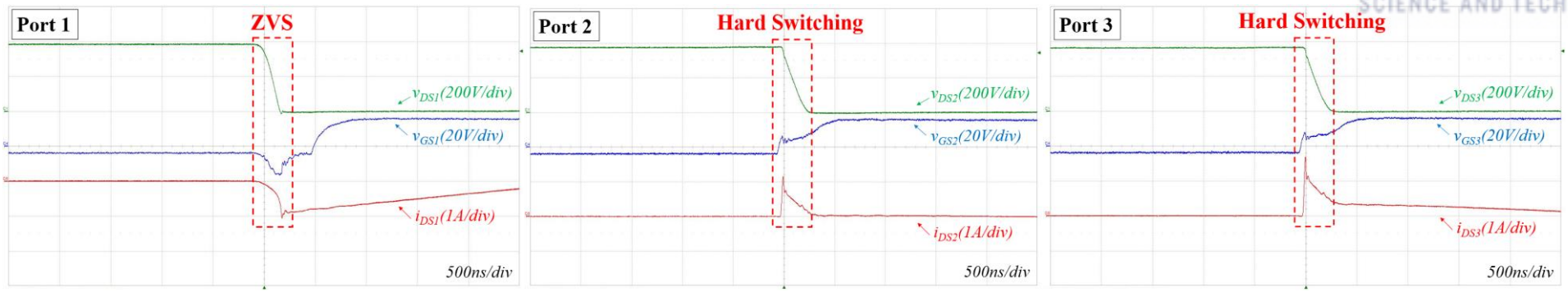

(a) (b) (c)

Fig. 3.29 Case 1: Experimental results at turn-on transition without designed magnetizing inductances (a): Port 1, (b): Port 2, (c): Port 3

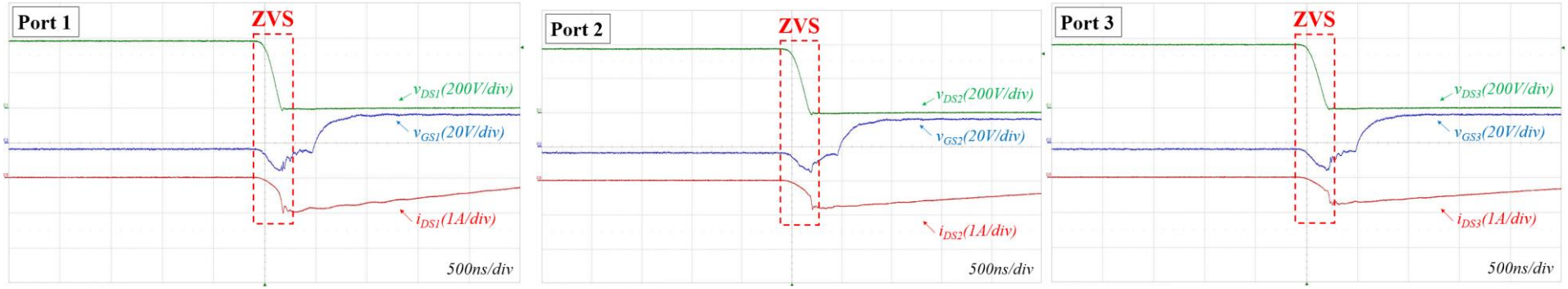

(a) (b) (c)

Fig. 3.30 Case 1: Experimental results at turn-on transition with designed magnetizing inductances (a): Port 1, (b): Port 2, (c): Port 3

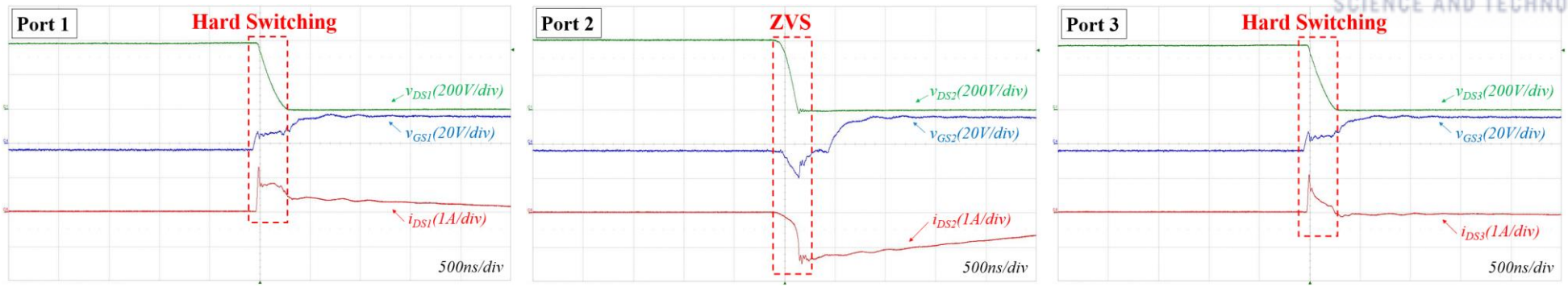

(a) (b) (c)

Fig. 3.31 Case 2: Experimental results at turn-on transition without designed magnetizing inductances (a): Port 1, (b): Port 2, (c): Port 3

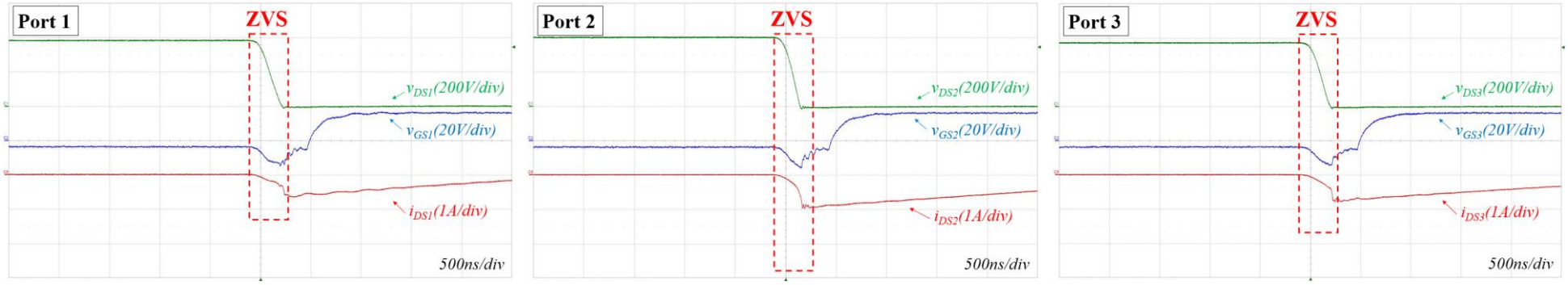

(a) (b) (c)

Fig. 3.32 Case 2: Experimental results at turn-on transition without designed magnetizing inductances (a): Port 1, (b): Port 2, (c): Port 3

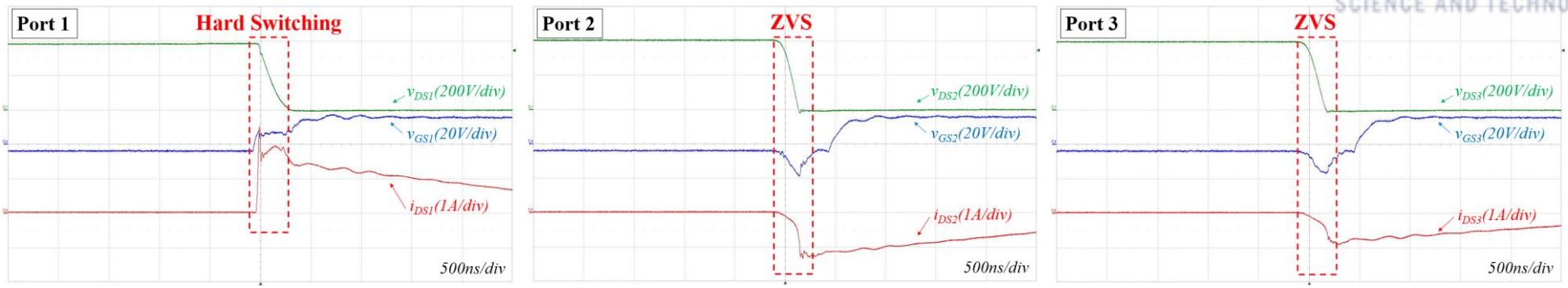

(a) (b) (c)

Fig. 3.33 Case 4: Experimental results at turn-on transition without designed magnetizing inductances (a): Port 1, (b): Port 2, (c): Port 3

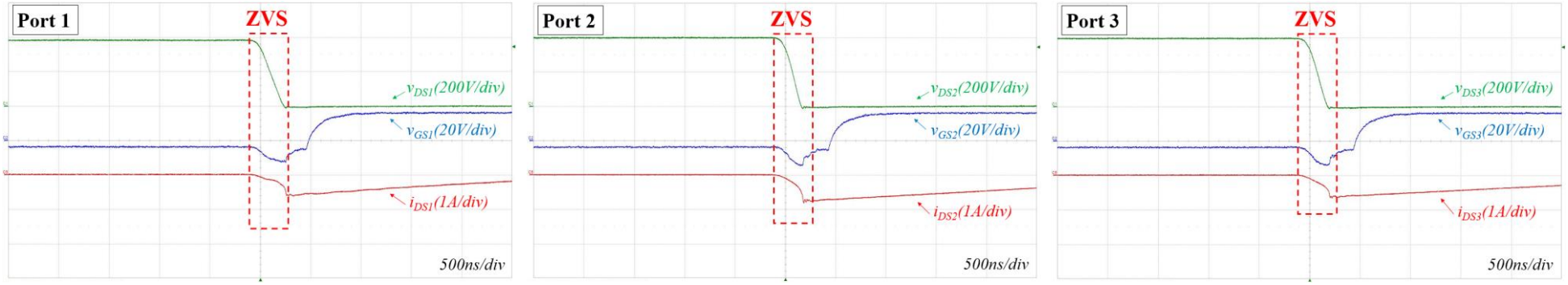

(a) (b) (c)

Fig. 3.34 Case 4: Experimental results at turn-on transition without designed magnetizing inductances (a): Port 1, (b): Port 2, (c): Port 3

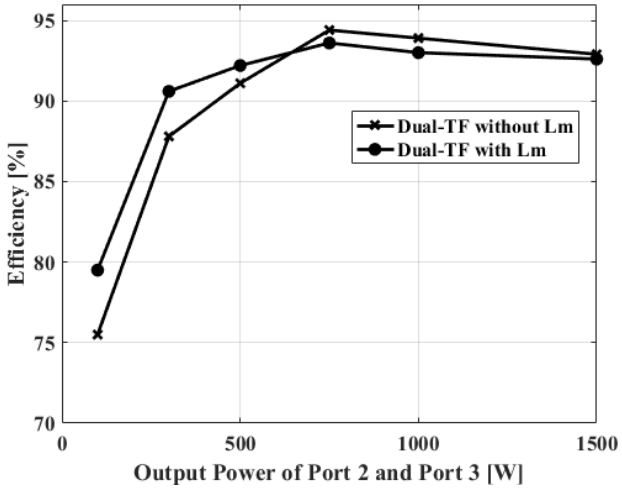

Fig. 3.35 Efficiency curves over change of Port 2 and Port 3 power for Case 1

In this section, a magnetizing inductance design method proposed to have the full ZVS operation with Dual-transformer three-port DAB converter. The operational principles and the decoupled system of Dual-transformer three-port DAB converter are explained and verified with PSIM and experimental results. Also, the proposed magnetizing design method is experimentally demonstrated. In the simulation experimental and results, the proposed converter can transfer power with the phase shift values under several load conditions. The dynamic response shows the proposed converter is a decoupled system. In the result, Port 1 is controlled to 380 V at a step-load condition with 200-ms of the settling time while Port 3 remains the same without any change. In the turn-on transition experimental results, the proposed magnetizing design method effectively widens the ZVS operation for different voltage gain cases. The converter using the proposed method has higher efficiency under 500-W that are 4 %, 2.8 % and 1.1 % higher at 100-W, 300-W and 500-W conditions, respectively. As a result, Dual-transformer three-port DAB converter can be implemented with simple control. Also, by using the proposed magnetizing design method, the converter does not only have higher efficiency under light load conditions but also protect the switching devices.

Ⅳ. Isolated Voltage Balancer for Bipolar LVDC Distribution

A bipolar low-voltage DC (LVDC) distribution system used in residential and building applications requires AC-DC converters and voltage balancers that balance the two DC pole voltages. The bipolar DC pole voltage level only relies on the voltage balancer tied with the AC grid. Two-inductor three-port DAB converter using ESS with the voltage balancing capability is used to prevent the bipolar voltage level collapse caused by the failure of the grid-tied voltage balancer. It can balance the bipolar DC voltage level without complicated control. In addition, it has lower current stress in switching devices than that of the conventional three-port DAB converter. The validity of the proposed converter is demonstrated with a 3-kW prototype converter.

4.1 Proposed Voltage Balancer Structure

DC distribution systems have a variety of attractions compared with the conventional AC distribution systems due to the development of power electronics technologies and the good connectivity of renewable energy sources [1]-[3]. As digital loads demanding DC power have become the majority in the modern society, LVDC distribution systems have been getting attention as an alternative solution for residential and building applications. The LVDC distribution system can supply electricity with higher efficiency and less energy conversion stages, no AC resistance in the distribution [28], [29]. A bipolar LVDC distribution system brings more distinct benefits than unipolar DC distribution [29], [30]. It gives three different voltage levels, which provides flexibility in connection and high safety with reduced voltage levels according to the ground. Furthermore, even if faults occur in one of the DC poles, the other one can be still working. It can ensure high reliability of the distribution system.

The bipolar DC poles cannot be maintained at the same voltage level under unbalanced load conditions without a voltage balancer [31]-[33]. Various types of voltage balancers connected to the AC grid have been proposed to solve the above-stated issue with different characteristics. A buck-boost voltage balancer with a half-bridge has been proposed [31]. It has high cost-effectiveness due to the small quantity of components. A dual-buck voltage balancer has been proposed to prevent the system from the arm-short problem that the bridge-type voltage balancer has [32]. A three-level voltage balancer has been developed to withstand high voltage stress for high voltage DC distribution [33].

The bipolar DC voltage level of the LVDC distribution system is regulated by the AC grid-tied voltage balancer. If failures lie in the grid-tied voltage balancer, the bipolar voltage levels cannot be sustained. Therefore, several back-up voltage balancers are required to improve the system reliability [34]. An ESS charger with the bipolar voltage balancing capability has been proposed [35] as an auxiliary voltage balancer. It is an enhanced three-level type voltage balancer, which has the low quantity of components. However, it is a non-isolated type balancer. The ESS adopted to the LVDC

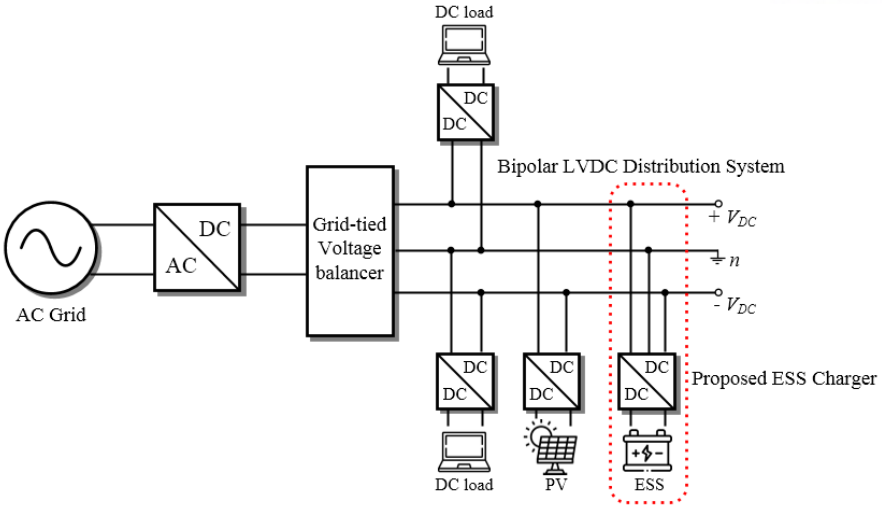

Fig. 4.1 Schematics of bipolar LVDC distribution system with the proposed back-up converter employing voltage balancing capability with ESS

distribution system is mostly used for residential and building applications, which is highly accessible to people. It can cause a hazard to people who accidentally contact the ESS [30], [36]. Electric isolation between the ESS and the grid is recommended to meet the safety requirement as well as for protecting operators during maintenance [36], [37]. Therefore, the earlier-stated non-isolated voltage balancers cannot be used for the back-up balancer using ESS applied to the residential and building applications.

The conventional three-port DAB converter derived can be used as a charger [12]. It has a galvanic isolation with a high-frequency transformer and bidirectional power transfer capability that is necessary for charger applications, which are all explained in Chapter 2. However, it has the power coupling among the three ports due to the cross-coupled loops made by its structure, which may bring control complexity for regulating the two DC poles of the bipolar LVDC distribution system. To overcome the power coupling issue, power decoupling methods have been introduced [12], [13]. This method is implemented by composing a look-up table of decoupling matrices calculated and stored in advance at every single operating point. As a result, it leads to highly complex control and may be a burden to controller

Two-inductor three-port DAB converter is used with the advantages of the galvanic isolation and the bidirectional power control capability. The proposed converter can overcome the power coupling issue among the ports without any additional control. Therefore, using a simple control algorithm, the converter can regulate the bipolar DC pole voltage levels at the grid-tied voltage balancer failure condition. Furthermore, it has less current stress, which can improve overall power conversion efficiency comparing with the conventional converter. Using the proposed converter, the ESS can balance the bipolar DC voltage level for a longer time with the same amount of energy during the AC grid-tied voltage balancer failure.

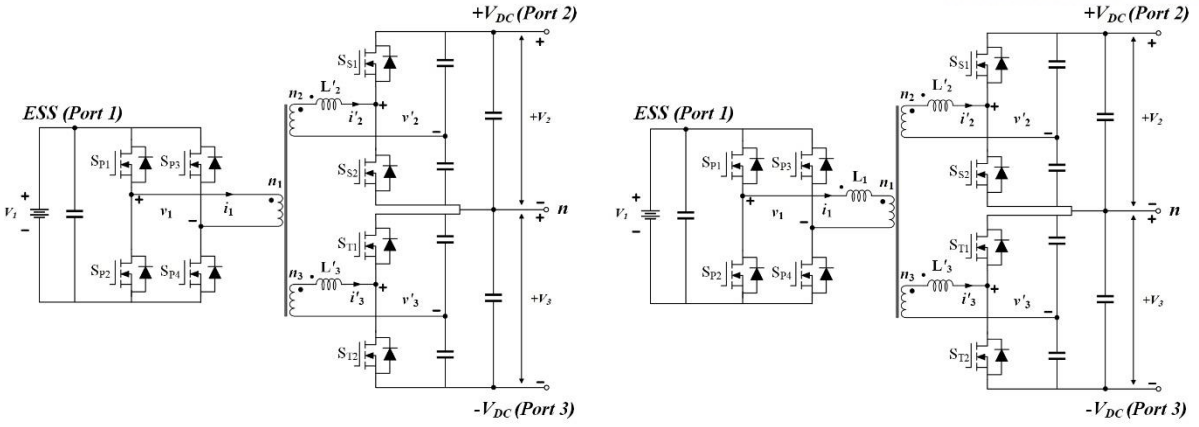

Fig. 4.2 Converter schematics: (a) Two-inductor three-port DAB converter, (b) The conventional three-port DAB converter

Fig. 4.1 shows a bipolar LVDC distribution system with the proposed ESS charger. As previously stated, to keep the same voltage level in both of the DC poles even during the faults of the grid-tied voltage balancer, the ESS must be accessible to the DC pole pair. Two-inductor three-port DAB converter connected to the bipolar DC pole lines is depicted in Fig. 4.2 (a). Port 1 is the ESS port, and the other two ports, Port 2 and Port 3 linked in series are attached to the bipolar DC pole lines with the neutral point *n*.

A full-bridge is used to the ESS port to deal with the electric power provided to both the DC poles. A half-bridge is used for each DC pole port as they handle less power than the power that the ESS port takes. The three ports are magnetically coupled by a three-winding transformer. The transformer provides galvanic isolation between the ESS and the grid as well as adjusts voltage difference among the ports. An external power inductor is located at each DC pole port as a power transfer element. The external inductors can be integrated into the transformer, which requires large leakage inductance. However, it is hard to design such integrated transformers because heat generated by high leakage flux is concentrated on the magnetic core. The external inductors are used in this research for the design simplicity.

4.2 Theoretical Analysis

4.2.1 Voltage Balancing Operation

The proposed converter can balance the bipolar voltage level by controlling each DC pole voltage since it can independently transfer the electric power to each DC pole without any interference among the ports. The power transfer of the proposed converter is determined by control variables that are the

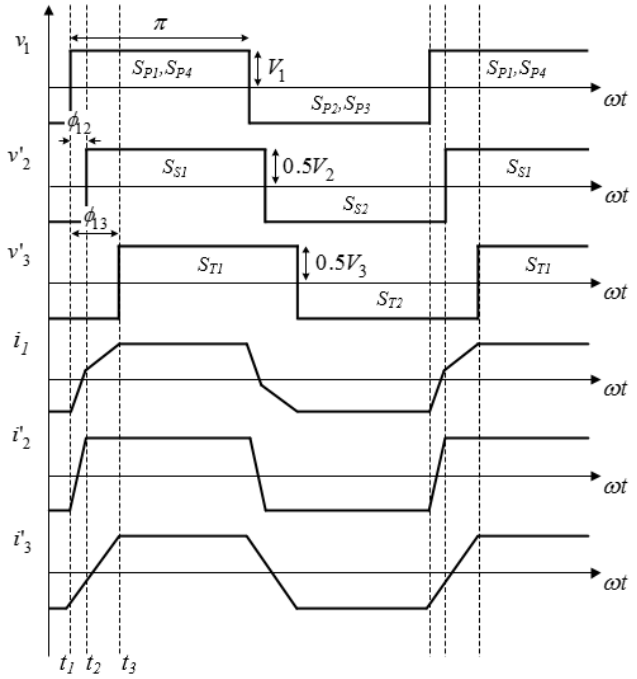

Fig. 4.3 Theoretical operating waveforms of the proposed converter

voltage phase displacements with respect to that of v_1. Each port power equation is described as the equations (25)-(28).

If the system is ideal without power loss, theoretical operating waveforms can be illustrated as Fig. 4.3 It depicts that the voltages applied to the inductance network shown in Fig. 3.2 determine the inductor currents (i_1, i_2 and i_3). Since the current through L_{23} is assumed to be zero, the current i1 is sum of the current i_2 and i_3. Therefore, the two DC pole ports are seen as connected to the ESS port in parallel.

The proposed converter can independently control the two output voltage levels with a simple control method using two PI controllers. The proposed converter does not have the cross-coupled control loops that can unbalance the bipolar voltage level, which the conventional converter suffers from. It has already been explained in Chapter 3 (See Chapter 3.2.1). It is eliminated by the converter structure without extra control. Therefore, the two output voltage levels can be sustained even under different load conditions since the two PI controllers control the corresponding DC pole voltage without interference between each DC pole.

The system matrix G shown in the equation (34) is a diagonal matrix, which depicts that the proposed converter is able to independently control each pole voltage level using the corresponding phase displacement variables. The balancing strategy can be achieved by setting the reference voltage phase of the inductor-less port. Otherwise, the off-diagonal elements G_{12} and G_{21} cannot become zero, which brings difficulty in the control of the voltage balancing. Fig. 4.4 shows the proposed converter control diagram of the voltage balancing operation. It only requires two PI controllers since the off-diagonal

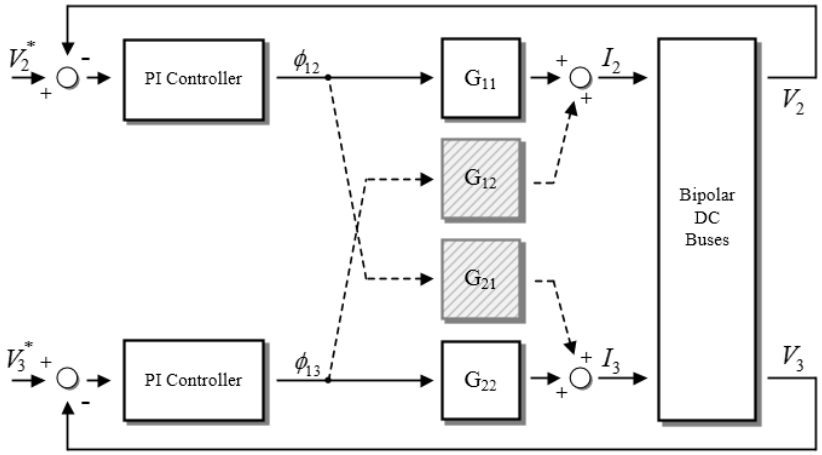

Fig. 4.4 Control block diagram of the proposed converter with balancing capability for bipolar DC pole voltage levels

elements are eliminated because of the structure. Therefore, the proposed converter has the simple control algorithm to balance the DC pole voltages without additional control strategies.

4.2.1 Current Stress Reduction

The proposed converter has lower current stress than that of the conventional converter. The reason why the conventional converter has high current stress in a leakage power path between Port 2 and Port 3, which does not exist in the proposed converter. It shows that Port 2 power and Port 3 power are not only determined by their own corresponding voltage phase displacements with respect to that of Port 1, but the leakage power also occurs through the path between them by their voltage phase difference. For instance, to idle Port 2 at zero power, P_{12} that is the power supplied from Port 1 to Port 2 must be the same as P_{23}, which is the power transferring from Port 2 to Port 3. The net power is zero, but large reactive power can be created, which leads large current stresses in the DAB converters [8], [12].

Smaller current rated power switching devices and magnetic components can be used in the proposed converter. In addition, the reduced current stress brings the higher efficiency in the DAB converters [8]. Therefore, the proposed converter can balance the DC pole voltages for a longer time with the same amount of energy left in the ESS. The current stress of the proposed converter that is smaller than that of the conventional converter is able to be derived by the volt-second balance principle as follows [8]:

$$i_2(t_1) = -\frac{1}{4 f_{sw} L_{12}}[(2d_2 - 1)(n_{12} 0.5V_2) + V_1] \tag{58}$$

$$i_2(t_2) = \frac{1}{4 f_{sw} L_{12}}[(2d_2 - 1)V_1 + (n_{12} 0.5V_2)] \tag{59}$$

$$i_2(t_3) = \frac{1}{4 f_{sw} L_{12}}[(2d_3 - 1)V_1 + (1 + 2d_2 - 2d_3)(n_{12}\, 0.5V_2)] \tag{60}$$

$$i_3(t_1) = -\frac{1}{4 f_{sw} L_{13}}[(2d_3 - 1)(n_{13}\, 0.5V_3) + V_1] \tag{61}$$

$$i_3(t_2) = \frac{1}{4 f_{sw} L_{13}}[(2d_3 - 2d_2 - 1)(n_{13}\, 0.5V_3) + (1 - 2d_2)V_1] \tag{62}$$

$$i_3(t_3) = \frac{1}{4 f_{sw} L_{13}}[(2d_3 - 1)V_1 + (n_{12}\, 0.5V_2)] \tag{63}$$

where d_2 ($=\phi_{12}/\pi$) and d_3 ($=\phi_{13}/\pi$) are each DC pole port phase displacement duty ratio corresponding to the reference voltage v_1, respectively.

As previously stated, in the proposed converter structure, Port 2 and Port 3 are connected to Port 1 in parallel because it has no link between Port 2 and Port 3. Therefore, Port 1 transformer current is the sum of the other port inductor currents as below:

$$i_1(t_x) = i_2(t_x) + i_3(t_x) \tag{64}$$

where, x = 1, 2 and 3. The current stress of the proposed converter in each port is defined as the peak current value. In order to simplify the analysis, equivalent voltages and inductances have same values: $V = V_1 = 0.5n_{12}V_2 = 0.5n_{13}V_3$, L = $L_2 = L_3$ and $L_1 = 0$. The current stress for each port can be simplified, which appear at time t_1.

$$i_{1,\max,pr} = |i_1(t_1)| = \frac{V}{2 f_{sw} L}(d_2 + d_3) \tag{65}$$

$$i_{2,\max,pr} = |i_2(t_1)| = \frac{V}{2 f_{sw} L}(d_2) \tag{66}$$

$$i_{3,\max,pr} = |i_3(t_1)| = \frac{V}{2 f_{sw} L}(d_3) \tag{67}$$

In order to compare the current stress, the conventional converter current stresses can be derived by using $L_1 = L$, which is the same manner above:

$$i_{1,\max,co} = |i_1(t_1)| = \frac{V}{2 f_{sw} L}[(d_2 + d_3)/3] \tag{68}$$

$$i_{2,\max,co} = |i_2(t_2)| = \frac{V}{2 f_{sw} L}(d_3/3) \tag{69}$$

$$i_{3,\max,co} = |i_3(t_1)| = \frac{V}{2 f_{sw} L}[(2d_3 - d_2)/3] \tag{70}$$

In order to normalize the derived values, the normalized coefficients of the derived power and current

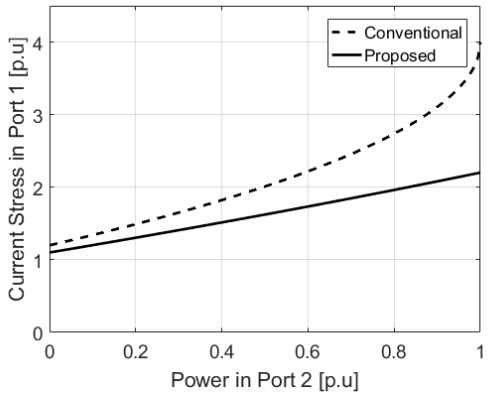

(a)

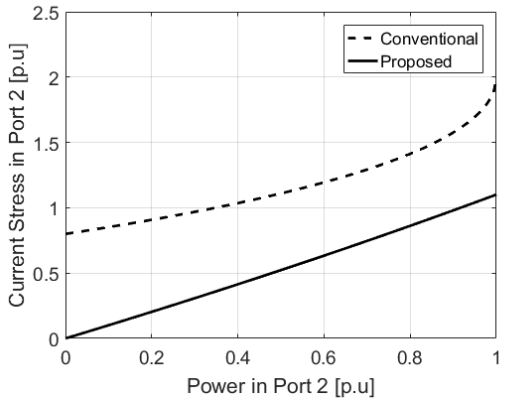

(b)

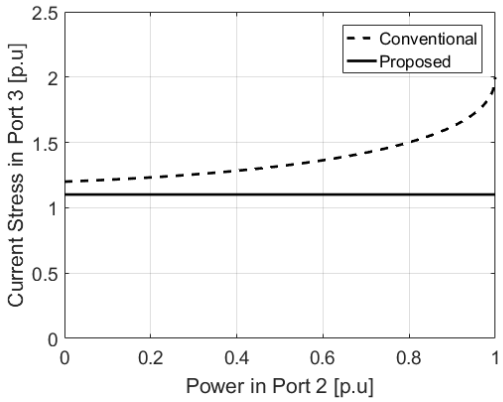

(c)

Fig. 4.5 Current stress comparison between the conventional converter and the proposed converter in each port at P_3 = 1.0 *pu* fixed: (a) Port 1, (b) Port 2, (c) Port 3

can be defined as follows:

$$P_N = VI_N = \frac{V^2}{24 f_{sw} L} \quad \text{where,} \quad I_N = \frac{V}{24 f_{sw} L} \tag{71}$$

Fig. 4.5 depicts the comparison of each port current stress in the conventional and proposed converters at P_3 = 1.0 *pu* with equations (5), (28) and (65)-(70) divided by P_N and I_N. It denotes the proposed converter has smaller current stress than that of the conventional converter.

3.3 Experimental Results

A 3-kW prototype voltage balancer depicted in Fig. 4.6 is used to obtain experimental results to demonstrate its effectiveness. The converter parameters and specifications are listed in Table V. IPW65R041 from Infineon, MOSFETs are installed at the three power bridges of the converter. The three-winding transformer is designed by an EER6062S ferrite core. The two inductances are designed as the same inductance for the equal power capability in both the two DC poles. They are designed with

TABLE V SYSTEM SPECIFICATIONS AND PARAMETERS FOR THE PROPOSED VOLTAGE BALANCER

Parameter	Symbol	Value
Rated power	-	3 kW
ESS voltage	V_1	200 V
Bipolar bus voltage	V'_2	380 V
	V'_3	380 V
Power inductor	L'_2	33.7 μH
	L'_3	32.6 μH
Turns ratio	n_{22} (n_{12}/n_2)	1
	n_{33} (n_{13}/n_3)	1
Switching frequency	f_{sw}	25 kHz

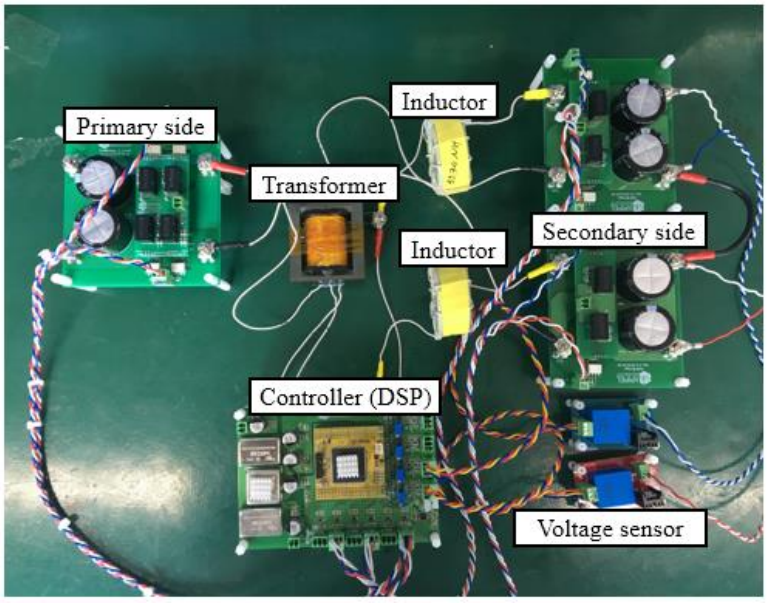

Fig. 4.6 3-kW prototype proposed voltage balancer photograph

external inductors using CH610125 cores. The control strategy is operated by a TMS320F28335 DSP from Texas Instruments.

Fig. 4.7 illustrates the steady-state operations of the proposed converter to demonstrate the voltage balancing operation. It shows the proposed voltage balancer is able to balance the bipolar DC voltage level under both balanced and unbalanced load conditions. It can be achieved by independently transferring power to each bus with their corresponding voltage phase displacements of ϕ_{12} and ϕ_{13}. Fig. 4.7 (a) depicts the steady-state operational waveforms under the balanced full load condition providing 1.5 kW for both the DC poles. The bipolar DC pole voltage levels of V_2 and V_3 are controlled to 380 V with 20° of the voltage phase shifts of ϕ_{12} and ϕ_{13}. In Fig. 4.7 (b), one DC pole (Port 2) operates under the full load condition during the other DC pole (Port 3) under the no load condition. The bipolar DC pole voltage levels are balanced to 380 V. The phase displacement of Port 2, ϕ_{12}, is 20° as equal as

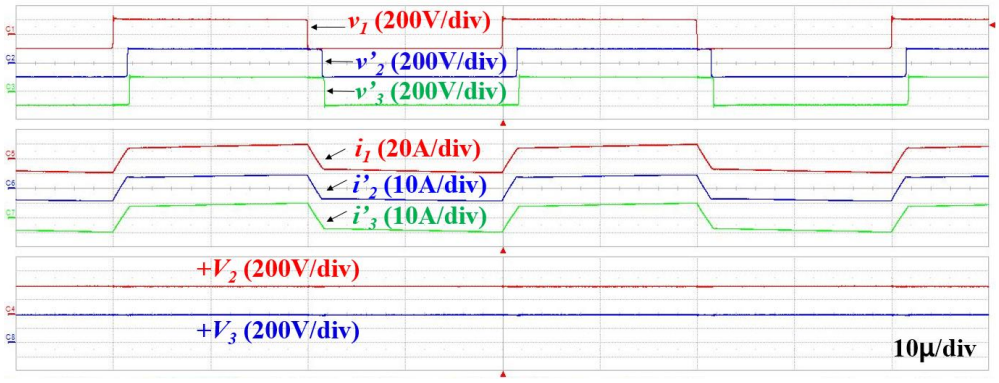

(a)

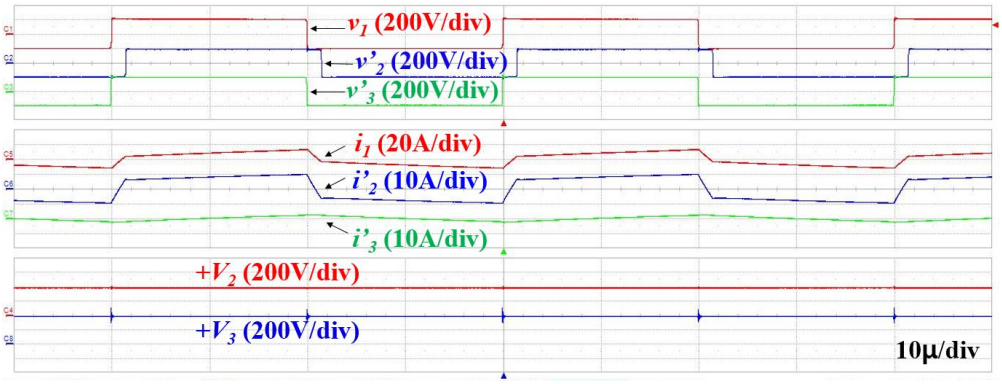

(b)

Fig. 4.7 Steady state experimental operational waveforms under (a): 3 kW (P_2 = 1.5 kW, P_3 = 1.5 kW) (b): 1.5 kW (P_2 = 1.5 kW, P_3 = 0 W)

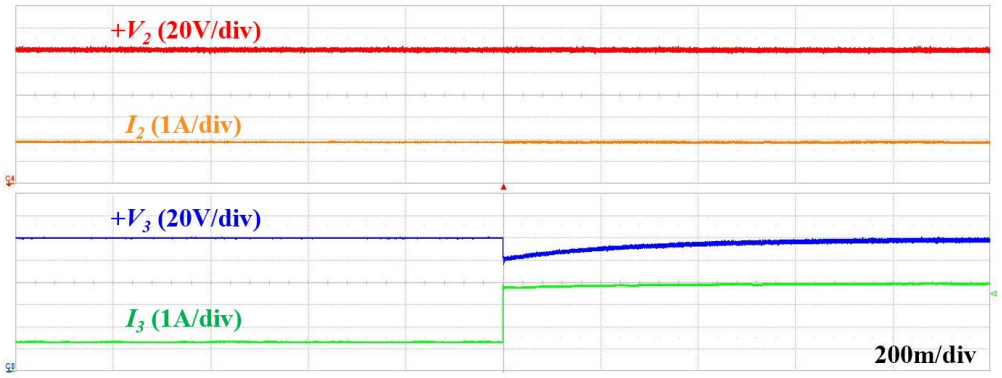

Fig. 4.8 Dynamic response experimental waveforms (P_2 = 750 W and P_3 = 500 W to 1.5 kW)

the one in Fig. 4.7 (a). However, the other voltage phase shift of Port 3, ϕ_{13}, is in phase with the reference voltage phase. Since the converter separately regulates the two bipolar DC poles, only ϕ_{13} is changed under the unbalance load condition.

Fig. 4.8 depicts the experimental result of the dynamic response in the proposed voltage balancer. Port 3 power changes from 500 W to 1.5 kW while Port 2 keeps the output power to 750 W. Port 3

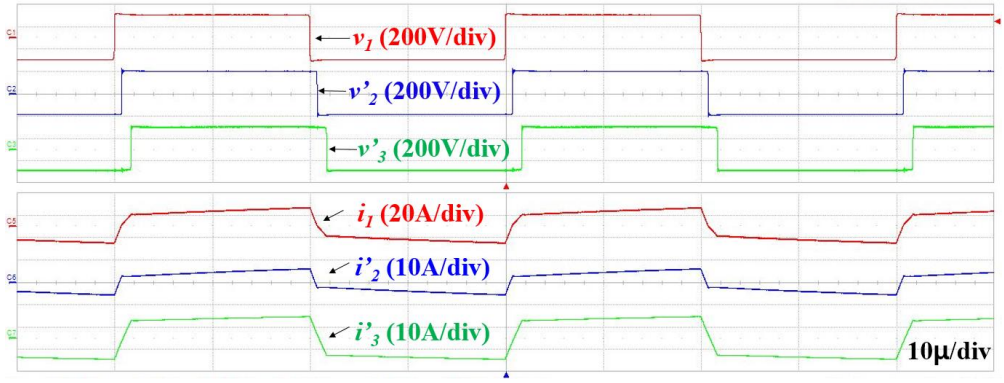

(a)

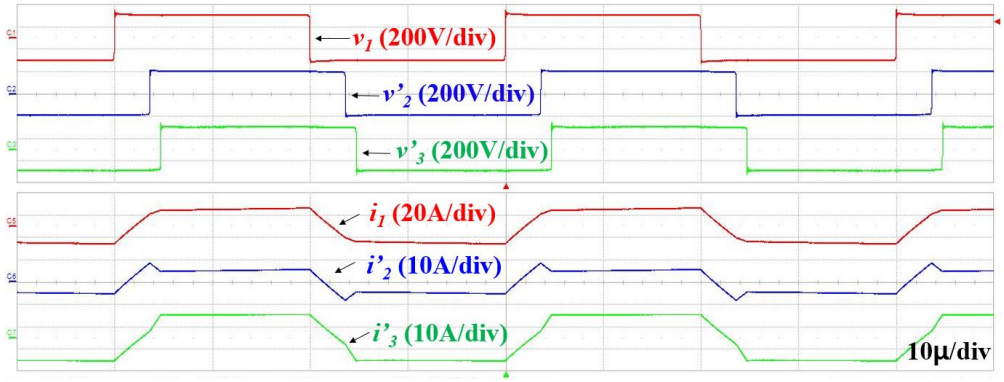

(b)

Fig. 4.9 Steady state operational waveforms under the power conditions of P_2 = 750 W and P_3 = 1.5 kW (a) in the proposed converter (b) in the conventional converter

balances its bus voltage to 380 V with 200-ms of settling time and Port 2 well regulates the same voltage level even under the load step-changes in Port 3. As a results, there is no interference of the voltage regulation operation between the two DC poles. The step-load response denotes that the power change in one port does not affect the other port in power control manner. In other words, the two bipolar DC poles are effectively decoupled without any extra controls in the proposed voltage balancer.

Fig. 4.9 shows the steady-state operational waveforms of the proposed converter to compare the current stress between the conventional and proposed converters. In Fig. 4.9 (a), the peak current for each port is $i_{1,max}$ = 15.6 A, $i_{2,max}$ = 5.9 A and $i_{3,max}$ = 9.5 A, respectively, in the proposed converter. The conventional converter shows the peak current for each port of $i_{1,max}$ = 16.7 A, $i_{2,max}$ = 8.5 A and $i_{3,max}$ = 10.5 A, respectively, which are shown in Fig. 4.9 (b). The current stresses are reduced by 6.6 %, 30.6 % and 10.5 % in Port 1, Port 2 and Port 3, respectively. The difference of the peak current is from the leakage path formed by L_{23} located in the conventional converter. It creates more reactive power than the proposed converter due to the additional leakage path.

Fig. 4.10 shows the efficiency curves of the conventional and proposed converters according to power variations at Port 2 with a fixed power of 1.5 kW at Port 3. The proposed converter shows higher

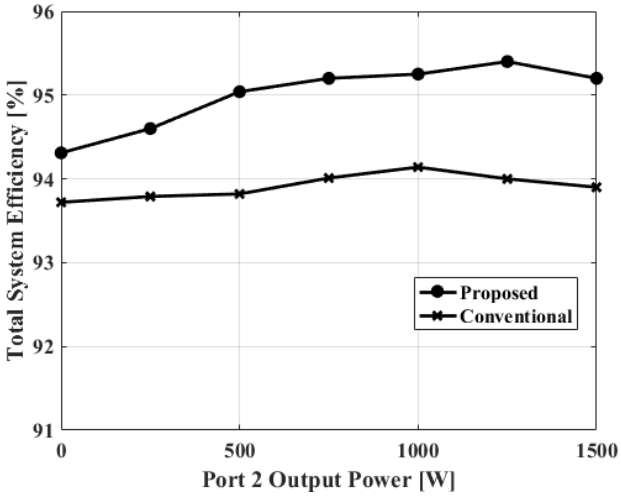

Fig. 4.10 Efficiency curves over output power change at Port 2 (P_3 = 1.5 kW fixed)

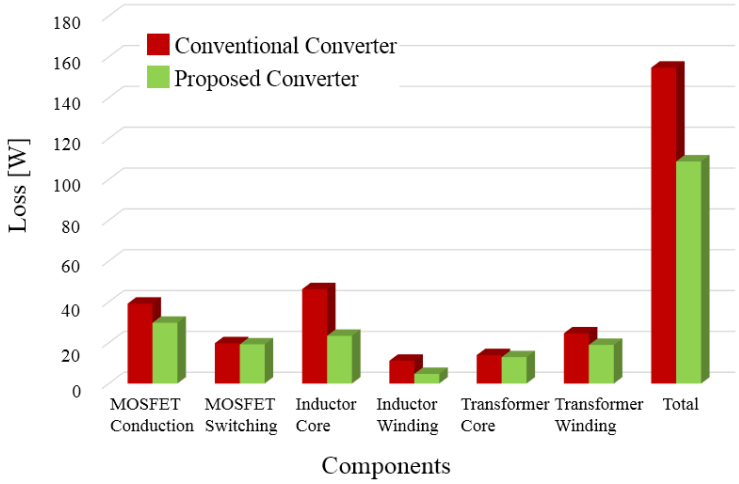

Fig. 4.11 Estimated loss comparison at $P_2 = P_3$ = 1.5 kW

efficiency according to all the load ranges than that of the conventional converter. It is because the high current stress makes high conduction loss and high core loss in the conventional converter. Furthermore, the proposed converter has only two inductors, which brings lower conduction and core losses than those of the conventional converter that has three inductors. Therefore, Two-inductor three-port DAB voltage balancer denotes higher efficiency with reduced current stress and smaller quantity of inductor cores than the conventional converter. The proposed converter has more than 94 % efficiency over entire load ranges. The biggest efficiency difference between the proposed and conventional converters is 1.4 % at 1250 W in Port 2.

The efficiency difference comes from conduction loss and the inductor core loss as shown illustrated in Fig. 4.11 (Calculation procedure in detail is in APPENDIX.C). The estimated total loss difference is 45.9 W. It is 1.5 % difference in efficiency. The proposed converter has 9.4-W lower MOSFET

conduction loss, 6.5-W smaller inductor winding loss and 5.7-W lower transformer winding loss. Besides, it has one less core loss portion in Port 1, which brings 22.9 W less loss. Consequently, the proposed converter has lower loss due to less conduction loss and core loss.

In this chapter, Two-inductor three-port DAB converter is used as the voltage balancer for the bipolar DC pole system. The converter structure and operational principles are explained. The benefits of the proposed converter that are the simple control for the voltage balancing capability and the reduced current stress, are theoretically analyzed. In the experimental results, the bipolar voltage level is balanced to 380 V under various load conditions. The dynamic response shows that Port 3 balances its bus voltage level to 380 V during the step-load while Port 2 voltage is balanced without any influences. In the current stress comparison, the biggest reduction of the current stress is 30.6 % in the proposed converter. As a result, the proposed converter shows higher efficiency because of reduced current stress and only two inductors comparing with the conventional converter. The efficiencies are 0.6 % and 1.4 % higher than those of the conventional converter at the low and high load powers, respectively. The proposed converter has more than 94 % efficiency over the whole load ranges. Therefore, Two-inductor three-port DAB converter can be used as the voltage balancer employing the ESS with its voltage balancing capability in case of main voltage balancer failures.

Ⅴ. Conclusion

In this thesis, two advanced three-port DAB converters, which are Two-inductor three-port DAB converter and Dual-transformer three-port DAB converter have been proposed to reduce the control complexity that the conventional converter has, and achieve higher power density and higher efficiency.

Elimination of the power coupling issue and reduction of circulating current in one port idling is theoretically analyzed and discussed in Two-inductor three-port DAB converter. The performance and the benefits are demonstrated with a 5-kW prototype Two-inductor three-port DAB converter. In the simulation and experimental results, the steady-state waveforms prove that the converter can transfer in any direction, the step-load response shows that the converter has a decoupled system without extra control and the one port idling waveforms denotes that it has reduced circulating current.

The operational principles and the absence of the power coupling issue of Dual-transformer three-port DAB converter are explained and the magnetizing inductance design methodology is also proposed to achieve the full ZVS operation. It has multiple transformer rather than a single transformer that the other converters stated above have. It may decrease the power density of the converter, but has higher expendability to connect more than three ports. By using a 3-kW prototype Dual-transformer three-port DAB converter, the performance and effectiveness of the converter are verified with the experimental steady-state operational waveforms and the dynamic response waveform. The full ZVS operation using the proposed magnetizing design method is also experimentally demonstrated with the turn-on transition waveforms.

A voltage balancer for bipolar LVDC distribution using Two-inductor three-port DAB converter is proposed to balance the bipolar voltage levels in case of the grid-tied voltage balancer failures. The voltage balancing operations and the current stress reduction are theoretically analyzed. The performance and validity of the proposed balancer is demonstrated with a 3-kW prototype. The experimental results denote that the converter balances each bus voltage under several load conditions, shows it independently regulate each bus without interference and shows it has reduced current stress compared with that of the conventional converter

REFERENCES

1. D. Boroyevich, I. Cvetković, D. Dong, R. Burgos, F. Wang and F. Lee, "Future electronic power distribution systems a contemplative view," 2010 12th International Conference on Optimization of Electrical and Electronic Equipment, Basov, 2010, pp. 1369-1380

2. A. Q. Huang, M. L. Crow, G. T. Heydt, J. P. Zheng and S. J. Dale, "The Future Renewable Electric Energy Delivery and Management (FREEDM) System: The Energy Internet," in Proceedings of the IEEE, vol. 99, no. 1, pp. 133-148.

3. L. E. Zubieta, "Are Microgrids the Future of Energy?: DC Microgrids from Concept to Demonstration to Deployment," in IEEE Electrification Magazine, vol. 4, no. 2, pp. 37-44, June 2016.

4. De Doncker, R., Divan, D., and Kheraluwala, M. "A three-phase soft-switched high power density DC/DC converter for high power applications." In: Conference Record of the IAS Annual Meeting. Oct. 1988, 796–805 vol.1.

5. Hyun-Jun Choi and Jee-Hoon Jung, "Practical Design of Dual Active Bridge Converter as Isolated Bi-directional Power Interface for Solid State Transformer Applications", Journal of Electrical Engineering & Technology (JEET), vol.11, no.5, pp.1266-1273, Sep 2016

6. B. Zhao, Q. Song, W. Liu and Y. Sun, "Overview of Dual-Active-Bridge Isolated Bidirectional DC–DC Converter for High-Frequency-Link Power-Conversion System," in *IEEE Transactions on Power Electronics*, vol. 29, no. 8, pp. 4091-4106, Aug. 2014.

7. A. R. Rodríguez Alonso, J. Sebastian, D. G. Lamar, M. M. Hernando and A. Vazquez, "An overall study of a Dual Active Bridge for bidirectional DC/DC conversion," *2010 IEEE Energy Conversion Congress and Exposition*, Atlanta, GA, 2010, pp. 1129-1135.

8. B. Zhao, Q. Yu and W. Sun, "Extended-Phase-Shift Control of Isolated Bidirectional DC–DC Converter for Power Distribution in Microgrid," in *IEEE Transactions on Power Electronics*, vol. 27, no. 11, pp. 4667-4680, Nov. 2012.

9. H. Bai and C. Mi, "Eliminate Reactive Power and Increase System Efficiency of Isolated Bidirectional Dual-Active-Bridge DC–DC Converters Using Novel Dual-Phase-Shift Control," in IEEE Transactions on Power Electronics, vol. 23, no. 6, pp. 2905-2914, Nov. 2008.

10. K. Wu, C. W. de Silva and W. G. Dunford, "Stability Analysis of Isolated Bidirectional Dual Active Full-Bridge DC–DC Converter With Triple Phase-Shift Control," in *IEEE Transactions on Power Electronics*, vol. 27, no. 4, pp. 2007-2017, April 2012.

11. G. Xu, D. Sha, J. Zhang and X. Liao, "Unified Boundary Trapezoidal Modulation Control Utilizing Fixed Duty Cycle Compensation and Magnetizing Current Design for Dual Active Bridge DC–DC Converter," in *IEEE Transactions on Power Electronics*, vol. 32, no. 3, pp. 2243-2252, March 2017.

12. C. Zhao, S. D. Round and J. W. Kolar, "An Isolated Three-Port Bidirectional DC-DC Converter With Decoupled Power Flow Management," in IEEE Transactions on Power Electronics, vol. 23, no. 5, pp. 2443-2453, Sept. 2008

13. H. Tao, J. L. Duarte and M. A. M. Hendrix, "Three-Port Triple-Half-Bridge Bidirectional Converter With Zero-Voltage Switching," in IEEE Transactions on Power Electronics, vol. 23, no. 2, pp. 782-792, March 2008.

14. H. Tao, A. Kotsopoulos, J. L. Duarte and M. A. M. Hendrix, "Family of multiport bidirectional DC-DC converters," in *IEE Proceedings - Electric Power Applications*, vol. 153, no. 3, pp. 451-458, 1 May 2006.

15. A. Ganz, "A Simple, Exact Equivalent Circuit for the Three-Winding Transformer," in IRE Transactions on Component Parts, vol. 9, no. 4, pp. 212-213, December 1962.

16. Ju-Young Sim, Jun-Young Lee, Hyun-Jun Choi, Hak-Sun Kim, Jee-Hoon Jung. (2018). Decoupled Power Control of Three-port Dual Active Bridge DC-DC Converter for DC Microgrid Systems. THE TRANSACTIONS OF KOREAN INSTITUTE OF POWER ELECTRONICS, 23(5), 366-372.

17. Arkun Y, Manouslouthakis B, Palazoglu ‘A Robustness analysis of process control systems. A case study of decoupling control in distillation,” IEC Process Des Dev 23(1):93−101 1984.

18. H. Choi, J. Lee, Y. Cho and J. Jung, "Design consideration of efficinecy improvement in three phase dual active bridge converter for LVDC application," *2017 IEEE International Telecommunications Energy Conference (INTELEC)*, Broadbeach, QLD, 2017, pp. 549-555.

19. J. Sim, J. Lee, H. Choi and J. Jung, "High Power Density Bidirectional Three-Port DC-DC Converter for Battery Applications in DC Microgrids," *2019 10th International Conference on Power Electronics and ECCE Asia (ICPE 2019 - ECCE Asia)*, Busan, Korea (South), 2019, pp. 843-848.

20. H. Tao, A. Kotsopoulos, J. L. Duarte and M. A. M. Hendrix, "Multi-input bidirectional DC-DC converter combining DC-link and magnetic-coupling for fuel cell systems," *Fourtieth IAS Annual Meeting. Conference Record of the 2005 Industry Applications Conference, 2005.*, Kowloon, Hong Kong, 2005, pp. 2021-2028 Vol. 3.

21. J. Schäfer, D. Bortis and J. W. Kolar, "Multi-port multi-cell DC/DC converter topology for electric vehicle's power distribution networks," *2017 IEEE 18th Workshop on Control and Modeling for Power Electronics (COMPEL)*, Stanford, CA, 2017, pp. 1-9.

22. S. Shao, H. Chen, X. Wu, J. Zhang and K. Sheng, "Circulating Current and ZVS-on of a Dual Active Bridge DC-DC Converter: A Review," in *IEEE Access*, vol. 7, pp. 50561-50572, 2019.

23. M. Yaqoob, K. H. Loo and Y. M. Lai, "Extension of Soft-Switching Region of Dual-Active-Bridge Converter by a Tunable Resonant Tank," in *IEEE Transactions on Power Electronics*, vol. 32, no. 12, pp. 9093-9104, Dec. 2017.

24. Z. Guo, D. Sha and K. Song, "Output-Series Connected Dual Active Bridge Converters for Zero-Voltage Switching Throughout Full Load Range by Employing Auxiliary LC Networks," in *IEEE Transactions on Power Electronics*, vol. 34, no. 6, pp. 5549-5562, June 2019.

25. N. D. Dinh, N. D. Tuyen, G. Fujita and M. N. B. Muhtazaruddin, "Investigation of ZVS condition for dual-active-bridge converter using dual-phase-shift modulation," *2014 IEEE*

PES Asia-Pacific Power and Energy Engineering Conference (APPEEC), Hong Kong, 2014, pp. 1-6.

26. M. Kim, M. Rosekeit, S. Sul and R. W. A. A. De Doncker, "A dual-phase-shift control strategy for dual-active-bridge DC-DC converter in wide voltage range," *8th International Conference on Power Electronics - ECCE Asia*, Jeju, 2011, pp. 364-371.

27. M. N. Kheraluwala, R. W. Gascoigne, D. M. Divan and E. D. Baumann, "Performance characterization of a high-power dual active bridge DC-to-DC converter," in *IEEE Transactions on Industry Applications*, vol. 28, no. 6, pp. 1294-1301, Nov.-Dec. 1992.

28. Mohammed Ajlif A, S. C. Joseph and Dhanesh P R, "LVDC architecture for residential application," 2016 IEEE International Conference on Power Electronics, Drives and Energy Systems (PEDES), Trivandrum, 2016, pp. 1-4.

29. E. Rodriguez-Diaz, F. Chen, J. C. Vasquez, J. M. Guerrero, R. Burgos, and D. Boroyevich, "Voltage-level selection of future two-level lvdc distribution grids: A compromise between grid compatibiliy, safety, and efficiency," IEEE Electrification Magazine, vol. 4, no. 2, pp. 20–28, 2016.

30. D. Kumar, F. Zare, and A. Ghosh, "Dc microgrid technology: System architectures, ac grid interfaces, grounding schemes, power quality, communication networks, applications, and standardizations aspects," IEEE Access, vol. 5, pp. 12 230–12 256, 2017

31. H. Kakigano, Y. Miura and T. Ise, "Low-Voltage Bipolar-Type DC Microgrid for Super High Quality Distribution," in IEEE Transactions on Power Electronics, vol. 25, no. 12, pp. 3066-3075, Dec. 2010.

32. X. Zhang and C. Gong, "Dual-buck half-bridge voltage balancer," IEEE Transactions on Industrial Electronics, vol. 60, no. 8, pp. 3157–3164, 2013.

33. X. Zhang, C. Gong, and Z. Yao, "Three-level dc converter for balancing dc 800-v voltage," IEEE Transactions on Power Electronics, vol. 30, no. 7, pp. 3499–3507, 2015.

34. G. Byeon, S. Kim, J. Kim, J. Jeon and G. Kim, "Cooperative ESS management strategy for stable islanded operations in a bipolar-type LVDC system," 2015 International Symposium on Smart Electric Distribution Systems and Technologies (EDST), Vienna, 2015, pp. 290-295.

35. S. Rivera and B. Wu, "Electric Vehicle Charging Station With an Energy Storage Stage for Split-DC Bus Voltage Balancing," in IEEE Transactions on Power Electronics, vol. 32, no. 3, pp. 2376-2386, March 2017.

36. IEEE Standard Test Procedures for Electric Energy Storage Equipment and Systems for Electric Power Systems Applications," in IEEE Std 2030.3-2016, vol., no., pp.1-72, 30 Sept. 2016

37. IEEE Recommended Practice for Emergency and Standby Power Systems for Industrial and Commercial Applications," in IEEE Std 446-1995 [The Orange Book], vol., no., pp.1-320, 3 July 1996

38. M. Bartoli, N. Noferi, A. Reatti and M. K. Kazimierczuk, "Modeling Litz-wire winding losses in high-frequency power inductors," PESC Record. 27th Annual IEEE Power Electronics Specialists Conference, Baveno, Italy, 1996, pp. 1690-1696 vol.2.

39. C. P. Steinmetz, "On the Law of Hysteresis," in Transactions of the American Institute of Electrical Engineers, vol. IX, no. 1, pp. 1-64, Jan. 1892.

APPENDIX

A. Derivation of the neutral voltage v_n of the conventional three-port converter

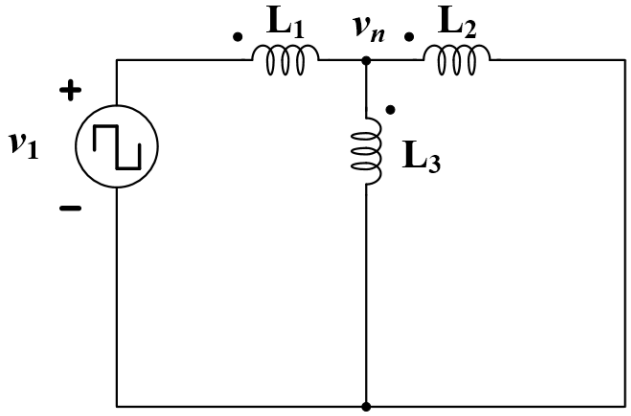

Fig. A1. Equivalent circuit with the two sources v_2 and v_3 short

Fig. 2.3 illustrates the wye-connected equivalent circuit for conventional three-port DAB converter. the neutral voltage v_n can be derived by applying the principle of superposition. Fig. A1 shows the equivalent circuit with one voltage source v_1 and the other two voltage sources v_2 and v_3 short. The neutral voltage v_n seen from the voltage source v_1 side is derived as below:

$$v_n(\omega t) = \frac{L_2 L_3 v_1(\omega t)}{L_1 L_2 + L_1 L_3 + L_2 L_3} \tag{A1}$$

In the same manner, it can be applied to the other two ports. The neutral voltage v_n seen from the other two ports are derived as follows:

$$v_n(\omega t) = \frac{L_1 L_3 v_2(\omega t)}{L_1 L_2 + L_1 L_3 + L_2 L_3} \tag{A2}$$

$$v_n(\omega t) = \frac{L_1 L_2 v_3(\omega t)}{L_1 L_2 + L_1 L_3 + L_2 L_3} \tag{A3}$$

The neutral voltage v_n can be derived by summing the equations (A1), (A2) and (A3)

$$v_n(\omega t) = \frac{L_1 L_2 v_3(\omega t) + L_1 L_3 v_2(\omega t) + L_2 L_3 v_1(\omega t)}{L_1 L_2 + L_1 L_3 + L_2 L_3} \tag{A4}$$

B. Current margin consideration for ZVS operation

Current margin for the ZVS operation is practically required considering the output capacitance (C_{oss}) of MOSFETs and the dead time. To charge the two output capacitance and discharge the rest of the two output capacitance, the magnitude of the charge Q is defined as below:

$$Q = 4C_{oss}V \tag{B1}$$

Where V is the magnitude of the voltage applied across the output capacitance. The charge Q has to be provided by the inductor current. The charge Q can be derived in terms of the current and the time as follows:

$$Q = \int_{\theta_1}^{\theta_1'} i_L \omega t \tag{B2}$$

Since the dead time ωt_d set depending on the designer, that is between θ_1 and θ'_1 is relatively very short time. the inductor current i_L can be considered as constant during the dead time. The equation (B2) can be re-expressed as below:

$$Q = i_L \cdot \omega t_d \tag{B3}$$

Substituting (B1) into (B3), the practical current margin can be calculated as follows:

$$i_L = \frac{4C_{oss}V}{\omega t_d} \tag{B3}$$

C. Estimated loss calculation

Losses in the proposed converter and the conventional converter are mainly categorized into two parts: power switch (MOSFET) losses and magnetic component losses. Parasitic losses are negligible (e.g. PCB conductive loss, capacitor ESR loss, and etc.).

1) MOSFET conduction loss: The conduction loss in the MOSFETs can be straightly calculated by the current flowing through the MOSFET with its on-resistance. The conduction loss in a full-bridge having four MOSFETs is calculated as in the equation (C1), and for a half-bridge organized by two MOSFETs, the conduction loss can be calculated as in the equation (C2).

$$P_{sw\_con(full)} = 4I_{ds,RMS}^2 \cdot R_{ds(on)} \tag{C1}$$

$$P_{sw\_con(half)} = 2I_{ds,RMS}^2 \cdot R_{ds(on)} \tag{C2}$$

Where, $I_{ds,RMS}$ is the RMS value of current conducting through the MOSFET. The RMS value of the MOSFET current and $R_{ds(on)}$ is the on-resistance of the MOSFET presented in the data sheet.

2) MOSFET switching loss: MOSFET switching loss consists of turn-on loss and turn-off loss. If zero voltage switching (ZVS) is achieved, turn-on loss can be significantly reduced. In the design parameters listed in the manuscript, the prototype is designed with nearly unity voltage gains, which ensure the ZVS operation in the DAB converter [25]. Therefore, turn-on loss can be neglectable. Turn-off loss is only considered and can be calculated as follows:

$$P_{sw\_off} = f_{sw} \sum_{j=1}^{N} E_{off,j} \cong N \frac{1}{2} V_{ds} I_{ds} t_{fall} \cdot f_{sw} \tag{C3}$$

Where f_{sw} is the switching frequency, $E_{off,j}$ (j is a MOSFET number in a bridge) is turn-off energy dissipation in a MOSFET during the MOSFET turn-off transient time, N is the number of MOSFETs in a port (e.g. N=4 for a full-bridge and N=2 for a half-bridge), V_{ds} is the voltage before the MOSFET turns off, Ids is the current before the MOSFET turns off, and t_{fall} is the MOSFET falling time.

3) Inductor and transformer winding loss: Winding losses can be calculated as below:

$$P_{wind} \cong 2I_{ds,RMS}^2 \cdot R_{AC} \tag{C4}$$

Where $I_{ds,RMS}$ is the RMS value of current conducting through the MOSFET, which is $1/\sqrt{2}$ of the transformer winding current. Current through the power transfer inductor is the same as the transformer winding current. R_{AC} is the AC resistance of the magnetic component winding. It has strong non-linear characteristics, which is a function of switching frequency, wire length, wire diameter, number of litz wire strands, single litz wire strand diameter and the geometric distance among litz wire strands [38]. Due to the difficulty of the calculation of R_{AC}, R_{AC} values of the inductors and the transformer used for the prototype converter are measured with IM3523 LCR meter manufactured by HIOKI.

4) Inductor and transformer core loss: In the DAB converter, current passing through the inductor and the transformer windings can be assumed to be sinusoidal. If the current sinusoidally excites the core and its magnetic flux is uniformly distributed, the core loss can be calculated using the empirical Steinmetz-formula as follows [39]:

$$P_{core} \cong V_{core} k f_{sw}{}^{\alpha} B_{\max}{}^{\beta} \tag{C5}$$

Where V_{core} is the volume of a core, B_{max} is the peak magnetic flux density, and k, α and β are the core parameters given in a core data sheet.